Title

Automating the Culture of Stress-Reduced Cerebral Organoids with Microfluidics for Long-Term, Feedback-Driven Experiments

Author

Seiler, Spencer Todd

Publication Date

2024

UNIVERSITY OF CALIFORNIA
SANTA CRUZ

AUTOMATING THE CULTURE OF STRESS-REDUCED CEREBRAL ORGANOIDS WITH MICROFLUIDICS FOR LONG-TERM, FEEDBACK-DRIVEN EXPERIMENTS

A dissertation submitted in partial satisfaction of the
requirements for the degree of

DOCTOR OF PHILOSOPHY

in

BIOMOLECULAR ENGINEERING & BIOINFORMATICS

by

Spencer T. Seiler

September 2024

The Dissertation of Spencer T. Seiler
is approved:

Professor David Haussler, Co-chair

Professor Mircea Teodorescu, Co-chair

Professor Sofie Salama

Professor Joshua Stuart

Peter Biehl
Vice Provost and Dean of Graduate Studies

Contents

List of Figures

List of Tables

Abstract

Automating the culture of stress-reduced cerebral organoids with microfluidics for long-term, feedback-driven experiments

by

Spencer T. Seiler

Stem cell biology has enabled the development of 3D organ-specific *in vitro* models that mimic aspects of *in vivo* tissue. The analysis of tissue cultures, particularly brain organoids, takes a high degree of coordination, measurement, and monitoring. Here, I have developed a novel microfluidic platform that automates the culture of individual organoids in isolated microenvironments at user-defined flow rates. This technology has enabled greater homeostatic regulation of culture's media through frequent, low-volume replenishment cycles. RNA sequencing (RNA-seq) analysis of automated cerebral cortex organoid cultures showed benefits in reducing glycolytic and endoplasmic reticulum stress compared to conventional *in vitro* cell cultures. For the first time, longitudinal metabolic profiles tracing glucose and lactate over 105 days of culture were achieved for six cerebral cortex organoid protocols.

The microfluidic technology was advanced to integrate electrophysiology and imaging into a unified system for feedback-driven studies. An Internet of Things (IoT) architecture was developed to enable continuous, communicative interactions among sensing and actuation devices, achieving precisely timed control of biological experiments. Computer vision for fluid volume estimations of aspirated media was used as feedback to rectify deviations in microfluidic perfusion during media feeding/aspiration cycles. The system performed 7-day studies of mouse cerebral cortex organoids, comparing manual and automated protocols. The automated experimental samples maintained robust neural activity throughout the experiments; however, the system enabled hourly electrophysiology recordings that revealed dramatic temporal changes in neuron firing rates not observed in once-a-day recordings.

This work is dedicated to my parents, Todd and Laurie,
whom cheered me on at each success and picked up every phone call at
each low. I have the greatest love and gratitude for the continual blessings
that my family has brought to my life, enabling my persistence through
the marathon that is scientific research.

Acknowledgments

The Braingeneer's lab and UCSC has been a haven for scientific investigation. I want to chiefly thank professors Mircea Teodorescu, Sofie Salama, and David Haussler for advising, funding, critiquing, and promoting my work here. I have also been greatly influenced by the guidance of Mohammed Mostajo Radji, Rob Currie, Tal Sharf in the Braingeneers. I want to thank the UCSC Genomics Institute and Baskin School of Engineering for their resources and the research environment.

My work here has been possible through the gracious collaboration of colleague researchers. The major contributions and gratitudes I would like to call out are:

- **Kateryna Voitiuk** for generating the microfluidic culture chamber, 3D printing, designing the IoT messenging software, running experiments, analyzing data, and co-writing the "Integrated System" manuscript.

- **Mirella Pessoa de Melo (Ella)** for the generating computer vision technology and co-developing the Integrated System.

- **Ryan Hoffman** for the meticulous and extensive organoid cell culture, single cell sequencing, and experimental design regarding our "Adaptive Glucose" study.

- **Sebastian Hernandez** and **Hunter Schweiger** for producing the magically sparky mouse organoid cultures.

- **Jess Sevetson** and **Tjitse van der Molen** for experimental design, guidance in electrophysiology, and data analysis.

- **Pierre Baudin** and Victoria Ly for the *Picroscope* imaging platform and experiment collaborations.
- **Mojtaba Zeraatkar** for design and development of the servo-motor manifold.
- **Gary Mantalas** for assistance in experimental design, organoid culture, and RNA-seq library construction.
- **Jack Selberg** and **Sergio Cordero** whom designed and fabricated the microfluidic chips.
- **David F. Parks** for generating and maintaining the *braingeneerspy* software infrascrutcture making our automated experiments possible.
- **Sebastian Torres** who completed the COMSOL finite element analysis simulating the microfluidic chip's fluid dynamics.
- **Viktor Yurevych**, **Ravipa Losakul**, **Ruiting Xu**, and **Julker Neyen Sampad** as collaborators whom generated the devices and protocols for extracellular vesicle sensing and analysis.

I want to extend a further thanks to Anna Toledo, Demir Ozcakir, Quinton Brail, Kristof Tigyi, Samira Vera-Choqqueccota, Yohei Rosen, Jinghui Geng (Sury), Valeska Victoria, Pierre Baudin, Lon Blauvelt, Catharina Lindley, the IBSC Cell Culture Facility (RRID:SCR 021353), Pacific Research Platform (PRP), and the UCSC Life Sciences Microscopy Center (RRID:SCR 021135) for valuable resources and assistance.

This work was supported by the Schmidt Futures Foundation SF 857 and the National Human Genome Research Institute under Award number 1RM1HG011543, the National Institute of Mental Health of the National Institutes of Health under Award Number R01MH120295, the National Institute of Mental Health grant 1U24MH132628, the National Institutes of Health (NIH) under award number K12GM139185 and the Institute for the Biology of Stem Cells (IBSC) at UC Santa Cruz, the National Science Foundation under award number NSF 2034037, and NSF 2134955. This work was supported in part by National Science Foundation (NSF) awards CNS-1730158, ACI-1540112, ACI-1541349, OAC-1826967, OAC-2112167, CNS-2100237, CNS-2120019, the University of California Office of the President, and the University of California San Diego's California Institute for Telecommunications and Information Technology/Qualcomm Institute.

Chapter 1

Introduction

1.1 Motivation

Automated technologies are transforming our ability to control, and I receive great satisfaction in engineering tools to magnify the quality and scale of research. Electronic and mechanical devices have a better orientation to accomplish tasks of precision, consistency, and throughput compared to human researchers. I believe furthering the use of automated technologies is an incredible, yet untapped advantage for the field of biological research. By designing and presenting tools for automation-assisted research, we can lower the barrier of entry so that novices or experts in other disciplines may complete complex, large-scale experiments that would otherwise be prohibitive. This is the heart of democratizing scientific research so that many diverse participants may contribute and interact with our growing body of science. In addition to generating automated technologies for a broader audience, doing so by means of open-source designs, maker-space printed components, and wide-ranging application changes the paradigm regarding robotic solutions. Currently, it takes immense industrial scale and massive repetition to merit robotic automation. Instead, I am motivated by generating versatile, reprogrammable technologies that drive greater fundamental discovery while reducing manual labor. To me, these advances usher in a future where researchers from many walks of life spend more time in creative and analytical spaces while our automated tools care for our experiments with great precision at all hours of the day.

1.2 Contribution of Work

This thesis presents a technological advance and new protocols in tissue culture research. I co-led the research leading to publication, "Modular automated microfluidic cell culture platform reduces glycolytic stress in cerebral cortex organoids" [84] and preprint, "A feedback-driven IoT microfluidic, electrophysiology, and imaging platform for brain organoid studies" [105].

- Developed the *Autoculture* platform, an automated microfluidic system for long-term cerebral organoid culture, integrating precision fluid handling, environmental control, and real-time monitoring [84, 48, 59].
- Designed and validated novel microfluidic chips for individual organoid culture, enabling high-throughput and reduced variability [84].
- Demonstrated reduced glycolytic and endoplasmic reticulum cellular stress in automated organoid cultures [84].
- Produced longitudinal metabolic profiles tracing glucose and lactate over 105 days of culture were achieved for six cerebral cortex organoid protocols [publication in development].
- Engineered a feedback control system for media exchange in long-term organoid cultures, ensuring stable environmental conditions [105].
- Integrated high-density microelectrode arrays with automated microfluidics and

in-incubator imaging, creating a comprehensive platform for multi-modal organoid analysis [105, 59].

- Established protocols for maintaining stable, long-term (7+ days) automated organoid cultures with minimal human intervention, paving the way for extended developmental studies [84, 48, 105].
- Revealed dynamic neural activity patterns in cerebral organoids through high-frequency, long-term electrophysiological recordings, uncovering temporal dynamics [105].

1.3 List of Terms

***Autoculture*:** Name of the automated, microfluidic cell culture platform that includes hardware, electronics, microfluidic tubing, consumables, and software.

Cerebral cortex organoid: 3D cell cultures derived from stem cells that model aspects of human brain development and function, including many cortex-specific cell types and sub-regions.

Connector plate: The custom-manufactured platform-to-chip interface plate that mates microfluidic tubes (from the *Autoculture* platform) to inlets and outlets of the microfluidic chip.

Manifold: An extension to the connector plate that performs fluid channel switch operations, enabling multiplexed microfluidics.

Microfluidic chip: The custom well plate designed to interface with the *Autoculture* platform and service cultures in parallel.

Organoid Nursery: A variation of the microfluidic chip that is aimed expanding organoid cultures in high-throughput and consistency.

Stress: A cellular condition of disregulated health leading towards cell death. This is sub-categorized here as glycolytic and endoplasmic reticulum (ER) stress.

1.4 List of Abbreviations

AF: Automatic feeding, an experimental condition where organoids are fed automatically but recorded manually.

AFAR: Automatic feeding and automatic recording, an experimental condition combining automated feeding and electrophysiological recording.

API: Application programming interface, a set of protocols, routines, and tools for building software applications.

AR: Automatic recording, an experimental condition where organoids are automatically recorded but fed manually.

CFD: Computational fluid dynamics, a branch of fluid mechanics that uses numerical analysis and data structures to analyze and solve problems involving fluid flows.

CMOS: Complementary Metal-Oxide-Semiconductor, a technology used in manufacturing microelectronics, including microelectrode arrays.

DGE: Differential gene expression, relating to RNA sequencing analysis.

FEP: Fluorinated ethylene propylene, a type of fluoropolymer used for tubing in the microfluidic system.

GUI: Graphical user interface, a form of user interface that allows users to interact with electronic devices through graphical icons and visual indicators.

HD-MEA: High-density microelectrode array, a device used in electrophysiology to measure the electric field potential of cells, particularly neurons. It consists of an electrode grid used to detect the electrical signals of cells cultured on the array.

HSV: Hue, saturation, value, a color model used in computers for image processing.

IoT: Internet of Things. A network of interconnected devices that can communicate and exchange data.

PSCs: Pluripotent stem cells, cells that can give rise to all cell types found in an organism, including both embryonic stem cells (ESCs) and induced pluripotent stem cells (iPSCs).

LED: Light-emitting diode, a semiconductor device that emits light when an electric current passes through it.

MAE: Mean absolute error, a measure of the average magnitude of errors in a set of predictions.

MQTT: Message queuing telemetry transport, a messaging protocol used for IoT communication.

Oxphos: Oxidative phosphorylation, the metabolic pathway in which cells use enzymes to oxidize nutrients, thereby releasing energy which is used to produce ATP.

LDH: Lactate dehydrogenase, an enzyme that catalyzes the interconversion of pyruvate and lactate.

LOO: Leave-one-out cross-validation, a method for assessing how well a model generalizes to unseen data.

PDMS: Polydimethylsiloxane, a silicone-based polymer often used in microfluidic devices.

RMSE: Root mean square error, a measure of the standard deviation of residuals in a predictive model.

RNA-seq: RNA sequencing, a technique used to analyze gene expression by sequencing RNA molecules in a biological sample.

ROS: Reactive oxidative species.

S3: Simple Storage Service, a cloud storage service provided by Amazon Web Services.

SOP: Standard operating procedure. This is a verified protocol that is taken to ensure proper use of instruments, quality of data, and consistency between operators.

TCA: Tricarboxylic acid cycle, also known as the Krebs cycle, a series of chemical reactions used by aerobic organisms to release energy through the oxidation of acetyl-CoA.

UUID: Universally unique identifier, a letter/number identifier for cloud infrastructure organization and data retrieval.

Chapter 2

Background

2.1 *In Vitro* Models of the Brain

2.1.1 Stem cell-based models

Cell culture has been a fundamental model for studying human disease and development for over 70 years, dating back to the isolation of HeLa cells from a human cervical cancer biopsy [87, 81]. These cultures were optimized for rapid growth and high yields, particularly for virus research, and many aspects of these early protocols persist in modern cell culture practices. However, there is increasing recognition that traditional culture methods often fail to accurately mimic physiological conditions, particularly in terms of nutrient concentrations and metabolic dynamics [15].

The advent of human pluripotent stem cell (hPSC) technology has revolutionized *in vitro* modeling of human tissues [74, 62]. This field encompasses two main types of pluripotent stem cells: embryonic stem cells (ESCs) and induced pluripotent stem cells (iPSCs). ESCs, first isolated from human blastocysts in 1998 by Thomson et al. [98], possess the ability to differentiate into all three germ layers. The development of iPSCs by Takahashi and Yamanaka in 2006 [95] further expanded the potential of stem cell research by allowing the reprogramming of adult somatic cells into a pluripotent state, overcoming ethical concerns associated with ESCs, and opening up possibilities for patient-specific disease modeling.

Pluripotent stem cells offer opportunities to study human development, disease processes, and potential therapeutic interventions. Key applications include:

- **Developmental biology:** hPSCs allow researchers to study early human development in vitro, providing insights into processes that were previously inaccessible [108].
- **Disease modeling:** Patient-derived iPSCs enable the creation of disease-specific cell lines, facilitating the study of genetic disorders and complex diseases [45].
- **Drug discovery and toxicology:** Stem cell-derived tissues provide more physiologically relevant models for drug screening and toxicity testing compared to traditional 2D cell cultures [16].
- **Regenerative medicine:** The ability to generate specific cell types from hPSCs holds promise for cell replacement therapies and tissue engineering [97].

The integration of stem cell technology with advanced culturing methods, such as microfluidics and organ-on-chip systems, promises to further bridge the gap between *in vitro* models and *in vivo* physiology [30]. These approaches aim to provide more accurate and physiologically relevant models for studying human biology and disease, ultimately accelerating the translation of basic research into clinical applications.

2.1.2 Cerebral organoids: development and applications

Building upon advances in stem cell biology, three-dimensional (3D) organoid cultures have emerged as powerful tools for modeling complex tissues and organ systems. Cerebral organoids, in particular, have gained significant attention for their ability to recapitulate key aspects of human brain development and function [40, 17]. These 3D cultures are generated by aggregating hPSCs and subjecting them to specific differentiation protocols that promote the formation of neural tissues [41].

Cerebral organoids contain multiple cell types found in the developing brain, including neural progenitors, neurons, and glial cells, organized into structures reminiscent of the cerebral cortex [72]. They have been successfully used to study various aspects of neurodevelopment [33, 53], model neurological disorders [23], and even investigate human-specific features of brain evolution [68].

The process of generating cerebral organoids typically involves several key steps (see Fig. 2.1): expansion of hPSCs in 2D culture, aggregation of cells into embryoid bodies, neural induction through the inhibition of specific signaling pathways (e.g., WNT and Nodal/Activin), and maturation and differentiation in 3D culture conditions.

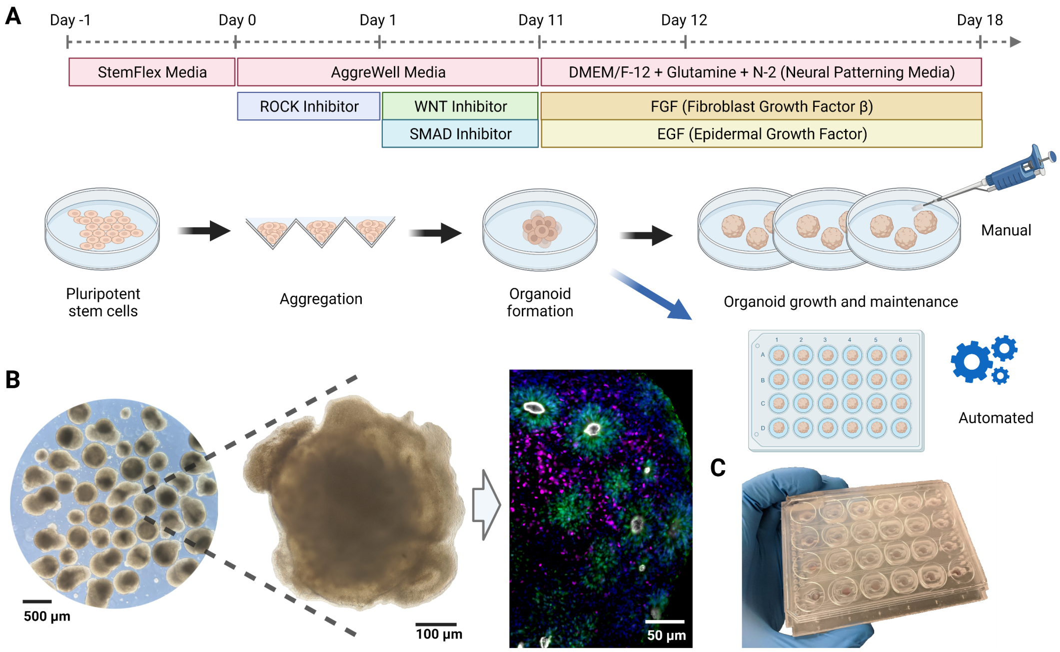

Figure 2.1: Overview of the human cerebral organoid generation protocol. **(A)** Human pluripotent stem cells are expanded in traditional 2D culture, dissociated, aggregated into microwells, and matured into 3D organoid cultures using defined media conditions to promote cerebral cortex tissue differentiation. In this study, on day 12 post-aggregation, organoids were either kept in suspension and maintained manually (black arrow) or transferred to individual wells of a microfluidic chip and maintained in automation (blue arrow). **(B)** Images of cerebral organoid cultures. Bright-field images at low (left) and high (center) magnification under standard culture conditions show organoid morphology and heterogeneity. Immunofluorescence stains on week 5 for PAX6 (green, radial glia progenitor cells), CTIP2 (BCL11B) (magenta, excitatory projection neurons), ZO-1 (TJP1) (white, tight junction proteins on radial glia end-feet, apical surface of the neural tube), show characteristic ventricular zone-like rosette structures with radial glia surrounded by neurons. Nuclei stained with DAPI (blue). **(C)** Image of the PDMS microfluidic chip. The custom cell culture chip, modeled after a standard 24-well plate, houses organoids for automated experiments.

As organoid development progresses, various cell types and structures emerge, including radial glial cells organized into ventricular zone-like rosettes, intermediate progenitors, and neurons of different cortical layers [21].

Despite their utility, currently cerebral organoid models face several limitations:

- Variability between batches and protocols
- Lack of vascularization, leading to potential nutrient and oxygen gradients
- Presence of cellular stress that may not accurately reflect *in vivo* conditions
- Absence of certain cell types/subtypes and structures found in the developing brain

These challenges highlight the need for improved culture systems that can better maintain physiological conditions, reduce artifactual stress responses, and promote more complete and accurate brain-like development [6, 103].

2.2 Cellular Metabolism in the Brain

2.2.1 Glucose and glycolysis

The brain is an exceptionally energy-demanding organ, consuming approximately 20% of the body's resting energy despite comprising only 2% of body mass [27]. Glucose serves as the primary energy source for the brain, with its metabolism occurring through a series of interconnected pathways: glycolysis, the tricarboxylic acid (TCA) cycle, and oxidative phosphorylation [111].

Glycolysis, the initial step in glucose metabolism, occurs in the cytosol and involves the breakdown of glucose into pyruvate through a series of enzymatic reactions. This is a ten-reaction, two-stage process that yields a net gain of 2 ATP molecules per glucose molecule, as well as reducing equivalents in the form of NADH [20]. Although glycolysis doesn't require oxygen, it occurs in both aerobic and anaerobic variations. In aerobic conditions, pyruvate enters the citric acid cycle and undergoes oxidative phosphorylation leading to the net production of 30-32 ATP molecules.

The overall reaction of aerobic glycolysis can be summarized as:

$$Glucose + 2\ NAD^+ + 2\ ADP + 2\ P_i$$

$$\rightarrow 2\ Pyruvate + 2\ NADH + 2\ H^+ + 2\ ATP + 2\ H_2O$$

Key regulatory enzymes in glycolysis include:

- **Hexokinase (HK):** Catalyzes the first step of glucose phosphorylation
- **Phosphofructokinase (PFKM):** The primary rate-limiting enzyme of glycolysis [1]
- **Glyceraldehyde-3-phosphate Dehydrogenase (GAPDH):** The enzyme to convert NAD+ to NADH in glycolysis
- **Pyruvate kinase (PK):** Catalyzes the final step, generating ATP and pyruvate

2.2.2 Lactate and anaerobic glycolysis

Under conditions of limited oxygen availability or high energy demand, cells can engage in anaerobic glycolysis, also known as the lactic acid cycle. This process involves the conversion of pyruvate into lactate, catalyzed by lactate dehydrogenase (LDH) [25]. Anaerobic glycolysis is an energetic compromise in that it sacrifices 95% of the potential energy in glucose (36 out of 38 ATP) however, it receives the 5% of energy (2 ATP) 100 times faster than through oxidative phosphorylation [112]. Anaerobic glycolysis transforms glucose into lactate and is generally reserved for short bursts of high metabolic requirements.

Under high energy demand when oxygen is limited, lactate is produced from pyruvate faster than the system can process it, causing lactate concentrations to rise. The lactate production is beneficial for NAD+ regeneration (pyruvate is reduced to lactate while NADH is oxidized to NAD+), which is subsequently used in the oxidation of glyceraldehyde 3-phosphate (G3P) during the production of pyruvate from glucose in aerobic glycolysis. In this way, the byproducts of short-term lactate production are useful when aerobic metabolism resumes, however, pathology arises when anaerobic metabolism is relied upon. The excess lactate produced from anaerobic glycolysis can be used in two ways: (1.) oxidation back to pyruvate via lactate dehydrogenase, or (2.) conversion back to glucose (gluconeogenesis) in the liver via the Cori cycle

Only the first of these (lactate dehydrogenase) is available in the brain (and cerebral organoids). The build-up of lactate can result in lactic acidosis, a lowering of pH to pathological levels. The ”A chain” isoform of the enzyme lactate dehydrogenase (LDHA, or LDH-M) has a higher affinity for converting pyruvate into lactate to produce energy. This is primarily found in neurons, muscle tissue, and the liver. The ”B chain” isoform of the enzyme lactate dehydrogenase (LDHB, LDH-H), has a higher affinity for converting lactate back into pyruvate. In hypoxic conditions, the expression of LDHA represents a shift in the metabolic pathway of ATP synthesis away from oxidative phosphorylation and back to glycolysis [32]. This phenomenon is called the Warburg effect, reported in the 1920's [11, 69, 107]. LDH is the most important factor in this effect, playing a pivotal role in this metabolic shift.

There are reports that indicate lactate, not glucose, is preferentially metabolized by neurons in the brain [110, 114]. According to the lactate-shuttle hypothesis, glial cells are responsible for transforming glucose into lactate and for providing lactate to the neurons [22, 64]. It was hypothesized that lactate might exert a strong action over GABAergic networks in the developing brain, making them more inhibitory than it was previously assumed [28], acting either through better support of metabolites [114], or alterations in base intracellular pH levels [101, 76], or both [35]. Studies of brain slices of mice show that β-hydroxybutyrate, lactate, and pyruvate act as oxidative energy substrates, causing an increase in the NAD(P)H oxidation phase, that glucose was insufficient as an energy carrier during intense synaptic activity and, finally, that lactate can be an efficient energy substrate capable of sustaining and enhancing brain aerobic energy metabolism *in vitro* [31].

The induction of 3-phosphoinositide-dependent protein kinase-1 (PDK1) and

LDHA expression shunts pyruvate away from the mitochondria, thereby reducing the flux of acetyl-CoA through the TCA cycle and reducing the production of NADH and the subsequent consumption of O2 as the final electron acceptor in the electron transport chain. The efficiency of electron transport under hypoxic conditions is reduced, leading to increased mitochondrial ROS production [26].

The overall reaction of anaerobic glycolysis:

$$Glucose + 2\ NAD^{+} + 2\ ADP + 2\ P_i \rightarrow 2\ Lactate + 2\ NADH + 2\ H^{+} + 2\ ATP$$

The conversion of pyruvate to lactate:

$$Pyruvate + NADH + H^{+} \leftrightarrow Lactate + NAD^{+}$$

Key regulatory enzymes in lactate and anaerobic glycolysis include:

- **Lactate Dehydrogenase (LHD):** The enzyme that converts pyruvate to lactate.
- **3-Phosphoinositide-dependent Protein Kinase-1 (PDK1):** The kinase enzyme which acts to inactivate pyruvate dehydrogenase by phosphorylating it using ATP. This shunts pyruvate away from the mitochondria to inhibit TCA and Oxphos.

2.2.3 Tricarboxylic acid cycle and oxidative phosphorylation

The tricarboxylic acid (TCA) cycle, also known as the citric acid cycle (CAC) or Krebs cycle, is a series of chemical reactions to release stored energy through the oxidation of acetyl-CoA derived from carbohydrates, fats, and proteins. The TCA cycle does not produce ATP directly, however, it produces energy-containing compounds NADH, FADH2, and GTP that are consumed in oxidative phosphorylation for high ATP generation [2]. The TCA cycle consumes acetyl-CoA and water, reduces NAD+ to NADH, and releases carbon dioxide. In all eukaryotic cells, the TCA cycle occurs in mitochondria. It is pyruvate dehydrogenase (PDH) that links glycolysis to the TCA cycle. Pyruvate production through pyruvate dehydrogenase is the principal source of acetyl-CoA, which is a direct energy substrate in all brain cells. Several neurodegenerative conditions result in the inhibition of pyruvate dehydrogenase and a decrease of acetyl-CoA synthesis in mitochondria. This attenuates metabolic flux through TCA in the mitochondria, yielding energy deficits and inhibition of diverse synthetic acetylation reactions in all neuronal sub-compartments [75]. Alterations in acetyl-CoA levels alone may significantly change the rates of metabolic fluxes through multiple acetylation reactions in brain cells in different physiologic and pathologic conditions.

Oxidative phosphorylation (Oxphos), or electron transport-linked phosphorylation, is the final metabolic pathway in which cells use enzymes to oxidize nutrients to release energy for ATP generation. Oxphos is the most efficient means of ATP production from glucose, occurring in the inner mitochondrial membrane for eukaryotes. This process involves the transfer of electrons through a series of protein complexes (the electron transport chain), coupled with the pumping of protons across the membrane to generate an electrochemical gradient. This gradient drives the synthesis of ATP through ATP synthase [73].

The overall reaction of tricarboxylic Acid (TCA) Cycle:

$$\textit{Acetyl-CoA} + 3\ NAD^+ + FAD + GDP + P_i + 2\ H_2O$$

$$\rightarrow \textit{CoA-SH} + 3\ NADH + FADH_2 + 3\ H^+ + GTP + 2\ CO_2$$

The overall reaction of oxidative phosphorylation:

$$ADP + P_i + NADH + H^+ + O_2 \rightarrow ATP + H_2O + NAD^+$$

Key enzymes and regulators in the TCA cycle include:

- **Pyruvate dehydrogenase (PDH):** The enzyme linking glycolysis to the TCA cycle by converting pyruvate to acetyl-CoA

- **ATP Citrate Lyase (ACLY):** The primary enzyme responsible for the synthesis of cytosolic acetyl-CoA from citrate. This enzyme links upstream metabolism (glycolysis) which yields citrate as an intermediate to TCA and Oxphos that both oxidize acetyl-CoA.

- **Isocitrate dehydrogenase (IDH):** Catalyzes a rate-limiting step in the TCA cycle

- **AMP-Activated Protein Kinase (AMPK):** is a cellular energy sensor that is activated under conditions of low energy availability. It regulates energy metabolism by inhibiting anabolic processes and activating catabolic processes, such as mitochondrial biogenesis and oxidative phosphorylation.

- **Mitochondrial Transcription Factor A (TFAM):** is a nuclear-encoded protein that is essential for the transcription and replication of mitochondrial DNA (mtDNA). It plays a critical role in the regulation of mitochondrial biogenesis and oxidative phosphorylation.

2.2.4 Hypoxia and metabolic stress in cerebral organoids

In the brain, acute changes in metabolism occur in response to neuronal stimulation, and the increased energy demand causes a Warburg-like transient dissociation between glycolysis and Oxphos [111]. While Oxphos generates the majority of ATP derived from glucose (26-30 molecules), it is reliant on oxygen availability. Limited oxygen inititates the hypoxic stress response to adjust cellular activity to be more oxygen-sparing. The highly-conserved hypoxia-inducted factor 1 (HIF-1) is a transcription factor that initiates the signal of over 60 genes in the hypoxic stress response [90]. One global strategy to divert energy production away from oxidative metabolism is to reduce mitochondrial mass through selective autophagy. HIF-1 activates transcription of the BNIP3 and BNIP3L genes, which encode mitochondrial proteins that trigger mitochondria-selective autophagy in hypoxic cells [5, 39]. Failure to induce BNIP3 expression results in increased reactive oxygen species (ROS) production under conditions of chronic hypoxia and ROS-induced cell death [39].

A significant challenge in cerebral organoid culture is the development of hypoxic and metabolically stress regions [6]. This is in part due to limitations in oxygen diffusion as the organoids grow larger [51] however it remains a sparsely understood issue. Metabolic stress and the activation of hypoxia-inducible factors (HIFs) alter gene expression to adapt to low-oxygen conditions [85] and non-ideal energetic environments. This stress can lead to alterations in cell fate decisions, increased cell death, and changes in gene expression profiles that may not accurately reflect *in vivo* development [6, 63, 68].

Current strategies to address metabolic stress in organoid cultures include:

- Optimization of media composition and feeding schedules
- Development of perfusion-based culture systems
- Integration of vascular-like structures or co-culture with endothelial cells
- Use of oxygen-carrying perfluorocarbons to enhance oxygen delivery

Understanding and mitigating these stress responses is crucial for developing more physiologically relevant organoid models.

2.3 Microfluidics and Automation in Cell Culture

2.3.1 Laboratory robotics and liquid handling systems

In cell culture, dispensing, moving, and removing liquid are the necessary actions required for all protocols. Advancements in laboratory automation, particularly in liquid handling technologies, have opened new possibilities for precise and high-throughput experimentation in cell culture [37]. These systems can be broadly categorized into continuous-flow and digital microfluidic platforms, each with unique advantages for different applications [54]. Continuous-flow systems rely on steady-state liquid flow generated by pressure, mechanical, or electrokinetic pumps. With constant flow, these systems deliver control of velocity and homogeneity; however, they are less flexible for complex fluidic manipulations and challenging to scale. Closed-channel systems derived from continuous flow are inherently difficult to access, require managing trapped gasses, and do not scale well because the parameters that govern flow at any single location depend on the entire system's properties.

Continuous-flow systems rely on steady-state liquid flow generated by pressure, mechanical, or electrokinetic pumps. These systems offer high control over velocity and homogeneity but may be less flexible for complex manipulations. In contrast, droplet-based or segmented-flow microfluidics control discrete volumes, allowing for more complex operations such as mixing, encapsulation, and sorting [96].

Liquid handling technologies (within the digital microfluidics category) have evolved to include both contact and non-contact approaches:

- Contact liquid handlers: Require a tip containing liquid to meet the substrate, similar to manual pipetting but with greater precision and control.
- Non-contact liquid handlers: Manipulate fluid pressures and velocities to control flow without direct contact with the substrate.

Both technologies have advanced to achieve ultra-low volumes (nanoliter scale) and ultra-low flow rates (microliter per hour), enabling precise control over the cellular microenvironment [?]. Contact liquid handlers offer increased precision and throughput but are primarily designed for pharmaceutical screens, limiting their adoption in research labs due to high costs, large footprints, and inflexible workflows [37, 99]. Moreover, many of these systems lack the ability to seamlessly integrate new technologies as they emerge. Conversely, academic research labs are benefiting from advancements in commercial and custom-made technologies, facilitated by in-house fabrication methods like 3D printing [50, 106], which are enhancing their capacity to manipulate and measure biological systems. However, without an easy-to-integrate, device-agnostic robotic platform, researchers are constrained to manual operations, restricting the power and scope of their experiments. By outfitting devices to carry out automated jobs and relay data through communication networks, they acquire around-the-clock functionality and increased fidelity [29]. The flexibility in size (number of devices per integrated system) allows researchers to optimize for the experimental design and budget. Implementing programmable feedback loops derives precision and self-optimization by dynamically adjusting to real-time data [10, 38, 89], offering a practical alternative to complex mathematical modeling for experiment control. This approach would enable more integrated, flexible automation in research settings, broadening the scope and efficiency of experiments.

2.3.2 Microfluidic platforms for organoid culture

Microfluidic technologies offer unprecedented control over the cellular microenvironment, allowing for precise manipulation of media composition, flow rates, and gradients [86]. These systems are particularly promising for organoid culture, as they can provide more physiological conditions and enable long-term maintenance with minimal manual intervention [113]. Key advantages of microfluidic platforms for organoid culture include precise control over nutrient delivery and waste removal, the ability to generate stable concentration gradients, reduced shear stress compared to traditional orbital shaker cultures, potential for real-time monitoring and analysis of cellular responses, and scalability for high-throughput experimentation.

Recent developments in microfluidic organoid culture systems have focused on:

- Integration of multiple organoid types for ”body-on-a-chip” applications
- Development of perfusion-based systems to improve nutrient delivery
- Incorporation of sensing elements for real-time monitoring of cellular metabolism
- Design of modular systems that allow for flexible experimental setups

Organoids are commonly grown in batches with several organoids suspended in single wells of a plate. The shared conditions in a single well support batch consistency; however, increasing the number of variables in an experiment, such as including multiple genotypes, throughput becomes challenging. Furthermore, multi-well plates are not well suited for controlling dynamic conditions nor generating concentration gradients in the media. In contrast, microfluidic chips enable precise control of environmental conditions with high spatiotemporal resolution [86, 113]. Serial dilutions can achieve automated gradients, and robotic volumetric flow can efficiently manage high throughput experiments. The choice of device for laboratory automation should consider the use, flexibility, and cost. Considering the microenvironment of the cell culture, a non-contact system offers key advantages to maintaining homeostasis of nutrient concentrations, reducing the build-up of metabolic byproducts, and generating shear forces more similar to *in vivo* conditions.

2.3.3 Internet of Things (IoT) integration in biological research

Automating multiple devices to report data presents a challenge for device management and communication, necessitating flexible and efficient infrastructure. Addressing this need for an interconnected ecosystem of devices, services, and technologies is possible through designing networks using standards defined by the Internet of Things (IoT). This approach has already impacted wearables [61], agriculture [8], city infrastructure [92], security [78], and healthcare [34]. It was recently proposed to expand this approach to biology research [59]. Previously, each researcher built a custom device and code from scratch with unique assumptions for communication and behavior. Each device operated in solitude, lacking integration and feedback with other devices. Here, we establish a platform that addresses these challenges, combining electrophysiology, microscopy, microfluidics, and feedback control, automated and integrated through IoT technology for touch-free, in-incubator tissue research.

Benefits of IoT integration in organoid research include:

- Increased reproducibility through standardized protocols and automated workflows

- Enhanced data collection and analysis capabilities
- Improved resource utilization through optimized scheduling and remote monitoring
- Facilitation of collaborative research across multiple institutions

2.4 Electrophysiology in Organoid Research

2.4.1 Principles of neural electrophysiology

Electrophysiological recordings provide crucial insights into the functional properties of neurons and neural networks within cerebral organoids [60]. These techniques allow for the measurement of various electrical signals, including:

- Action potentials: Rapid changes in membrane potential that propagate along neuronal axons
- Synaptic currents: Small electrical currents generated by the activation of neurotransmitter receptors
- Local field potentials: Summed electrical activity from populations of neurons

Electrophysiological measurements in organoids can provide information on neuronal maturation and excitability, synaptic connectivity and plasticity, network-level activity patterns and oscillations, and responses to pharmacological interventions or environmental stimulation.

2.4.2 Data acquisition and analysis in organoid models

Recent advances in multi-electrode array (MEA) technologies and high-density CMOS-based systems have dramatically increased the spatial and temporal resolution of electrophysiological recordings in 3D cultures [52]. These technologies allow for simultaneous recording from hundreds or thousands of electrodes, providing a comprehensive view of neural network activity within organoids. Data analysis approaches for organoid electrophysiology include spike detection and sorting algorithms to identify individual neuronal units, network connectivity analysis to map functional connections between neurons, spectral analysis to characterize network oscillations and rhythms, and machine learning approaches for pattern recognition and classification of activity states.

Key considerations in electrophysiological recordings from organoids include:

- Electrode density and spatial coverage
- Signal-to-noise ratio and artifact removal
- Long-term stability for longitudinal recordings
- Cross-compatibility with other analysis techniques such as imaging

Most considerations on the list above remain areas of development for this field. By combining advanced electrophysiological techniques with microfluidic culture systems and IoT integration, researchers can gain insight into the functional development and maturation of cerebral organoids, paving the way for more accurate modeling of human brain function and disease.

Chapter 3

Generate an Automated Microfluidic Organoid Platform

3.1 Introduction

Cerebral organoids has advanced our ability to study brain development and disease *in vitro*. However, current methods for culturing these complex 3D structures are labor-intensive, prone to variability, and may induce cellular stress that does not reflect *in vivo* conditions. To address these limitations, I have developed the *Autoculture* platform, an automated microfluidic system designed to optimize cerebral organoid culture. In this section, I describe the design, fabrication, and validation of the *Autoculture* platform.

The aim here was to create a system to:

- Provide precise control over media exchange and feeding schedules
- Maintain a stable microenvironment for long-term organoid culture
- Enable high-throughput experimentation with minimal manual intervention
- Integrate with other technologies for comprehensive organoid analysis

I detail the components of the *Autoculture* platform, including its microfluidic chip design, fluid dynamics, and integration with imaging systems. The content here closing follows the publication ”Modular automated microfluidic cell culture platform reduces glycolytic stress in cerebral cortex organoids” (Seiler, *et al.*, 2022) [84].

3.2 The *Autoculture* platform

The *“Autoculture”* platform is an automated, microfluidic cell culture platform to optimize 3D organoid growth. The system consists of six linked modules (Fig. 3.1): (1) Refrigerator with reagent reservoirs (e.g., fresh media), (2) Syringe pump, distribution valves, and control interface, (3) conditioned media collection reservoirs in cold storage, (4) a microfluidic serial bus interfacing with a cell culture incubator, and (5) a multiplexed microfluidic organoid chip that (6) immobilizes organoids within their micro-environment vessel (1 of 24 wells). To feed the organoids, each individual well is serviced by a fluidic controller; the controller removes spent media via aspiration to a collector in cold storage and then replenishes the vessel with fresh media at programmable intervals.

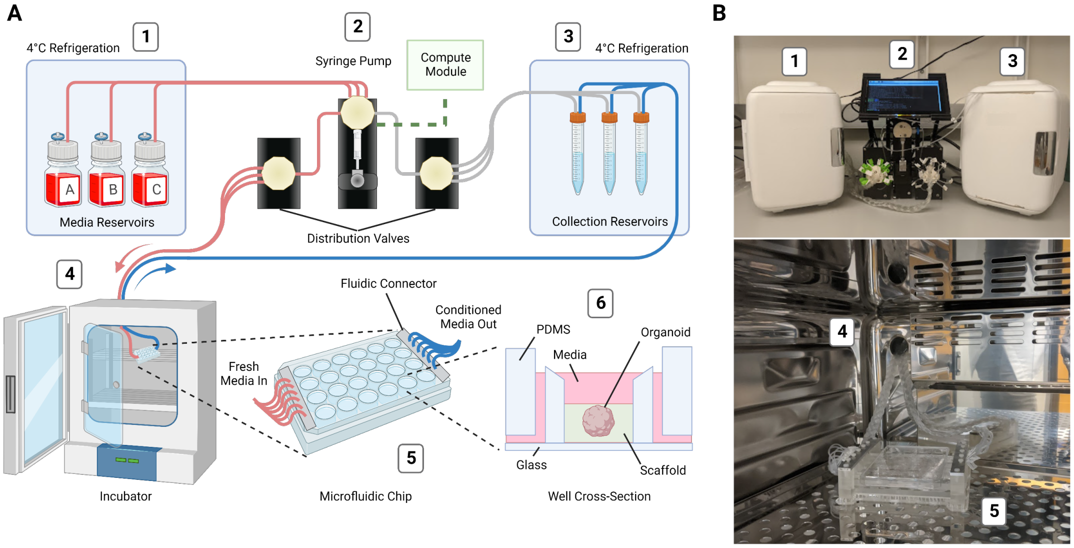

Figure 3.1: Design and implementation of the automated, microfluidic culture platform. **(A)** Illustration of the automated, microfluidic organoid culture platform, the *Autoculture*. **(B)** Front view images of the *Autoculture*. (1) Refrigerator with reagent reservoirs. (2) Syringe pump, distribution valves, and control interface. (3) Refrigerator with conditioned media collection reservoirs. These components reside on a lab bench directly above the cell culture incubator. (4) Microfluidic tubes enter through an incubator port and connect to the (5) microfluidic well plate chip inside the incubator. (6) Cross-sectional diagram of a single well containing an organoid culture.

3.2.1 System design

Each of the 24 wells of this system is a separate, isolated experiment with a dedicated inlet tube, outlet tube, and collection reservoir. Each well's feeding schedule is fully customizable in rate and media to increase the flexibility of experimentation.

A range of 5–1000 µL aliquots from 3 media/reagent reservoirs can be scheduled to any well. Media/reagent reservoirs may also be used in combination. By design, each well forms a fluidic circuit that maintains isolation from the other circuits on the plate (see 3.5 *Methods*). A full 24-well plate is serviced in 72 seconds, and the time between fluid injections may be any length beyond (for instance, every hour, twice a day, every other day, etc.). Conditioned media may be retrieved for molecular analysis without disrupting the culture at any point during or after the experiment. Conditioned media taken for collection are separated from the cultures by an air phase in the outflow fluidic channels to mitigate the risk of infection that may occur from idle medium in the lines. After the experiment, the organoids are retrieved for molecular analysis.

With these control parameters, entire plates may carry out the same workflow to generate consistent batches of organoids. One can also titrate a reagent with an incremental gradient in concentration from well 1 to 24. In addition, one can run multiple protocols/feeding schedules across the plate and change the media components or feeding schedules at various time points throughout an experiment.

3.2.2 Non-expert, user-oriented software

The *Autoculture* is designed to increase the power of the researcher (through multiplex automation) and reduce the complexity of experimentation. Application program interfaces (APIs) are required to convert data from the IoT Cloud, to the on-device compute module, to pump and valve functions, and to serial machine code. A graphical user interface (GUI) will be constructed to assist non-expert users in defining the automated experiment and monitoring progress while the system is running. The Python library, Plotly Dash, or similar GUI designer will be implemented that extends the Python-based software environment. The GUI will be an asynchronous acceptor of data coming from an operator or messaging transport communication.

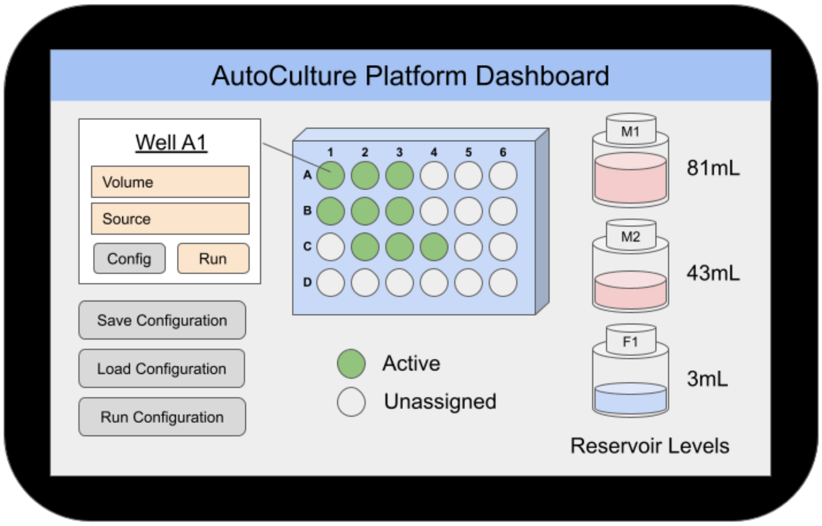

Figure 3.2: Mockup design of a graphical user interface in which individual wells are selectable, experiments are saved and loaded as configurations, and fluid levels of reservoirs are listed on screen. This live view of the experiment will be present on the physical screen mounted on the platform and viewable remotely from a Braingeneer's web IP.

3.2.3 Internet of Things connectivity

Most studies on biology occur in the coordination of several devices to control, perturb, and acquire data from the system. For example, in optogenetics, the incubator is responsible for controlling the environmental conditions for the culture, a probing light source is used to activate light-sensitive channels in the target cells, while a microscope and/or electrode array is used to acquire the readout. Layering more devices permits more tightly controlled experimentation and more data toward a comprehensive interpretation of the system's response. The Amazon Web Services (AWS) Internet of Things (IoT) provides a convenient control framework for multiple devices to communicate information and initiate actions. With a communication protocol such as Message Queuing Telemetry Transport (MQTT), systems can manage synchronized, coordinated efforts of control and data acquisition in real-time over the internet [58]. System-to-system communication occurs over a local area network (LAN), while researchers can make on-demand calls for data or actions remotely. As such, the Autoculture software architecture has control from the AWS Cloud to design, start, pause, edit, and stop experiments on demand (Fig. 3.3).

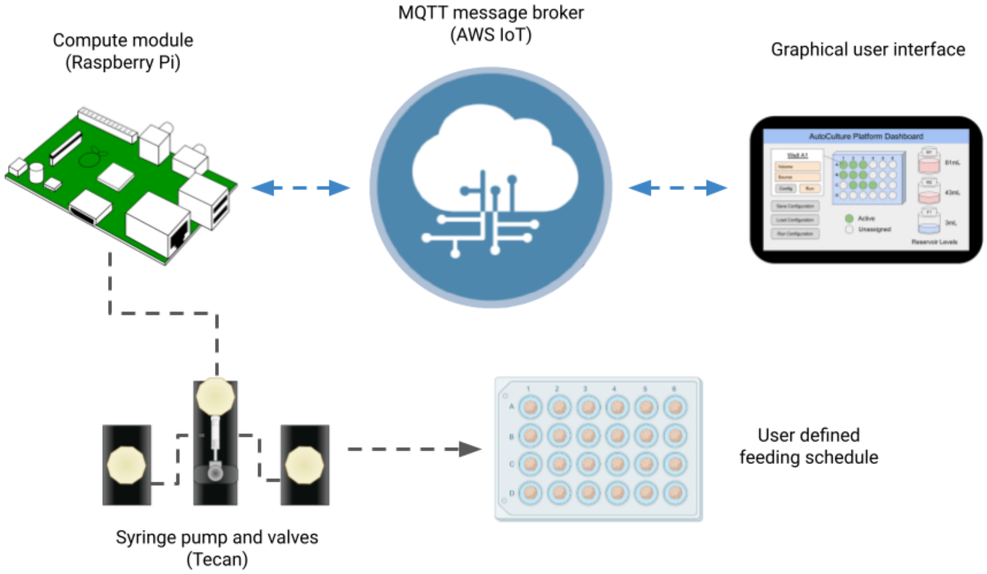

Figure 3.3: IoT Cloud integration: a graphical user interface hosted on the internet relays messages to the Autoculture platform via MQTT to start, monitor, and end experiments.

The Raspberry Pi compute module was used to run experiments locally and accept commands relayed over MQTT. The application program interface (API) used to send serial commands to the Tecan pump and valves was adapted from an open-source Python package [**?**]. Protocols to carry out experiments were developed by timed sequences of unit actions to the pump and valves. In this architecture, IoT connection provides the accessibility to operate experiments remotely while schedules operated locally on-device provide the security of operation in the case of an unstable internet connection. The Braingeneer's group has an existing IoT framework to relay data across devices and to a centalized hub for storage and processing. It is through this network that the *Autoculture* platform can operate in tandem with other devices of control and measurement. What is needed to complete this integration is:

- The retention and broadcast of the platform's state, or "shadow." This serves as the response to status queries.
- The ability to interrupt scheduled actions. This would come as a request to pause/resume all fluidic actions. This is applicable when sensitive measurements are underway or in the case of emergency situations (e.g., if a fluid line were to break and spill on electronics).

3.3 Microfluidic organoid chip

This sub-aim is to produce the *Autoculture*-compatible consumable, microfluidic organoid chip. This section includes the stages of prototyping (3.1.2.1), scaling (3.1.2.2), and characterization (3.1.2.3).

3.3.1 The glass-PDMS chip design

Figure 3.4 describes the manufacturing and assembly process of the PDMS microfluidic chip. The optically-transparent glass-PDMS microfluidic chip has the footprint of a 24-well plate (85.5 mm × 127.6 mm) to integrate with laboratory tools such as microscopes, plate readers, and robotic dispensers. The 24 isolated wells are addressable via 2 mm square channels at the glass-PDMS interface. For convenient accessibility, all inlets are located in a row on the edge of the chip's face and all outlets are located in a row on the opposing edge. The open-loop microfluidic design here contains wells that are open to air. This way, bubbles accumulated in the system are exhausted, there is free gas exchange with the incubator environment, and organoids are easily accessed during chip loading and the experimental conclusion. Each well traps 120 µL that can be used as a micro-environment, including the use of extracellular scaffolds. The inlet and outlet of the fluidic channels are 5 mm above the bottom of the well, which helps mitigate the risk of losing a non-adherent sample into the outflow channel.

Each 3D-printed, fluidic interface plate simultaneously connects 24 lines (Fig. 3.4F). This is a simplification compared to inserting each line individually, which is common for PDMS-based microfluidic. Inside the tube inserts of the fluidic interface plate, three circular barbs seal the Tygon tubing to rigid projections. The tube-bearing rigid projections align to channel access holes of the microfluidic chip. When the collection of 24 lines mate with the molded holes in the PDMS, bore seals form with all the plate projections and the platform tubing lines are aligned to the channels of the microfluidic chip.

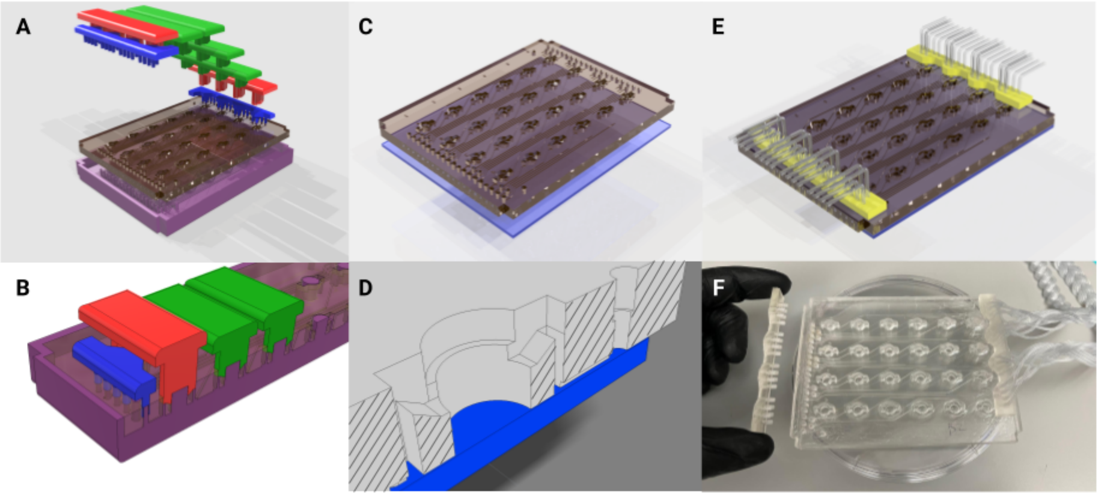

Figure 3.4: Fabrication of the PDMS microfluidic chip. **(A)** Graphical rendering of the interlocking mold pattern for the PDMS substrate in the microfluidic chip assembly. **(B)** Interlocking mounts (blue, red, and green) affix to the base mold (purple) and define microfluidic geometries upon the poured PDMS that are retained as the substrate cures. **(C)** The PDMS substrate is removed from the mold and bonded to glass. **(D)** A cross-sectional rendering of the chip. Fluid enters from microfluidic inlets on the surface and follows channels sealed by glass on the bottom to wells with open access from the top. **(E)** A 3D-printed fluidic interface plate (yellow) connects 24 fluidic microtube lines with the inlets/outlets of the microfluidic chip. **(F)** Microfluidic chip (center) with an example of the fluidic interface plate (left) and fully installed fluidic interface plate (right).

3.3.2 The injection-molded chip design

Once the geometry and functionality was confirmed with the glass-PDMS microfluidic chip (3.1.2.1), we drove down manufacturing and cost using injection molding to generate microfluidic chips. This design is a single layer of injection-molded polycarbonate with the same channel and well size of the glass-PDMS chip. Sealing the channels is a bio-compatible, transparent, pressure-sealed tape that is applied to the underside of the injection-molded chip.

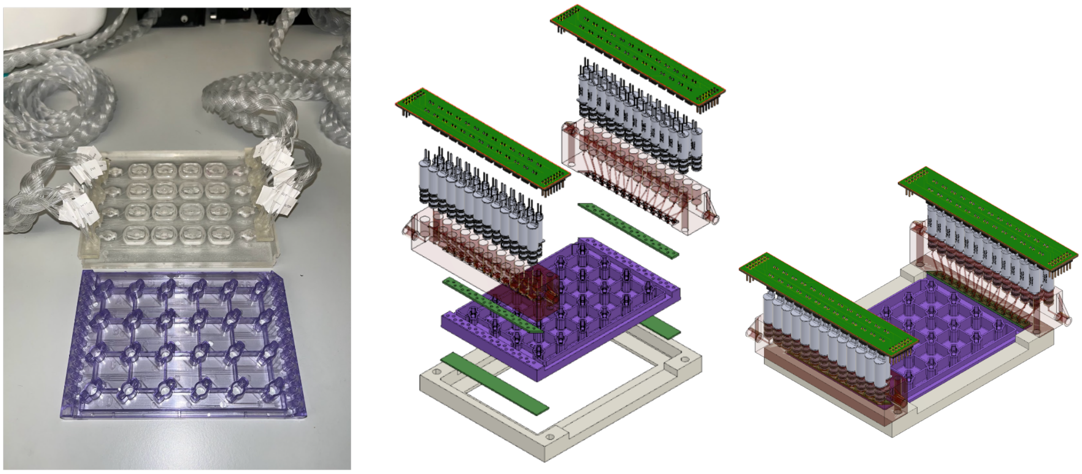

Figure 3.5: The polycarbonate injection-molded microfluidic consumable chip (purple) compared to the glass-PDMS chip (clear) and two renderings of the 24-plex solenoid distribution manifold in exploded and consolidated views.

The injection-molded chip serves as the low-cost consumable component of the experiment. It is designed to integrate with the non-consumable, platform Connector and distribution manifold (Fig. 3.5). Advances in the microfluidic manifold will be discussed in greater detail in sub-aim 3.2.2.1.

3.3.3 Computational fluid dynamics

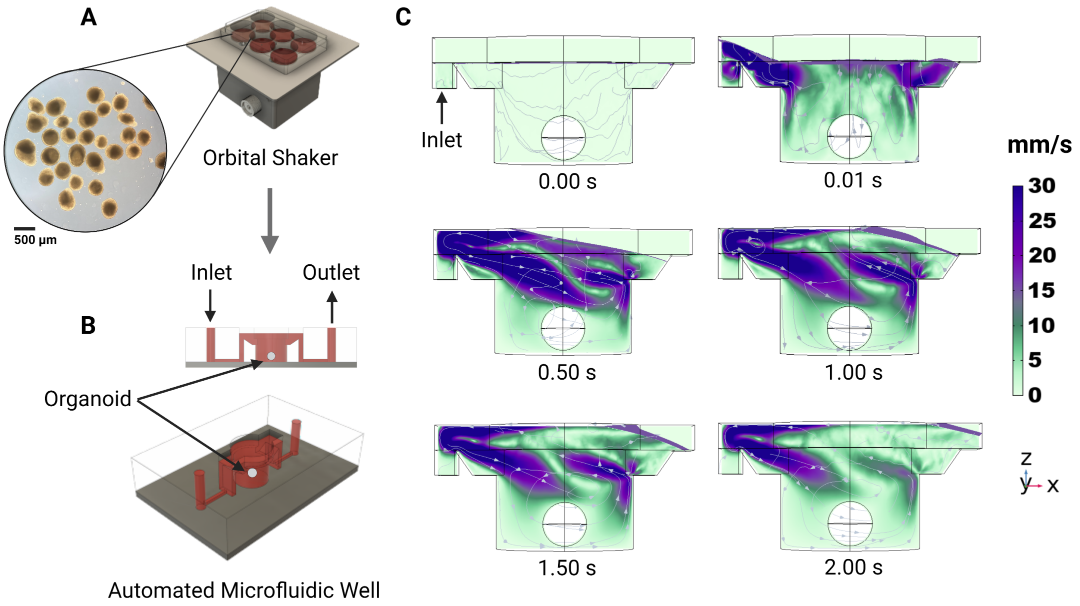

Figure 3.6: Computational fluid dynamics simulated flow in the individual tissue culture wells using the automated system. **(A)** Organoid cultures are expanded on well plates rotated on an orbital shaker. **(B)** After 12 days, organoids are transplanted into the automated microfluidic well. **(C)** One well of the proposed automated system with constant fluid injection over 2 seconds with velocity streamlines.

Conventional cerebral organoid protocols maintain cultures on an orbital shaker. These maintain a quasi-steady velocity regime of approximately 0.12 m/s [79, 24, 93]. We performed a Computational Fluid Dynamics simulation (CFD) using Comsol Multiphysics (Fig. 3.6C), representing the first 2.2 s of media injected into the well. Fluid enters the inlet, 5 mm above the glass floor, and enters the well via a sloped wall. The simulation begins with a media liquid domain filled to the level of the inlet/outlet ports with an air domain existing above. In feeding, media enters the cavity and generates a wave that progresses from the inlet to the outlet. The organoid, modeled as a sphere, fixed 5 mm below the air-media interface, does not observe most of the turbulence generated. The lower (glass) substrate experiences <5% of the maximum velocity during feeding. The velocities in this regime are instantaneous (as opposed to quasi-steady-state) and two orders of magnitude less than that of orbital shakers, inducing lower velocities and less shear stress upon the culture. One of the advantages of this system is that researchers can tailor the media flow rate and delivery schedule to achieve optimal diffusion of the nutrients with minimal disruption to the organoid.

3.4 System validation with cerebral organoid culture

This sub-aim is to quantify the quality of organoid cultures produced on the *Autoculture* platform (3.1.1) with the microfluidic chip (3.1.2). This section includes details of experimenting on the platform (3.1.3.1), taking live images concurrently (3.1.3.2), and experimental results (3.1.3.3).

3.4.1 Automated culture of cerebral organoids

The growth of cerebral organoids on Autoculture was compared to that of orbital shaker conditions in an 18-day experiment. Human pluripotent stem cells were aggregated to form organoids and maintained under standard conditions for the first 12 days during neural induction (see "Methods"). The batch was split, and 12 organoids were loaded onto an Autoculture microfluidic chip while the remainder were maintained in a 6-well plate on an orbital shaker as controls. Each well was pre-loaded with 50 µl Matrigel immediately before loading the organoids to adhere each organoid at the center of the well (see “Methods”). The automated organoids were fed 70 µL every hour for six days, while the controls were fed 2 mL every other day. In automation, the well plate does not need to be periodically removed from the incubator for feeding; therefore, this system is well-suited for longitudinal monitoring of organoid development. In this study, organoids in the Autoculture well plate were monitored once per hour using a bright-field imaging in-incubator platform [48, 4].

3.4.2 Live imaging with *Picroscope* integration

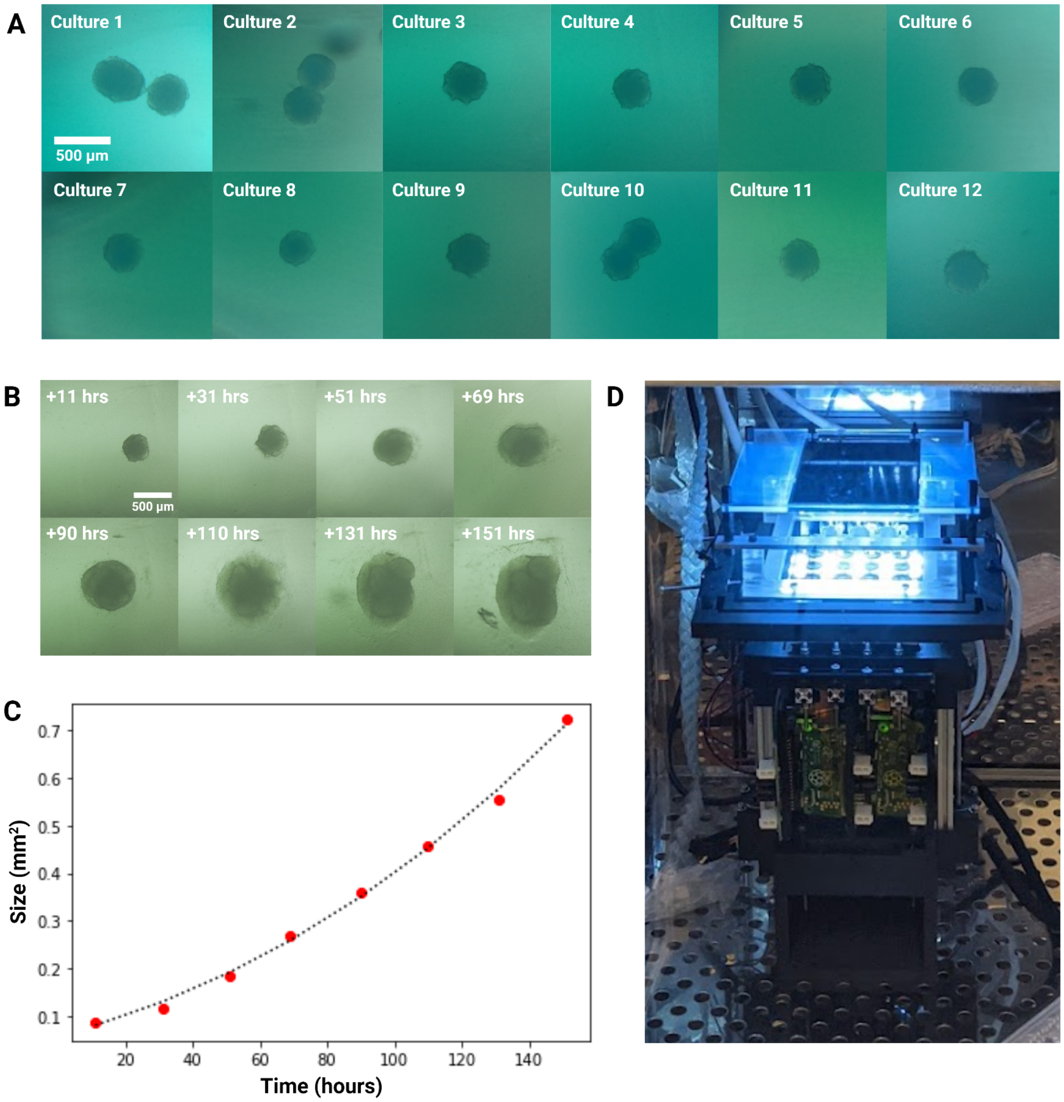

Figure 3.7: Longitudinal monitoring of organoid development. **(A)** Bright-field images of twelve individual 12-day-old cerebral cortex cultures at day 1 of automated feeding. **(B)** Longitudinal imaging of "Culture 4" during the experiment. **(C)** Projected area expansion of "Culture 4" during the experiment. This was obtained using a computer vision algorithm[48]. **(D)** The *Autoculture* microfluidic chip sits on a remote-controlled, IoT-enabled, 24-well automated imaging system.

Figure 3.7D shows the automated, microfluidic culture plate inside an incubator placed on a remote-controlled, IoT-enabled, multi-well automated imaging system. The imaging system was designed to monitor biological experiments in a 24-well plate format, using one dedicated camera for each well. To account for the three-dimensional development of the organoids during the entire experiment, we captured bursts of images, sweeping through the range of focal distances covering the entire three-dimensional tissue. A computer vision algorithm was used to detect the features in focus at each focal plane, generate a composite image maximizing the in-focus features in the entire organoid, and compute the projected area. This process is described in previous work [4]. Figure 3.7A shows 12 cerebral cortex organoid cultures (day 12), loaded in individual wells of the microfluidic chip and fed in parallel on the Autoculture platform for the experiment. Figure 3.7B and C show the growth of "Culture 4" over six successive days. Robust organoid growth was observed for the organoids in the Autoculture wells and was consistent with the size increase observed for the organoids grown under control conditions. Compared to controls, automated organoids did develop a less-dense perimeter, suggesting that the reduction in velocities and shear forces may accommodate growth and migration that would otherwise be cleaved.

3.5 Methods

Design of the *Autoculture* platform

Cell culture media was stored in glass bottle reservoirs (Corning) with a multi-port solvent delivery cap (Spex VapLock) and stored at 4°C for the duration of the experiment. Each reservoir delivery cap contained a single 0.030" ID x 0.090" OD Tygon microbore tube (Masterflex), sealed by a two-piece PTFE nut and ferrule threaded adapter (Spex VapLock), extending from the bottom of the reservoir to an inlet port on the 6-port ceramic valve head of the syringe pump (Tecan Cavro Centris, 1.0-mL glass vial). Sterile air is permitted to backfill the reservoir through a 0.22-µm filter (Millipore) affixed to the cap to compensate for syringe pump reagent draws. The same Tygon microbore tubing and PTFE nut and ferrule threaded adapters were used to connect the syringe pump to two parallel 12-port distribution valves (Tecan SmartValve). Each 0.020" ID x 0.060" OD Tygon microbore tube (Masterflex) emanating from the distribution valve connects to a single well of the microfluidic chip. Fluidic isolation between wells is retained from this junction onward. Each 12-port distribution valve services six wells on the microfluidic chip. Systems with two and four distribution valves were constructed. The collection of 2-meter long microbore tubes was bundled into a braid for convenient handling and guided through the rear entry port of a standard cell culture incubator (Panasonic) (Figure 3.1(4)). At incubator conditions (37°C, 5% CO2, 95% rel. humidity), a single custom, 3D-printed fluidic interface plate mated the set of microbore tubes for reagent delivery to the inlets of the microfluidic chip and a second, identical interface plate mated the set of microbore tubes for reagent aspiration to the outlets.

The microbore tubes for aspiration were guided back out of the incubator and to a set of single-use 15-mL conical tubes (Falcon) for conditioned media collection (Figure 3.1(3)). Each collection reservoir was capped with a rubber stopper (McMaster) containing two 0.06” drilled holes. For each stopper, the microbore tube sourcing conditioned media from the microfluidic chip was inserted into one hole, and a dry microbore tube for pneumatic operation routes back to the aspiration distribution valve head was inserted into the other hole. The syringe pump was used to generate negative pressure upon each collection reservoir in series to draw conditioned media from the microfluidic chip into the collection reservoir. The separation between the pneumatic tube and conditioned media tube trapped the influx of media in the collection reservoir. All microbore tubes were hermetically sealed to the distribution valve and syringe pump with PTFE nut and ferrule threaded adapters.

The syringe pump and distribution valves were connected using the multi-pump electrical wiring configuration described in the Tecan manual. A compute module (Raspberry Pi 4) relayed serial communications with Tecan OEM Communication Protocol using a GPIO TX/RX to DB9M RS232 serial expansion board for Raspberry Pi (Ableconn). The Raspberry Pi compute module used a 7” touchscreen display to edit and launch protocols. An open-source Python application program interface (API) was used to develop the software required to carry out protocols in automation.

PDMS Molding

PDMS-based microfluidics were constructed using an interlocking 3D-printed plastic mold (Figure 3.4). These were printed with an SLA printer (Formlabs Form 3) with Model V2 resin. The printed molds were post-processed with sonication in isopropanol (IPA) for 20 minutes to remove excess resin, followed by drying in N2. Dry components were cured under UV-light (405nm) for 30 minutes at 60°C. As illustrated in Figure 3A, the mold parts were assembled and filled with PDMS (Sylgard 184, Dow Corning) prepared by mixing PDMS prepolymer and a curing agent (10:1 w/w). After filling the mold, the PDMS was degassed in a vacuum chamber for 1 hour. The PDMS-filled mold is left to cure for 24 hours at 60°C before removal of the PDMS from the mold.

Microfluidic Chip Assembly

Borosilicate glass substrates (101.6mm x 127.0mm, McMaster-Carr) were cleaned via sonication in acetone (10 minutes), then isopropyl alcohol (10 minutes), and dried with N2. The glass substrate and molded-PDMS surface were activated with oxygen plasma at 50W for 45 seconds. The glass and PDMS (Figure 3.4C) were aligned by hand, pressed together, and baked at 100°C on a hot plate for 30 minutes, forming an irreversible seal.

Parylene Coating

A 10 µm layer of parylene-C (Specialty Coating Systems) was deposited onto the microfluidic chip to prevent PDMS absorption of small molecules. Two drops of silane A-174 (Sigma-Aldrich) were loaded into the deposition chamber to promote adhesion.

3D Printed Components

The fluidic interface plate (Figure 3.4F) was 3D printed to interface the 2.2 mm OD microbore tubing (Cole-Palmer) with the PDMS inlet and outlet features. Each connector geometry consisted of 24 cylindrical extrusions with an OD of 2.7 mm and a bore of 2.2 mm. Within each bore were three 0.2 mm long barbs to grip the microbore tubing when inserted. This component was printed with a Formlabs SLA printer (Form 2) with Surgical Guide resin with sonication in isopropanol (IPA) for 20 minutes to remove excess resin, followed by drying in N2. Dry components were then cured under UV light (405 nm) for 30 minutes at 60°C. To ensure biocompatibility, the part was coated with 5 µm of parylene-C (Specialty Coating Systems). Two drops of silane A-174 (Sigma-Aldrich) were also loaded in the deposition chamber with the device to promote adhesion.

Sterilization

Sterilization of the syringe pump, valve heads, tubing, fluidic interface plates, and collection tube caps was carried out per supplier recommendation (Tecan). A 10-

minute wash with 70% ethanol sourced from an autoclaved glass reservoir was pushed through the platform to the collection reservoirs via the syringe pump. Following 70% ethanol, a drying cycle of sterile air sourced through a 0.22 µm filter (Millipore) was applied for 10 minutes. Ten subsequent cycles of deionized, nucleus-free water and drying were carried out under the same parameters. The microfluidic chip and media reservoirs were autoclaved at 121°C for 45 minutes and dried for 15 minutes immediately prior to use. All components were transferred via sealed autoclavable bags to a biosafety cabinet in tissue culture for organoid and media loading. Pre-prepared, supplemented media was transferred to each media reservoir and capped (VapLock) and then stored in refrigeration for the duration of the experiment.

hESC line maintenance

The human embryonic stem cell line H9 (WiCell, authenticated at source) was grown on recombinant human vitronectin (Thermo) coated cell culture dishes in StemFlex Medium (Gibco). Subculturing was performed by incubating plates with 0.5 mM EDTA for 5 minutes and then resuspended in culture medium to be transferred to new coated plates.

Cerebral organoid differentiation and protocol

To generate cerebral organoids, adherent cultures were dissociated into single cells using Accutase Cell Dissociation Reagent (Gibco) and then aggregated in AggreWell 800 24-well plates (STEMCELL Technologies) at a density of 3,000,000 cells per well with 2mL of AggreWell Medium (STEMCELL Technologies) supplemented with Rho Kinase Inhibitor (Y-27632, 10 µM, Tocris, 1254) (day 0). The following day (day 1), 1mL of the AggreWell medium was manually replaced with supplemented medium containing WNT inhibitor (IWR1-ε, 3 µM, Cayman Chemical, 13659, days 1-10) and Nodal/Activin inhibitor (SB431542, Tocris, 1614, 5 µM, days 1-10). On day 2, aggregates were transferred onto a 37 µm filter (STEMCELL Technologies) by carefully aspirating with a p1000 wide-bore pipette out of the AggreWell plate. The organoids were transferred into ultra-low adhesion 6-well plates (Corning) by inversion and rinsing of the filters with fresh AggreWell medium. Media was changed on days 3, 4, 5, 6, 8, and 10 by manually replacing 2 mL of conditioned media with fresh media. On day 11 and onward, the medium was changed to Neuronal Differentiation Medium containing Eagle Medium: Nutrient Mixture F-12 with GlutaMAX supplement (DMEM/F12, Thermo Fisher Scientific, 10565018), 1X N-2 Supplement (Thermo Fisher Scientific, 17502048), 1X Chemically Defined Lipid Concentrate (Thermo Fisher Scientific, 11905031) and 100 U/mL Penicillin/Streptomycin supplemented with 0.1% recombinant human Fibroblast Growth Factor b (Alamone F-170) and 0.1% recombinant human Epidermal Growth Factor (R&D systems 236-EG).

Control-group "Suspension" organoids remained suspended in 6-well plates and were maintained with 2 mL media changes every other day for the remainder of the culture. Experimental-group "Automated" organoids were loaded onto the microfluidic chip and experienced media changes of 70 µL once every hour for the remainder of the culture.

Microfluidic chip loading

On day 12 of cerebral organoid differentiation, the microfluidic chip was prepared by pipetting 50 µL of chilled (approximately 0°C) Matrigel hESC Qualif Matrix (BD 354277) into each well. Immediately following Matrigel, single cerebral organoids were transferred via p1000 wide-bore pipette with 70 µL of native conditioned media to each well and positioned to center-well for imaging. The chip was covered with a 24-well plate lid and incubated at 37°C for 15 minutes to set the Matrigel. Each well was filled with an additional 70 µL of fresh media and connected to fluidic interface plates (Figure 3.4F) routed into the incubator through a rear access port. The fluidic interface plates were pressure fitted into the microfluidic chip by hand, and the chip was positioned on the imaging platform (if applicable).

Computational fluid dynamics

The fluid dynamics of filling and draining the wells were predicted using a commercial Computational Fluid Dynamics software COMSOL® Multiphysics 5.5 (Stockholm, Sweden). Figure 3.6B shows the first 2 seconds of the filling cycle ($70\mu L$ of media delivered with an average velocity of 9.85×10^4m/s). The well is 5mm deep and has a diameter of 5.6mm. In this simulation, the media properties were $997kg/m^3$ density and 6.92×10^3kg/m.s viscosity. The simulation predicts the phase boundary (between liquid and air) as a free surface [**?**]. The solution domain consists of a rigid wall (the well) with "non-slip" boundary conditions and the top surface (the air-media interface) open to the incubator with "slip" boundary conditions. The organoid was simulated as a phantom sphere geometry with a 1.8mm diameter. Atmospheric conditions were set to a pressure of 1atm, a temperature of 37°C, and a gas composition of 5% carbon dioxide, 17% oxygen, and 78% nitrogen. We visualized the velocity field on the central vertical cross-section of the well using stream arrow lines. The simulation used a total of $519,830$ tetrahedral elements.

3.6 Conclusion

The Autoculture platform represents a significant advancement in cerebral organoid culture technology. Our results demonstrate that this automated microfluidic system can support the growth and development of cerebral organoids while potentially reducing cellular stress compared to conventional methods. Key findings from this study include:

- Successful design and fabrication of a modular, scalable microfluidic platform for organoid culture
- Development of custom microfluidic chips that provide a controlled microenvironment for individual organoids
- Integration of the platform with live imaging capabilities for continuous monitoring of organoid development

These results suggest that the Autoculture platform may provide a more physiologically relevant environment for cerebral organoid growth. The reduction in stress markers without compromising differentiation fidelity indicates that this system could lead to improved organoid models for studying brain development and disease. While the prototype demonstrates promising results, we have identified areas for further improvement, including enhancing the reliability of fluid handling and developing more robust connection interfaces. Future work will focus on addressing these limitations and expanding the capabilities of the system to include additional sensing modalities and feedback mechanisms. The Autoculture platform lays the groundwork for more sophisticated, high-throughput organoid studies and represents a significant step towards standardizing and optimizing cerebral organoid culture for research and potential therapeutic applications.

Chapter 4

Monitor and Optimize the Metabolic Health of Cerebral Organoids

4.1 Introduction

Building upon the successful development and validation of the *Autoculture* platform described in Aim 1 (Chapter 3), we now turn our attention to leveraging this technology to improve the metabolic health of cerebral organoids. Our initial results suggested that automated culture conditions could reduce the expression of stress-related genes in organoids. This finding raises intriguing questions about the potential to further optimize culture conditions to create more physiologically relevant organoid models.

In Aim 2 here, we explore the hypothesis that increasing the feeding frequency and adjusting the composition of the medium can significantly reduce metabolic stress in cerebral organoids, bringing their cellular state closer to that of *in vivo* brain tissue. This aim is divided into three main objectives:

- Investigate the effects of increased feeding frequency on organoid health with RNA-seq
- Reformulate cell culture media constituents, particularly controlling for glucose levels, towards physiological relevance
- Characterize long-term metabolic profiles of cerebral organoids under reformulated conditions

By studying these factors, my aim was to develop a more comprehensive understanding of organoid metabolism and establish culture protocols that minimize artificial stress responses. This work has the potential to enhance the fidelity of cerebral organoid models, making them more suitable for studying brain development, disease modeling, and drug screening.

4.2 Effects of feeding frequency on organoid health

4.2.1 Growth analysis with immunofluorescence and RNA-seq

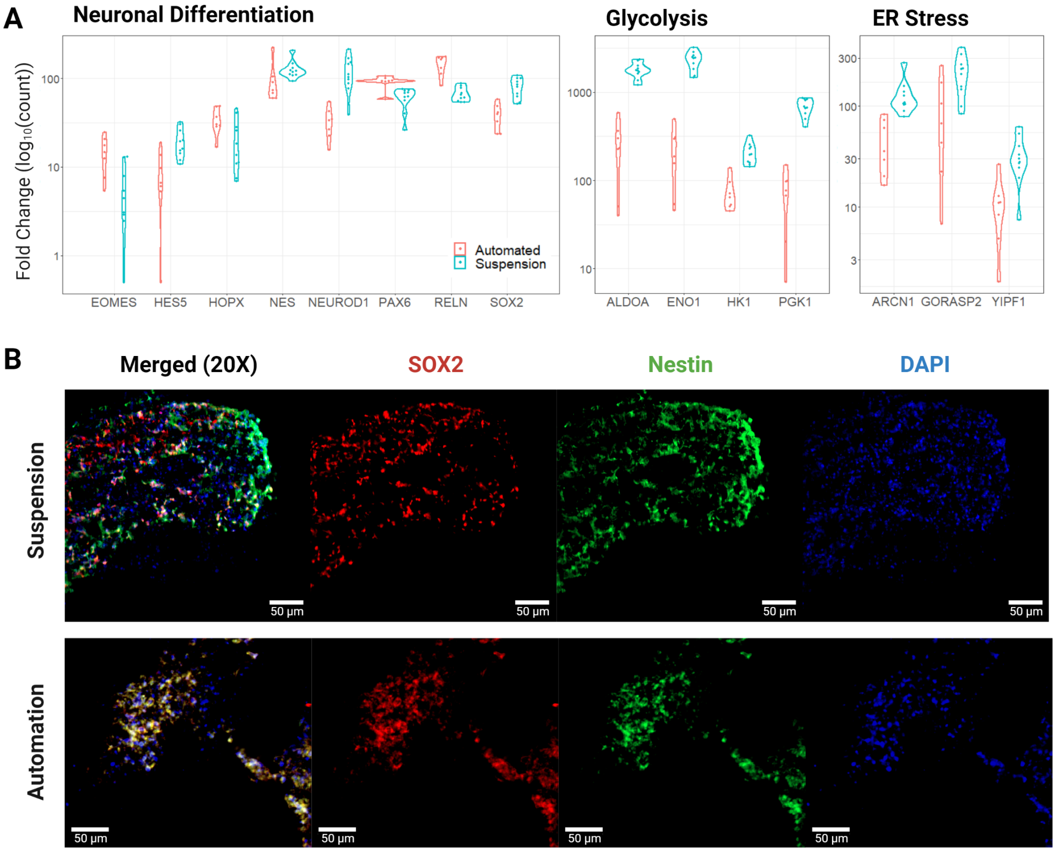

Figure 4.1: Transcription and immunofluorescent imaging results. **(A)** Pairwise comparisons of expression for select genes associated with neural differentiation, glycolysis, and ER stress. Results were statistically significant with an adjusted p-value <= 0.05, except for HOPX and NES of neural differentiation. The "Automated" data represent 7 biological replicates and the "Suspension" data represent 4 biological replicates with 6 technical replicates **(B)** Immunofluorescent stains for SOX2, Nestin, and DAPI of Suspension and Automated organoid sections show congruent progenitor markers.

To analyze the effects of Automation versus Suspension cultures in the previously discussed study [84], on day 18, the cultures were harvested and analyzed by bulk RNA sequencing (RNA-seq) and immunohistochemistry to evaluate the cell types generated in each condition and the overall health of the cell cultures. The transcriptomes of 7 "Automated" and 4 "Suspension" organoids were compared. Gene expression of cell-type markers for neuralepithelia (SOX2), radial glia neural stem cells (SOX2, HES5, PAX6, HOPX), intermediate progenitors (TBR2/EOMES), and immature neurons (NeuroD1, RELN) did not show consistent differences between the Autoculture and control samples suggesting that overall differentiation fidelity was not affected by using the Autoculture system (Fig. 4.1A). Consistent with this, we saw a robust expression of the neural progenitor protein markers, SOX2 and Nestin by immunohistochemistry in sections of organoids grown under standard or Autoculture conditions (Fig. 4.1B).

Contrasting automated and control organoids, we observed a significant difference in the expression of genes associated with cell culture stress. Studies have shown that the glycolysis and endoplasmic reticulum stress (ER stress) pathways are up-regulated in organoids relative to in vivo tissue samples, and are correlated with altered cell subtype specification and maturation [68, 6]. In this study, canonical glycolysis was the top differential pathway, with the vast majority of the significant genes consistently down-regulated (see Supplementary Tables 2 and 3 of [84]). Genes that are notably up-regulated in cerebral organoids showed reduced levels in the automation condition: ALDOA, ENO1, HK1, and PGK1 had fold changes of -6.9, -10.4, -2.8, and -9.3, respectively (Fig. 4.1A). Additionally, markers of ER stress: ARCN1, GORASP2, and YIPF1 were reduced by fold changes of −2.8, −2.2, and −3.0, respectively. See Supplementary Table 4 of [84] for more differentially expressed genes of ER stress.

There was also significant difference observed in the master transcription factor for hypoxia (HIF-1). In the automated condition, organoids had a −2.2 fold change (adjpval of 7.04E-4) in HIF-1 alpha compared to control. Additionally, the data suggests less directed autophogy of the mitochondria. The top differentially expressed gene was BCL2/adenovirus E1B 19 kDa protein-interacting protein 3 (BNIP3) that was reduced in automation by a fold change of −9.9 (adjpval of 3.03E-62). BNIP3 modulates the permeability state of the outer mitochondrial membrane by forming homo- and hetero-oligomers inside the membrane [80]. Presence of BNIP3 results in a decrease in mitochondrial potential, an increase in reactive oxygen species, mitochondrial swelling and fission, and an increase in mitochondrial turnover via autophagy [46].

The most significant results of differential expression for this experiment [84] were in the down-regulation of stress pathways for automated organoids. Genes that DGE showed up-regulated in Automated organoids were MUC16, CYP4F8, and HMOX1. Mucin 16, cell surface associated (MUC16) (log2FC = 1.35, adjpval = 5.72E-11) is a gene that encodes a mucin-member, O-glycosylated protein that plays a role in forming a protective mucous barrier, found on the apical surfaces of the epithelia. Much of the brain is not epithelial, however, ependymal cells are ciliated-epithelial glial cells that develop from radial glia along the surface of the brain's ventricles and spinal canal. They play a critical role in cerebrospinal fluid (CSF) homeostasis, brain metabolism, and the clearance of waste [49]. The gene, CYP4F8 (log2FC = 1.97, adjpval = 1.20E-7), encodes the Cytochrome P450 4F8 protein, a member of the cytochrome P450 superfamily of enzymes. This protein localizes to the endoplasmic reticula and is monooxygenase which catalyzes many reactions involved in drug metabolism and synthesis of cholesterol, steroids and other lipids [7] Heme oxygenase (HMOX1) (log2FC = 2.58, adjpval = 1.88E-7), is an essential enzyme in heme catabolism that cleaves heme to form biliverdin, carbon monoxide, and ferrous iron. For its role in oxidative cleavage, it plays an important role in reducing vascular inflammation.

4.3 Adaptive glucose study: Optimization of cell culture medium

Cell culture practices, first developed in the mid-twentieth century, were optimized for cancer cell expansion. Many of these early media formulations (e.g., Dulbecco's Minimum Essential Medium, Ham's F-12 Medium) are still used today. While these media support growth and have been foundational to cell biology, they do not reflect physiological concentrations that cells experience in primary tissue. Recent reformulations, such as BrainPhys, aim to mimic physiological concentrations. However, metabolically active cells quickly alter these conditions through nutrient consumption and waste excretion. Prior research has shown that stem cell-derived cerebral organoids differ from primary cerebral cortex tissue, notably in upregulating glycolysis and endoplasmic reticulum stress while down-regulating oxidative phosphorylation. These metabolic differences correlate with downstream issues in cell type fidelity and differentiation.

In order to optimize metabolic health, definition needs to be brought to the metabolic profile as it changes in time for developing cerebral organoids. Here, metabolic profile refers to the concentrations of metabolically active analytes that influence cell respiration, stress, and survival. The environment in which cells multiply, differentiate and expand in 3D space all influence nutrient requirements and stress response to waste by-products for cerebral organoids. By tracking metabolic analytes, we gained an understanding of the metabolic requirements and trajectories of cerebral organoid cultures. Key features of cell culture exist that suggest major influences on cerebral organoid metabolism. These include:

- **Size-dependent correlations.** It has been proposed in literature that the volumetric size of organoids poses a major constraint in shuttling oxygen to sub-surface cells [66]. If this constraint were a major influence, the data would likely show a spike in anaerobic glycolysis markers starting a 1.4mm diameters [51] and increasing thereafter.

- **Cell-type correlations.** At aggregation, the cultures are predominantly composed of stem cells. Over the expansion stage, many differentiate into progenitors, glia, and early neurons. Each of these cells have different metabolic requirements and functions. It may be the case that changes in metabolic analyte concentrations best correlate with the presence of particular cell types. This study will record changing populations.

- **pH effects.** Cell supernatant alkalinity plays a pivotal role in intracellular reactions. Fluctuations or minimal/maximal tolerances may correlate best with acute changes in metabolic health.

Metabolic analyte	*In vivo* reference concentration	Measurement instrument
D-glucose	3.9-7.2 mM (blood) 2.8-4.4 mM (CSF)	Vi-CELL MetaFLEX
Lactate	1.4-2.3 mM (blood) 2.1–4.44 mM (CSF)	Vi-CELL MetaFLEX
pH	7.350-7.450 (blood) 7.317-7.324 (CSF)	Vi-CELL MetaFLEX
Pyruvate	0.19-0.22 mM (blood) 0.03–0.15 mM (CSF)	Fluorometric assay kit
Acetyl-Coenzyme A	272.86 nM (220.9 ng/mL) (blood)	Fluorometric assay kit (10-1000 pmole sensitivity)
Lactate dehydrogenase	135–225 U/L (blood) 10–50 U/L (CSF)	Fluorometric assay kit (Lactate Dehydrogenase activity assay kit)

Table 4.1: Table of key metabolic analytes their physiological ranges. References for the concentrations in cerebrospinal fluid [83]. Acetyl-CoA resides primarily in the mitochondria of the cell and has a minimal concentration in the extracellular space [94].

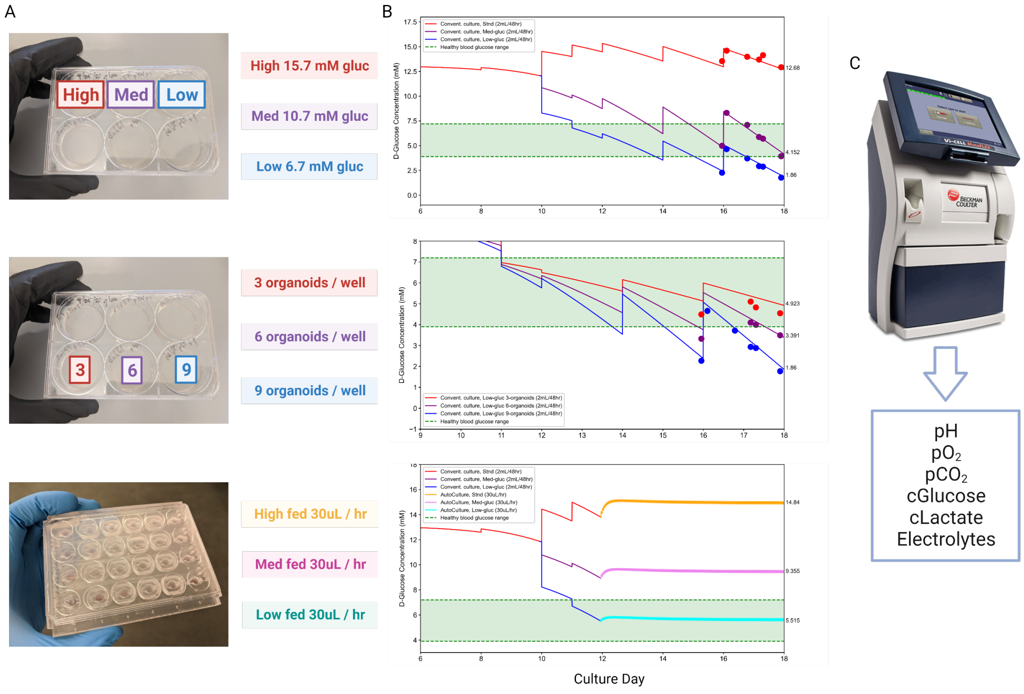

Figure 4.2: Model of cell supernatant glucose concentrations over time with different well conditions. **(A)** Images of three plates, each with different conditions: a 6-well suspension plate with wells at high glucose (15.7 nM), medium glucose (10.7 mM), and low glucose (6.7 mM); a 6-well suspension plate with wells containing 3 orgnaoids, 6 organoids, and 9 organoids; and a glass-PDMS microfluidic chip with high, medium, and low glucose concentrations all fed at 30uL aliquots per hour. **(B)** Thee graphed, computational models of glucose concentration over time (days in culture) that model each of the three well conditions. The green band denotes the range of healthy blood glucose (3.9 mM to 7.2 mM). The healthy range for cerebrospinal fluid is even less (2.8 mM to 4.4 mM). **(C)** Dots in the graphs represent bioanalyte measurements taken from the cultures and recorded using the Vi-CELL MetaFLEX. This instrument measures pH, the dissolved partial pressures of O2 and CO2, and the concentrations of glucose, lactate, K+, Na+, Ca2+, and Cl-.

The follow sections follow the procedures and results of the ”Adaptive Glucose” study. This experiment was set up with expert collaborators, in particular Ryan Hoffman, to resolve the effects of glucose concentration on long-term cerebral organoid differentiation.

4.3.1 Hypothesis and experimental design

The central hypothesis of this experiment is that non-physiological and highly variable cell culture media analyte concentrations (pH, glucose, lactate) degrade the cerebral organoid model. We posit that optimizing one of these factors (glucose) and sustaining it throughout organoid development will yield cerebral organoids that better mimic primary cerebral cortex tissue.

We established six experimental conditions:

1. Control 1 ”DMEM/F12” (+) EGF FGF: Classic, directed differentiation akin to Sasai cerebral organoids (High Glucose”).
2. Control 1 ”DMEM/F12” (-) EGF FGF: Control 1 without growth factors.
3. Control 2 ”BrainPhys (+) EGF FGF: Modern, directed differentiation akin to Galina cerebral organoids (Physiological Glucose”).
4. Control 2 ”BrainPhys” (-) EGF FGF: Control 2 without growth factors.
5. Experimental ”Adaptive Glucose” (+) EGF FGF: Continually adjusting glucose supplement to maintain optimal concentration.
6. Experimental ”Adaptive Glucose” (-) EGF FGF: Adaptive glucose experimental without growth factors.

To forecast metabolic changes, we initiated a ”Leading Plate” following the Adaptive differentiation condition, one passage (5 days) ahead of the main cohort.

We used the Vi-CELL MetaFLEX to evaluate cell supernatant pH, pO_2, pCO_2, glucose, lactate, and electrolytes. The Controls cerebral organoids were generated using established protocols, with modifications to the ECM treatment schedule.

Key timepoints included:

- Day 0-18: Initial aggregation and early differentiation
- Day 18: First RNA harvest and transition to experimental conditions
- Day 35: Growth factor removal and second "five week" RNA harvest
- Day 70: Third "ten week" RNA harvest
- Day 105: Final "fifteen week" RNA harvest

The number of organoids per well were quantified and controlled. Post-aggregation, orgnaoids were kept at 20 organoids per well (6-well plate). Throughout the experiment, we collected conditioned media for extracellular vesicle (EV) analysis, performed RNA sequencing, conducted cell counts, and carried out immunohistochemistry.

We anticipated that the "Adaptive Glucose" condition would produce organoids with metabolic profiles more closely resembled to *in vivo* tissue, potentially improving the fidelity and differentiation of cell types. This study aims to establish a new standard for cerebral organoid culture, emphasizing the importance of maintaining physiological metabolite concentrations throughout development.

4.3.2 The adpative glucose calculator

Homeostasis is a technically challenging task for experiments and biology itself. Control 1 (”DMEM/F12”) and Control 2 (”BrainPhys”) were conditions with predetermined media formulations; however, the ”Adaptive Glucose” experimental condition required constant adjustment to maintain the physiological band. Central to the ”Adaptive Glucose” experimental condition were two constraints:

1. Cultures may never exceed 10 mM concentration of glucose
2. Cultures may never experience the absence of glucose (0 mM)

To accomplish this, glucose concentration data drawn from the Vi-CELL MetaFLEX was used to meter glucose consumption and calculate the glucose supplement spike-in to maintain the experimental constraints.

4.4 Adaptive glucose study: Long-term metabolic profiles

Our long-term study of cerebral organoid metabolism under different glucose conditions revealed several key findings. As shown in Figure 4.3, organoids in the Adaptive glucose condition demonstrated a more stable glucose consumption rate over time compared to the high-glucose (DMEM/F12) and physiological glucose (BrainPhys) conditions. Organoids in the adaptive glucose condition showed less fluctuation in metabolic markers over time, suggesting a more stable and potentially less stressful metabolic environment.

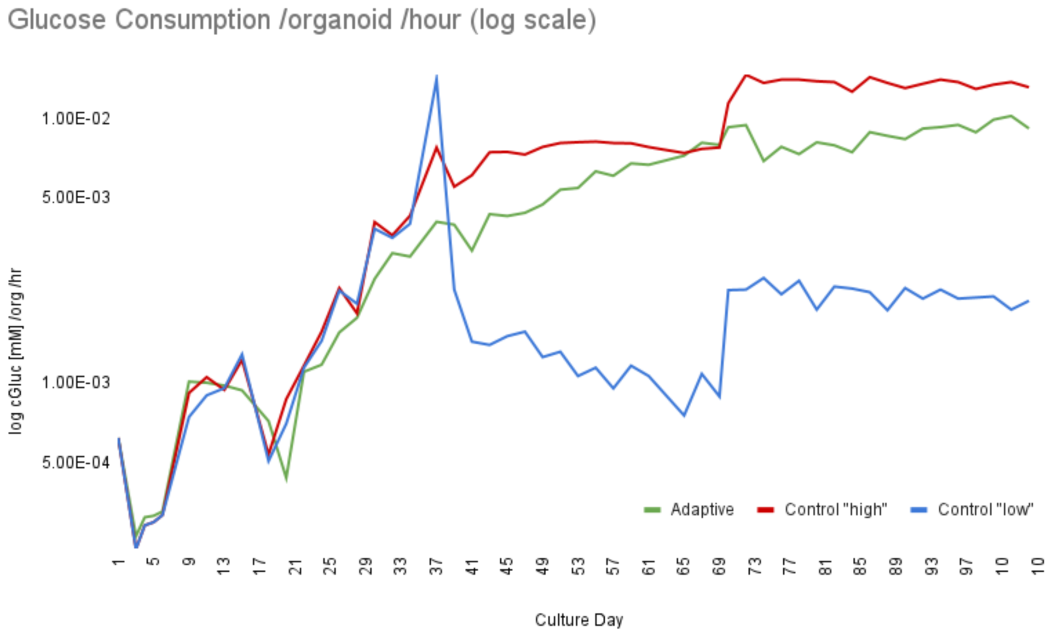

Figure 4.3: Graph of glucose consumption over 105 days per organoid, per hour.

The presence or absence of EGF and FGF appeared to influence metabolic profiles, with growth factor-supplemented conditions showing higher overall glucose consumption but potentially more variability in metabolic markers. We observed distinct metabolic phases across all conditions, with notable shifts occurring around days 18-20 and days 35-40. These time points coincide with key developmental stages in cerebral organoid maturation, suggesting a link between metabolic changes and cellular differentiation events.

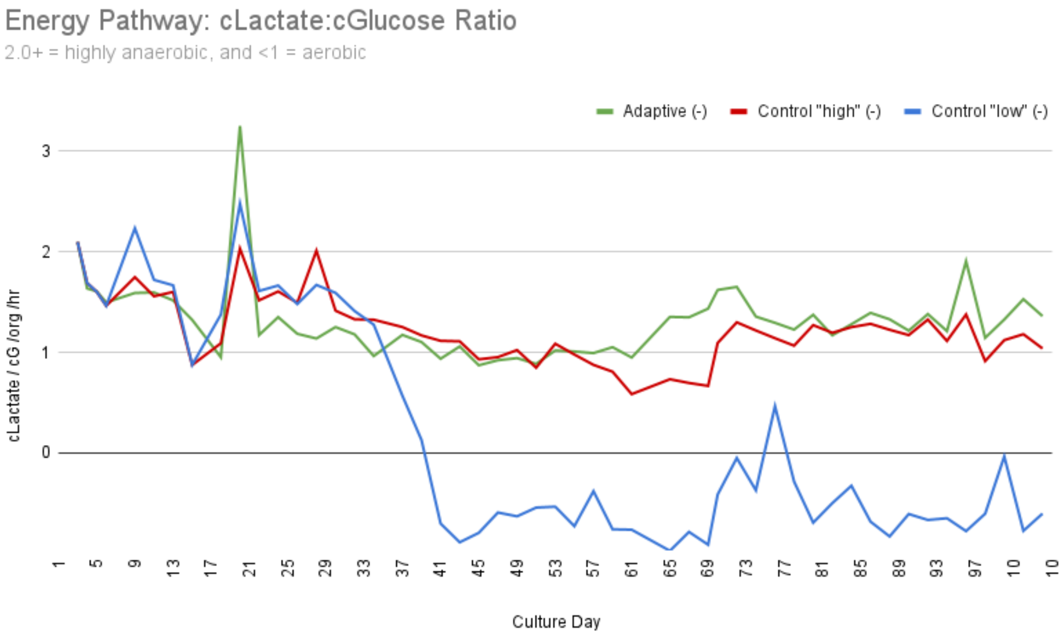

Figure 4.4: Graph of the lactate:glucose ratio. The amount of lactate produced in relation to glucose consumed indicates the energy consumption pathway.

Figure 4.4 illustrates the changes in the lactate:glucose ratio over the 105-day culture period. The adaptive glucose condition maintained a lower and more consistent ratio compared to the other conditions, particularly after day 35. This indicates a potentially more efficient aerobic metabolism and less reliance on anaerobic glycolysis.

4.5 Methods

Sequencing library preparation

Smart-seq2 protocol [65] was used to generate full-length cDNA sequencing libraries from whole organoid mRNA. Briefly, whole organoids were lysed using lysis buffer to render cell lysate containing polyadenylated mRNAs that were reverse transcribed with Superscript III (ThermoFisher Scientific) using an oligoDT primer (/5Me-isodC/AAGCAGTGGTATCAACGCAGAGTACTTTTTTTTTTTTTTTTTTTTTTT TTTTTTTVN) and template switching was performed with a template switch oligo (AAGCAGTGGTATCAACGCAGAGTACATrGrGrG). The oligoDT primer and template switch oligo sequences served as primer sites for downstream cDNA amplification (AAGCAGTGGTATCAACGCAGAGT). cDNA was quantified using a Qubit 3.0 DNA high sensitivity fluorometric assay, and quality was assessed using a bioanalyzer DNA high sensitivity kit (Agilent). Nextera HT transposase (Illumina) was used to convert 1 ng of cDNA into barcoded sequencing libraries.

Transcriptome analysis

Paired-end reads were sequenced at 75x75 bp on an Illumina NextSeq 550, and further depth was sequenced at 50x50 bp on an Illumina NovaSeq 6000 to an average read depth of 65 million paired reads per sample. Samples were demultiplexed using Illumina i5 and i7 barcodes, and higher depth samples were sub-sampled to 100M using SAMtools [44]. Trimmed reads were combined and aligned to the human genome (hg38 UCSC assembly) with STAR alignment [14] (Gencode v37) using the toil-rnaseq pipeline [104]. STAR parameters came from ENCODE's DCC pipeline [13]. Differential gene expression was performed using the DESeq2 [91] package in RStudio. Gene set enrichment analysis was performed using g:Profiler [71].

Immunostaining

Cerebral organoids were collected, fixed in 4% paraformaldehyde (ThermoFisher Scientific #28908), washed with 1X PBS and submerged in a 30% sucrose (Millipore Sigma #S8501) in PBS solution until saturated. Samples were embedded in cryomolds (Sakura - Tissue-Tek Cryomold) containing tissue freezing medium (General Data, TFM-C), frozen and stored at -80°C. Organoids were sectioned with a cryostat (Leica Biosystems #CM3050) at 18 µM onto glass slides. Organoids sections were washed three times for ten minutes in 1X PBS prior to a two-hour incubation in 10% BSA in PBS blocking solution (ThermoFisher Scientific #BP1605-100). The sections were then incubated in primary antibodies diluted in blocking solution overnight at 4deg C. The next day, sections were washed three times with 1X PBS for thirty minutes. They were then incubated in a solution of secondary antibodies diluted in a blocking solution at room temperature for two hours. The sections were washed an additional three times in 1X PBS for thirty minutes.

Primary antibodies used were: rabbit anti SOX2 (ab97959, 1:250 dilution), chicken anti Nestin (ab134017, 1:250 dilution), and DAPI (Sigma D9542-10mg). Secondary antibodies used were: goat anti-rabbit Alexa Fluor 594 (ab150080, 1:250 dilution) and goat anti-chicken Alexa Fluor 488 (ab150169, 1:250 dilution). Imaging was done using the Zeiss Axioimager Z2 Widefield Microscope at the UC Santa Cruz Institute for the Biology of Stem Cells (RRID:SCR_021135) and the Zen Pro software. Images were processed using ImageJ.

4.6 Conclusion

The investigations outlined in Aim 2 represent a significant step towards creating more physiologically relevant cerebral organoid models through metabolic optimization. Our approach combines the technological advantages of the Autoculture platform with a deep dive into the metabolic requirements of developing brain tissue. Key outcomes of this aim include:

- Significant reduction in the expression of genes associated with glycolysis and ER stress in automated cultures
- Effects of feeding frequency on organoid transcriptional profiles and morphology, providing insights into optimal feeding schedules.
- Refined media formulations that better mimic physiological concentrations of key metabolites, particularly glucose, potentially reducing metabolic stress.
- Long-term metabolic profiles of cerebral organoids under optimized conditions, offering a new perspective on the dynamic metabolic needs of these complex 3D cultures.

- Improved protocols for maintaining stable, physiologically relevant concentrations of growth factors and signaling molecules.
- The development of real-time sensing capabilities for key metabolites, enabling dynamic adjustments to culture conditions.

These results not only advance our understanding of cerebral organoid metabolism but also provide practical guidelines for researchers seeking to improve the quality and reproducibility of their organoid cultures. The optimized conditions developed here have the potential to generate organoids with cellular compositions and behaviors more closely resembling those found in the developing human brain.

Furthermore, the integration of advanced sensing technologies, such as in-line pH monitoring and extracellular vesicle analysis, opens new avenues for non-invasive, real-time assessment of organoid health. These tools may prove valuable for quality control in both research and potential future clinical applications of organoid technology.

While further validation and refinement will be necessary, the outcomes of Aim 2 lay a strong foundation for the development of ”stress-reduced” cerebral organoids. These improved models promise to be powerful tools for studying neurodevelopmental processes, modeling neurological disorders, and screening potential therapeutics with greater physiological relevance.

Chapter 5

Integration for Long-term, Feedback-driven Studies

5.1 Introduction

Building upon the development of the Autoculture platform (Aim 1) and the optimization of metabolic conditions for cerebral organoid culture (Aim 2), we now turn our attention to integrating multiple technologies for comprehensive, long-term studies of brain organoids. This multi-system integration represents a significant leap forward in our ability to monitor and analyze organoid development and function in real-time.

Aim 3 focuses on three key objectives:

- Integrating microfluidics, electrophysiology, and imaging into a unified, automated platform

- Implementing computer vision-based feedback for precise control of culture conditions
- Validating the integrated system through a long-term study of cerebral cortex organoids

The challenges addressed in this aim include:

- Coordinating multiple devices and data streams through an Internet of Things (IoT) architecture
- Developing robust feedback mechanisms to maintain stable culture conditions over extended periods
- Capturing and analyzing high-frequency electrophysiological data to reveal dynamic neural activity patterns

By combining these advanced technologies, we aim to create a powerful new tool for studying brain development and function in vitro, with potential applications in disease modeling and drug discovery.

5.2 The Integrated System

We have developed an integrated platform (Figure 5.1) that automates organoid culture and data collection in individual microenvironments. While microfluidics (Figure 5.1A) controls the media environment, digital microscopy captures the morphogenic features. The neural activity is recorded by local field potential measurements using complementary-metal-oxide semiconductor (CMOS) high-density microelectrode arrays (HD-MEA)[52](Figure 5.1B). The IoT cloud network brokers the communication between all devices and facilitates data storage, processing, and presentation services including an interactive webpage (Figure 5.1D). Through touch-free automation, samples remain undisrupted in the incubator, increasing the consistency of images and allowing for higher frequencies of feeding and recording.

At user-defined intervals, conditioned media is aspirated by a syringe pump through a system of distribution valves (Figure 5.1A), stored in a collection reservoir (without passing through the syringe pump vial (Figure 5.1C), and replaced by an equivalent volume of fresh media. Both types of media are perfused through flexible fluorinated ethylene propylene (FEP) tubing at 110 mm/s, which leads to low shear forces [84] (see **??**, Automated fluidics organoid culture).

The digital microscope (Figure 5.2A) is attached using 3D-printed parts on aluminum posts. The 3D printed culture chambers integrate the microfluidics and HD-MEAs. A liquid-impermeable O-ring gasket ensures media retention inside the chamber. The well lid includes a polished glass rod submerged in the media, improving image quality and removing the effects of condensation. Alignment grooves in the glass rod lid prevent rotation and incorrect fitting. The lid exchanges gas with the incubator conditions through ventilating air ducts (Figure 5.2C), similar to a cell culture well plate. The removable and re-attachable lid reduces manufacturing complexity and enables future use of other lids with applications beyond imaging.

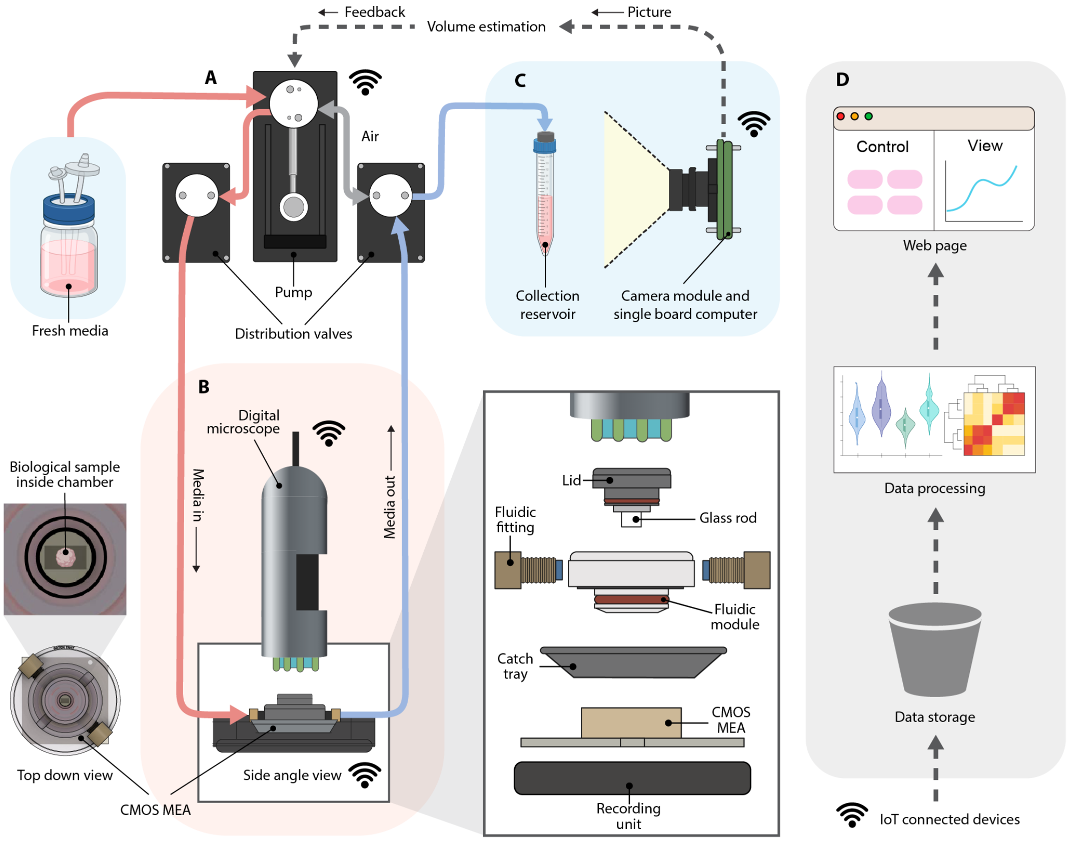

Figure 5.1: Schematic diagram of the integrated feedback platform. (A) A syringe pump and valve system dispense fresh media and aspirate conditioned media at user-defined intervals. The blue background represents 4°C refrigeration. **(B)** In-incubator microscopy and HD-MEA electrophysiology unit for automatic recording, media exchange, collecting morphogenic and functional dynamics data of the biological sample. Exploded view: the 3D printed gasket-sealed culture chamber. The red background represents 37°C incubation. The microfluidic culture chamber has an access lid with a polished glass rod viewing port, a gasket-sealed microfluidic module with threaded microtube fluidic fittings, and an overflow catch tray. The microfluidic culture chamber attaches to the HD-MEA, which houses the sensor for recording electrophysiology signals. **(C)** An in-refrigerator camera setup captures images of the aspirated conditioned media drawn from each culture and relays them through cloud-based data processing for volume estimation feedback to the syringe pump system. **(D)** Devices communicate over MQTT (Message Queuing Telemetry Transport) protocol and automatically upload data to the cloud, where it is stored, processed, and presented on a web page.

Figure 5.2C shows the cross-section of the culture chamber attached to the HD-MEA. The media flows in (red) and out (blue). The sinuous media path and well geometry ensure minimum disturbance to the biological sample [84]. Fresh media is delivered on top of the volume present in the chamber, similar to partial media changes found in manual feeding protocols [12, 109]. The ideal operating range is between 350 to 700 µL (see **??**, Figure C.2 and Table C.1 for numerical volume limits). In the case of over-aspiration, media drops to a minimum of 170 µL before aspirating air from the chamber's headspace. The 3D-printed catch tray guards against overflow, collecting up to 1.5ml (200% of the chamber's capacity) to protect the recording equipment from liquid damage.

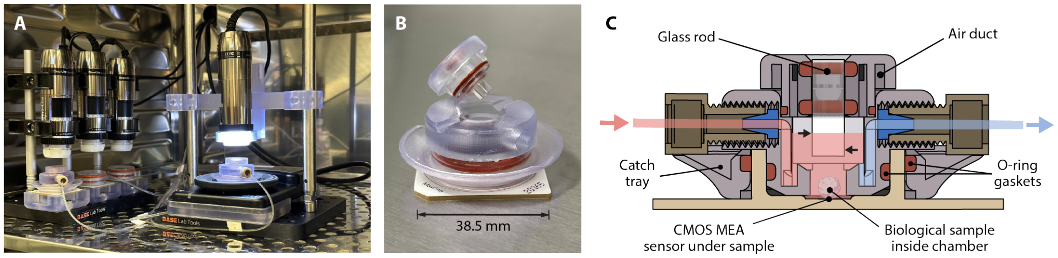

Figure 5.2: The microfluidic culture chamber. **(A)** The experimental setup inside an incubator shows two microfluidic culture chambers and two conventional membrane lids. **(B)** 3D printed culture chamber attached to the HD-MEA. **(C)** Cross-section showing the fluid path. Fresh media (red) enters the chamber, filling the internal cavity. Conditioned media (blue) is drawn out of the chamber. The media level, noted by the upper black arrow (559 µL) and lower black arrow (354 µL) on the glass rod, is the ideal operating range that keeps the rod immersed in media. The biological sample is adhered to the HD-MEA in the bottom of the cavity.

5.3 Microfluidic feedback with computer vision

We developed a computer vision volume estimation system to monitor the accumulation of aspirated media and identify anomalies during culture feeding events. Figures 5.3A and 5.3B provide a detailed view of the setup inside a refrigerator, which includes three main components: a collection reservoir support system, an LED panel, and a camera module (see **??**, Assembled devices and custom 3D-printed components). The camera module remains on standby for image capture requests made by other IoT devices or users. Upon request, computer vision techniques are employed to estimate the media volume within the reservoirs accurately.

Figure 5.3C shows the computer vision process (see **??**, Computer vision for fluid volume estimation) for segmenting area related to the media in the reservoir. A calibration was required to establish the relationship between the segmented area in pixels and volume in milliliters. We captured 184 images of the collection reservoirs containing volumes of media ranging from 0 to 12 mL (several pictures for each volume), with each volume confirmed by a scale, accurate to 1 µL. For each specific volume in Figure 5.3D, multiple points overlap and are all accounted for to calculate the polynomial regression lines. To accommodate the reservoir's conical section (volumes <1.5 mL) and cylindrical section (volumes >1.5 mL), two distinct regressions were applied, ensuring a high degree of precision for each geometrical shape.

A Leave-One-Out cross-validation (LOO) [55] approach was employed to quantify the model's error. This method tests the model's accuracy and generalizability in an unbiased manner, ensuring that the calibration results in a model that performs reliably across different samples. The effectiveness of the model is assessed quantitatively with the following metrics: an average Mean Absolute Error (MAE) of 0.56% (equivalent to 27 µL), an average standard deviation of errors at 0.53% (22 µL), and an average Root Mean Square Error (RMSE) of 0.77% (35 µL). The polynomial models exhibit R-squared values of >0.99, denoting an optimal fit of pixel area to liquid volume. Figure 5.3E shows the average absolute error percentage at a specific volume, with the bar indicating the error range from minimum to maximum.

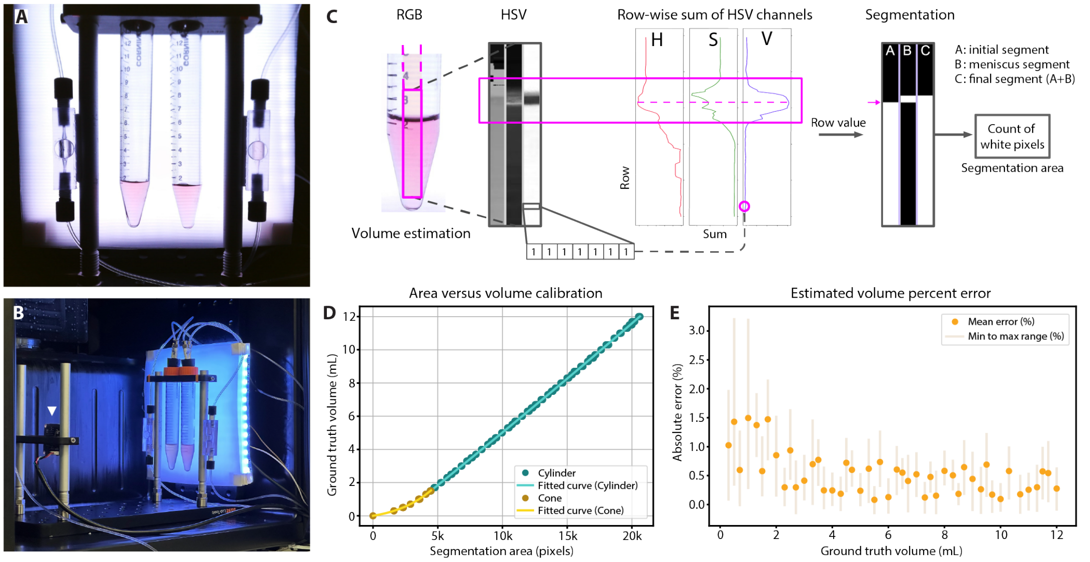

Figure 5.3: Computer vision for volume estimation. **(A)** Example of a raw image captured by the camera module. **(B)** In-refrigerator volume estimation setup. The CMOS camera module (the white triangle) images the conical tubes with a diffused LED backlight for even illumination. **(C)** Fluid segmentation: a rectangular pixel patch down the center of the conical tube; Row-wise summations of the HSV channels are used to detect the location of the meniscus. The initial liquid potion segmentation is added to the meniscus portion to yield the final segmentation. **(D)** Calibration graph with a fitted relationship of segmented pixel count to ground truth volume. **(E)** The absolute error percentage: orange dots represent the average error at selected volumes. The shaded bar represents the minimum to maximum error range.

5.4 Automated study of cerebral cortex organoids

The integrated research platform was used to study the effects of automation on the neuronal activity of pluripotent stem-cell-derived mouse cerebral cortex organoids. Embryonic stem cells were aggregated, patterned, and expanded to generate organoids using a previously defined differentiation protocol [18, 57]. Day 32 post-aggregation, 10 organoids were plated two-per-chip directly onto five HD-MEAs. For the 7-day study, the five chips were split into groups that were fed and recorded with standard manual procedures (Controls 1-3), automatic feeding and manual recording (AF), or automatic feeding and automatic recording (AFAR). Four chips (Controls 1-2, AF, and AFAR) were imaged in the incubator every hour, by their dedicated upright digital microscope (DinoLite).

Automated microfluidic feeds were used to increase the consistency and frequency of cell culture media replacement. We removed conditioned cell supernatant from the well and dispensed the equivalent volume of fresh media for each feed cycle. The controls had 1.0 mL media replacement every 48 hours, consistent with standard protocols. AF and AFAR were placed on a protocol in which 143 µL media were replaced every 6 hours, matching the total media volume turnover across groups for the 7-day study. The schedule of automated media feeds was defined at the experiment's launch and initiated by a timed feeding job command sent to the microfluidic pump. The fidelity of feeding was controlled through a computer vision volumetric feedback loop on the aspirated conditioned media (Figure 5.3, 5.4A).

Conditioned media has a high protein content, contains cellular debris, and is susceptible to forming salt crystals [9, 47]. In microfluidic systems, this leads to clogs, error accumulation, and failure modes [42]. To overcome this, a volume estimation feedback loop was initiated each time the pump performed a job. Once media was perfused to/from a specific well, the pump sent a job request to the camera module responsible for imaging the well's collection reservoir. The image was captured, uploaded to the cloud, its volume estimated by the computer vision Estimator, and returned to the pump for feedback interpretation. Within tolerance, the action was declared a success (marked as a green check mark in Figure 5.4A), and no further action was taken. Outside of tolerance, the pump scheduled itself a new job proportional to the volume discrepancy and in relation to the number of previous feedback attempts (see **??**, Feedback interpreter).

The system strives to resolve discrepancies on its own using feedback. However, in extreme cases where volume estimation returns a value outside of reason (i.e., $>$ expectation + 2 mL) or if the feedback iteration limit is reached (i.e., $>$ 20 attempts), the system was programmed to send an alert to a Slack messaging channel and pause. During the 7-day experiment, the system resolved errors independently, and this condition was not reached.

The automated feeding and feedback results for AF and AFAR are visually represented in Figure 5.4B-D. Figure 5.4C shows the traces of expected volume and computer vision estimated volume for AFAR (left) and AF (right) for the 7-day study (Days 5 to 12 post-plating). There was a collection reservoir change on Day 8 in which the 15 mL conical was replaced with a fresh tube. In both samples, the drop in estimated and expectation reflects the collection reservoir exchange. For AFAR (Figure 5.4B, left), a zoomed-in view of the feedback loop following the scheduled feeding cycle at 7:12 on Day 9 highlights feedback actions taken to remedy a volumetric discrepancy. In this instance, the volume estimation was less than expected after the feed cycle. Five consecutive aspiration jobs were carried out, and the estimated volume still remained under expectation. At the 6th iteration of feedback, a pull job was sent to the pumps, which raised the collection volume above the expected volume. In the 7th and 8th iterations of feedback, two dispense jobs were engaged to supplement the well for the over-aspiration. In a similar case, for AF (Figure 5.4B, right), a total of 6 iterations of feedback were engaged to bring the estimated volume into tolerance with the expected volume; however, in this example, no dispense jobs were required. Figure 5.4D shows histograms of the sum of pump events per day by subcategory. Each feeding cycle (four per day) was scheduled, and all other events occurred through feedback.

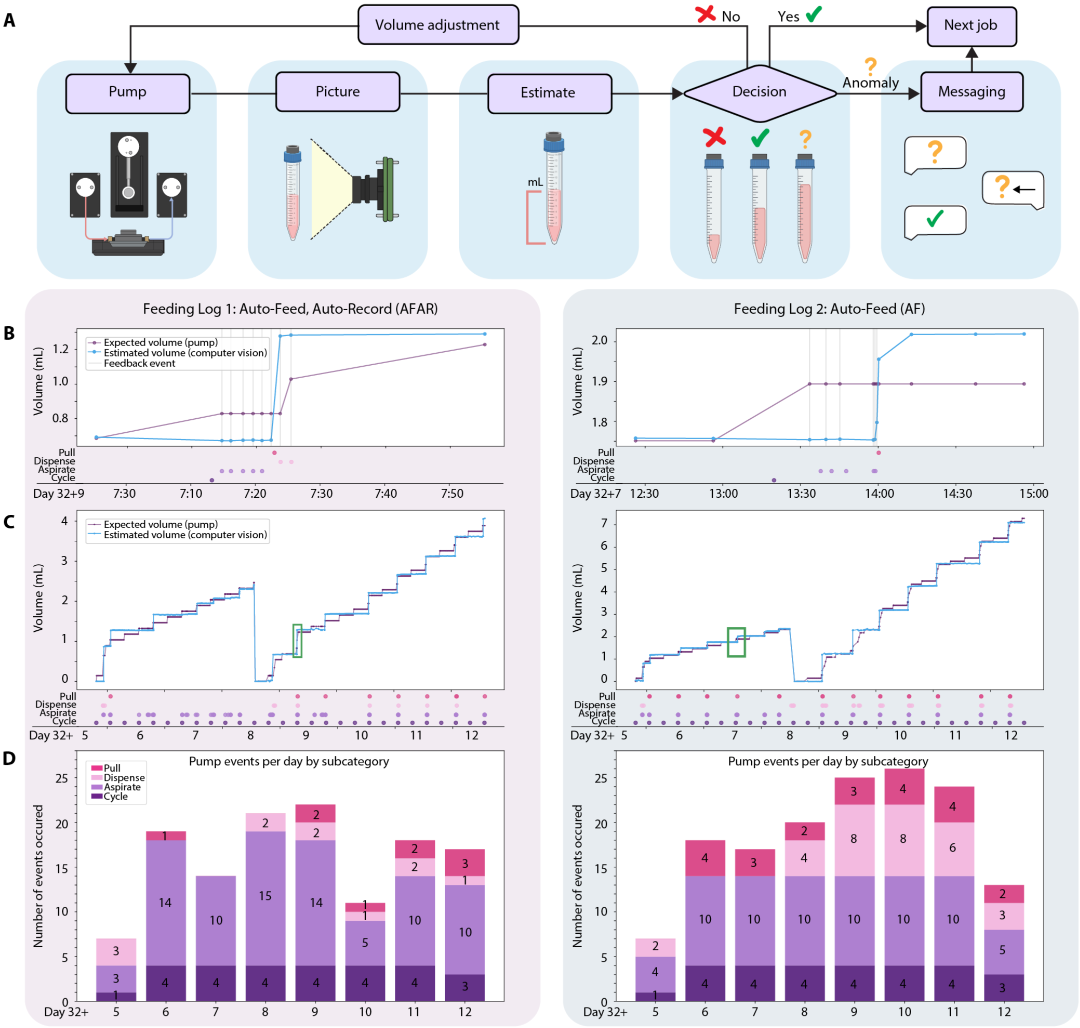

Figure 5.4: Volume feedback. **(A)** Volume estimation feedback loop. After the pump completes a microfluidic action, it requests a picture of the media collection reservoir from the camera module. The picture is passed to the cloud-based computer vision program to estimate the current volume. The results is compared with the expected volume, and a decision is made: within tolerance (green checkmark), a microfluidic volume adjustment action is needed (red "x"), or an anomaly is detected (yellow question mark). Once the estimated volume is within tolerance (green check mark), the feedback cycle ends and proceeds to the next job. If this cannot be achieved or an anomaly is detected, such as out-of-range volumes, an alert is sent to the user messaging service to request assistance. (B-D) On these graphs, the "Day" x-axis summarizes the timeline: organoids were plated on the HD-MEA on Day 32, automation started 5 days after plating and continued to day 12. Above this axis, dots mark the occurrence of microfluidic events. **(B)** Graphs of the Expected Volume and Estimated Volume for the automated AFAR (left) and AF (right) during a period of feedback events. Event types are marked with dots below the graph. **(C)** The complete view of Expected and Estimated volume traces over the 7-day study. **(D)** Stacked histogram pump events per day organized by type.

5.4.1 High-frequency HD-MEA recordings do not disrupt neuronal activity

To interrogate organoid neuronal activity, extracellular field potentials were measured using 26,400 electrode HD-MEAs, which can record up to 1,020 electrodes simultaneously. We conducted daily activity scans to monitor neural activity. Heat maps derived from the first and final activity scans for each sample are presented in Figure 5.5B, with organoid body outlines for reference. To optimize electrode coverage, we generated specific configuration files for electrode selection based on the regions with the highest activity, which remained constant for four of the five chips. In one case (AF, Day 32+6), we adapted the configuration due to the emergence of a new high-signal area on the second day of recording. These maps allowed continuous electrode measurements for 10-minute intervals optimized for frequent, long-term sampling.

Manual recordings involved an experimenter placing each HD-MEA on the recording unit and initiating 10-minute recordings via software. In contrast, the hourly recordings (AFAR) featured the HD-MEA remaining on the headstage while automated software handled the entire process, from power management to data uploading. AFAR amassed 161 recordings, totaling 26.8 hours (560 GB) of electrophysiology data. Conversely, all manually recorded samples (Controls 1-3 and AF) accumulated 7 recordings, amounting to 1.2 hours of electrophysiology data.

From these data, we analyzed the effects of our automated microfluidic, imaging, and recording system on the neuronal activity of the brain organoids housed therein.

Imaging of the chips from above (Figure 5.5A) allowed us to align the body of the organoid with neural units detected (Figure 5.5B). In some instances, such as in Control 1, neurite outgrowths were evident in the images and activity scans.

The initial activity scan was used to assign samples for the experiment. In the first activity scan, AFAR and Control 1 exhibited the highest activity, followed by AF, Control 2, and lastly, Control 3. This specific categorization of samples was designed to address potential biases introduced by varying levels of starting activity. To ensure robust analysis, each chip was treated as an average of the two organoids. Chips demonstrated similar trajectories in the number of units and firing rate frequency over the 7-day experiment, irrespective of feeding or recording schedules (Figure 5.5C-D). Figure 5.5C shows the distribution of neuronal firing rates as a violin plot for each chip over seven days, labeled with the number of neurons detected in that recording. The number of detected units had a positive correlation over the 7-day study for all samples except Control 1, which also presented the highest number of units (Figure 5.5D, top). Similarly, the median firing rate was positively correlated with time for all samples except for Control 2 (Fig 5.5D, bottom). The fully integrated system, encompassing automated feeding, imaging, and recording, behaved like the controls, indicating minimal bias or distortion of data as a result of increased HD-MEA recording frequency.

5.4.2 High-frequency HD-MEA recordings reveal dynamic neuronal activity states in organoids

The hourly recording condition (AFAR) unveiled dynamic and transient states, not apparent with single daily recordings (Figure 5.5E). While the trendlines for hourly and daily recordings (for both units and firing rates) have similar upward trends, hourly recordings show more prominent oscillations around the trendline not captured by the single daily recordings. Median firing rates fluctuated as much as 3-fold over the course of a day, sometimes within a few hours of each other.

To determine if feeding cycles influenced this activity, we aligned recordings to a six-hour ‘time since feed’ cycle (Figure 5.5F, top) and examined potential differences in the number of units and firing frequency. Figure 5.5F presents the composite graph of aggregated neuronal firing rates comprising 26 feeding cycles with all 161 recordings binned with respect to their time since feeding. Our results showed no trend across all superimposed feeding cycles: neither the number of units nor firing rate changed in relation to feeding cycles. The oscillations presented in Figure 5.5E do not align with feeding and appear to be a temporal dynamic intrinsic to the network. In summary, these findings underscore the robustness and reliability of our feedback-driven microfluidic platform for brain organoid studies.

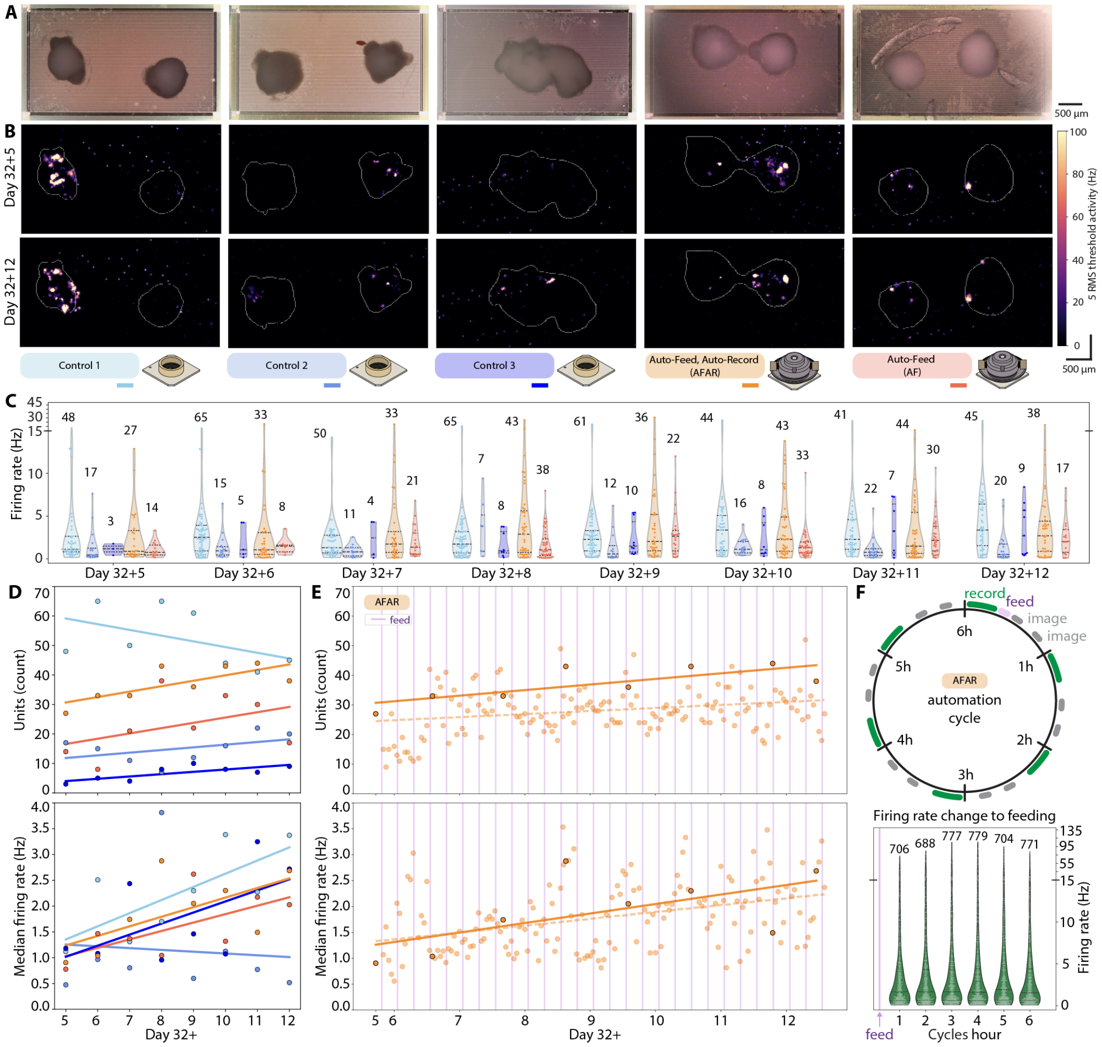

Figure 5.5: Electrophysiology analysis of the 7-day cerebral cortex organoid study. **(A)** Digital microscope images of each organoid sample **(B)** Boundaries of each organoid were outlined and overlaid for orientation on their activity scans from the first recording day (top) and last recording day (bottom). The samples are labeled underneath, with the color legend consistent throughout the figure. **(C)** Spike sorting analysis on 10-minute recording/day detected neural units and spiking frequency. Daily Violin plots. The black dashed lines represent the first (lowest) quartile, median, and third (highest) quartile. The firing rate of each neuron is represented along the y-axis, and the total number of neural units is labeled above each plot. **(D)** Plots of the number of units (top) detected on the daily activity scans, and their median firing rates (bottom). **(E)** The AFAR had an additional 23 (hourly) recordings per day (translucent dots/trendline) beyond the daily recordings (opaque dots/trendline). The trend of units detected over time (top graph) and median firing rates (bottom graph) was different with the inclusion of hourly recordings compared to daily recordings. Vertical lavender lines represent occurrences of automated feeds. **(F)** A dial schematic of the 6-hour automated cycle of recording, feeding, and imaging for the AFAR sample (top). The AFAR's hourly recordings were organized in bins of 'hours since feed,' and the neuron firing rates are shown in violin plots (bottom).

5.5 Methods

Automated fluidics organoid culture

The automated microfluidic pump system builds on previous work [84]. The microfluidic system was configured to support two chips (AF and AFAR) and their respective collection reservoirs (right and left) were imaged by the camera setup.

Fresh cell culture media is kept at 4°C refrigeration and accessed by the pump through flexible FEP tubing routed into a benchtop refrigerator and to a media bottled with a reagent delivery cap (Cole-Parmer VapLock). Fresh media is kept refrigerated to increase longevity and may be replaced during experimentation. To dispense, the syringe pump and distribution valves draw fresh media into the syringe vial and distribute the programmed volume into flexible FEP tubing routed through an access port in the incubator. Here, the media is heated in incubator conditions prior to being delivered to the organoid inside the culture chamber. To keep media dispenses available on demand, a preheated 450 µL reserve (59% of the chamber's volumetric capacity) of fresh media remains idle in the FEP tubing so that upon dispensing, 37°C media is delivered to the well in less than 10 seconds. The FEP tubing is interfaced with the fluidic module with threaded ferrule lock and nut fittings (Cole-Parmer VapLock). Outflow from the fluidic module is drawn away with FEP tubing routed out of the incubator and into a refrigerator containing the collection reservoirs and computer vision camera setup.

For the collection reservoirs, we selected 15 mL Polyethylene Terephthalate (PET) conical tubes (430055, Corning) for high optical clarity, ease of replacement, and durability in downstream analysis and cold storage. To enhance visibility for computer vision imaging, we removed the factory-printed writing area on the conical PET tubes using generic, multipurpose tape. Flexible FEP tubing was interfaced with the PET tubes using a rubber cork plug (#6448K95, McMaster-Carr). The cork was pierced with 8-gauge steel needles that served as supportive conduits for the tubing. The tubing was secured inside the needle with glue (Loctite 4011) to create a hermetic seal at the point of interface. The steel encasing of the needles ensures a smooth, unobstructed flow within the flexible FEP tubes. Each collection reservoir had two flexible FEP tubes: one for media coming from the fluidic module and one for pressurized operation connected to the syringe pump. This ensured that spent media never entered the syringe (only air). The air is expelled into a filtered (Millipore AA 0.22 µm syringe filter) safety container (not shown in Figure 5.1).

For the 7-day study described here, we designed for equivalent media exchange across conditions. The Controls 1-3 were fed 4 times at 1 mL per feed, totaling 4 mL of replacement media. AF and AFAR were fed 28 times at 143 µL per feed, totaling 4 mL of replacement media over the week. Summing the scheduled feeds and feedback adjustments, a single collection reservoir could store conditioned media for 2-3 weeks.

Sterilization and assembly

Before use in tissue culture, components were placed in autoclavable bags (RIT-3565, PlastCare USA) and steam-sterilized at 134°C for 20 minutes or 121°C for 30 minutes based on Formlabs material datasheet specifications. Components were autoclaved, disassembled, and then assembled in a sterile tissue culture hood to avoid deformation or cracking during temperature cycling. Components were transported in an enclosed petri dish (small items) or a sterile autoclaved bag (large items) before being released into the incubator. Components that could not be autoclaved (such as electronics, i.e., recording headstage, microscope) have their enclosures sterilized with hydrogen peroxide disinfecting wipes (100850922, Diversey) before entering the incubator.

Priming the experiment

On the 5th day on chip (Day 32+5), membrane lids for two HD-MEAs (AF and AFAR) were replaced with microfluidic culture chambers. During the replacement process, all media was aspirated from the HD-MEA's well with a P-1000 pipette. The microfluidic catch tray, followed by the culture chamber, was inserted inside the well, and 750 µL of the original media was added back to the microfluidic culture chamber. Excess media was discarded. The glass rod lid was placed on top.

Flexible FEP tubes (idling with DI water) were flushed with 1.0 mL of fresh media. After priming the lines with media, the AF/AFAR chips were connected with fluidic fittings wrapped with Teflon tape. An initial aspiration leveled the media to the target fluidic operating range. The collection reservoirs were replaced with new empty conical tubes.

Running the experiment

During the experiment, the media was exchanged using a feed cycle operation consisting of an aspiration followed by fresh media dispense. Here, we performed 143 µL aspirations and dispenses every 6 hours to match 1.0mL feeds every two days in the manual feeding controls. Feedback performed additional aspiration, dispense, and pull actions in addition to the basic feed cycle schedule to ensure the system stayed within normative error ranges. See section Feedback interpreter.

Teardown of the experiment

Once the experiment was stopped, chips were disconnected from the flexible FEP tubes by unscrewing the fittings. The flexible FEP tubes with fittings were sterilized in a flask containing disinfectant (Cydex) and covered with aluminum foil. The collection reservoirs with the experiment's conditioned media were disconnected and taken for analysis. New collection reservoirs were inserted for the cleaning cycle. The pump ran a cleaning solution (Cydex) through the entire internal cavity for 1 hour to disinfect the system. Following disinfection, DI water and dry, sterile air were profused through the system for 12+ hours (overnight) to clear the disinfectant. The flexible FEP tubes were left resting with DI water until the next experiment.

Microfluidic culture chamber

The microfluidic culture chamber assembly allows media to be exchanged inside the HD-MEA well. The chamber assembly consists of a microfluidic module, glass rod lid, and catch tray (Figure 5.2B, C).

The microfluidic module is placed inside the HD-MEA well, creating a media chamber and fluid path into and out of the chamber. Media from outside the incubator travels to the fluidic insert along 0.030" ID and 0.090" OD Tygon tubing (AAD02119-CP, Cole Parmer); the length of the tubing is approximately 100 cm. The tubing attaches to the fluidic insert using PEEK fittings (EW-02014-97, Cole Parmer) wrapped (counter-clockwise) in PTFE thread seal tape around twice the fitting's circumference. The inlet and outlet are raised inside the fluidic insert to create a pool following a geometry published in previous work [84].

The fluidic insert, glass rod lid, and catch tray use silicone O-rings (5233T543, 5233T479, 5233T297, and 5233T585, McMaster) to provide seals against contaminations and leakage. O-rings were rubbed with a minimal quantity of canola oil for lubrication to facilitate installation and enhance sealing performance. The canola oil can be autoclave-sterilized, but it is unnecessary if the O-rings are sterilized post-lubrication (see Sterilization and assembly).

Computer vision for fluid volume estimation

The computer vision setup, located inside a 4°C refrigerator, included a support for the collection reservoir, a camera module, and an LED panel positioned behind the conical tubes. The LED panel served as backlighting to enhance the clarity and contrast of the images. The reservoir support was a two-plex 3D-printed system capable of multiplexity to tailor alternate experiments (see Assembled devices and custom 3D-printed components). The camera and LED panel were both controlled by a Raspberry Pi.

To generate the calibration dataset, the camera module captured images of media in the collection reservoirs at select volumes over the entire range of the tube (0-12 mL), totaling 184 images. The volumes associated with each image were measured using a high-precision scale (30029077, Mettler Toledo). This approach enabled a correlation between the visual representation of media in the images and its actual volume (see **??**).

To ensure image quality, our study introduced two checks to validate the integrity of the captured images: Lighting and blurriness. A region of interest (ROI) was designated within the panel's area to verify the lighting conditions by checking that the average RGB color values each exceeded a minimum threshold of 20 out of 255. Blurriness was assessed by computing the variance of the Laplacian for the image, with a necessary threshold of 50 to pass. The thresholds were empirically determined using the calibration dataset.

Figure 5.3C illustrates the methodology applied to fluid segmentation, outlined in the Results section. The process begins with capturing an RGB image of the collection reservoirs that are fixed in place by the setup. To facilitate better segmentation and feature extraction, the RGB image is transformed into the HSV (Hue, Saturation, and Value) color space. A summation of the HSV values row-wise from the bottom to the top of the collection reservoir results in three distinctive profiles that allow differentiation between the liquid and background. Each profile, as illustrated in Figure 5.3C, presents a vertex at the boundary. A row value was established by averaging three rows identified in each HSV channel: an abrupt rise in the curve for the Hue channel, the absolute maximum for the Saturation channel, and the absolute minimum for the Value channel. From the average row value, the first segmentation was created. Everything below this row was set as white pixels, and everything above it was set as black pixels. A local evaluation around the average row was made to incorporate the meniscus in this segmentation. Utilizing HSV thresholds, the meniscus was accurately characterized and incorporated into the initial segmentation, culminating in the final image segmentation, in which white pixels represented the liquid portion.

The estimated volume was given by Equation 5.1, where x represents the segmented area in pixels, and the resultant volume is in microliters. Two different curves are used to account for the conical section for volumes under 1.5 mL (and pixel area less than 4446) and the cylindrical section for larger volumes.

$$V(x) = \begin{cases} 5.09 \times 10^{-9}x^3 + 2.39 \times 10^{-5}x^2 + 0.13x - 1.28 & \text{if } x < 4446 \text{ pixels} \\ 2.60 \times 10^{-11}x^3 + 5.38 \times 10^{-7}x^2 + 0.62x - 1288.37 & x \geq 4446 \text{ pixels} \end{cases} \tag{5.1}$$

The image segmentation and estimation based on the mathematical model (Equation 5.1) is carried out by a software program named the “Estimator.” The process initiates with a feeding cycle, which triggers a picture request. Upon receiving the image of the collection reservoir, the “Estimator” analyzes the image and returns the estimated value of the fluid volume. The volume is relayed to the next module for feedback interpretation within the pump system (see Feedback interpreter).

Feedback interpreter

Computer vision volume estimations were compared to expectation values based on the sum total of pump action jobs. The feedback interpreter classified estimations into four categories: within tolerance, out-of-tolerance, anomaly, and tube change. Tolerance was a static volume selected at the start of the experiment. For the results shown here, the tolerance was 143 µL. If the volume estimation received was within the expectation value +/- the tolerance, the pump action was determined a success, and feedback ceased. If the volume estimation received was beyond the expectation value +/- the tolerance and also less than +/- 2000 µL, another cycle of feedback was engaged. When the volume was less than expected, for the first 5 iterations of feedback, aspiration jobs were sent to the pump with the difference of expectation and estimation. For iterations 6 to 19, pull jobs were sent to the pump, increasing by one for each subsequent interaction. A "pull" is a 1000 µL aspiration at 10x the standard syringe speed (applying a 1.1 x 103 mm/s flow rate), shown to generate the force required to break through variably high resistance in the conditioned media. At 20 iterations, the feedback interpreter requests manual intervention via the messaging application, and all further pump actions are suspended until the issue is resolved. When the volume was more than expected, dispense jobs were sent to the pump with the difference of expectation and estimation. Dispense actions were limited to 200 µL per action and 2 iterations of feedback in total to prevent overflow. A volume estimation that was 2000 µL or more above the expectation value was determined as an anomaly and requested manual intervention via the messaging application, and all further pump actions were suspended until the issue was resolved. The feedback interpreter automatically detected collection reservoir tube changes when the volume estimation dropped by 2000 µL or more compared to the previous estimation and the total volume present was estimated as less than 2000 µL.

Computer vision for In-incubator Organoid Culture imaging

In-incubator imaging

A 5MP digital microscope (AM7115MZTL, Dino-Lite) was placed over the organoid culture on the HD-MEA using holders described in Assembled devices and custom 3D printed components. Imaging was performed from the top through a glass rod (quartz drawn rod, 5mm ± 0.20mm dia x 15mm ± 0.20mm long, UQG Optics) (in AF/AFAR chips) or through a membrane lid (in control chips). The image is captured using reflected light from a built-in brightfield LED source next to the camera sensor. The 3D printed alignment trays handle most of the chip placement, with initial minor focal plane adjustment required. The microscope remains shut off until the software triggers it to turn on the lights and take a photo.

Image Segmentation for Organoid

In the process of image segmentation for organoid analysis, the first step involves applying an image calibration to correct any distortion. This procedure requires identifying four source points and four destination points. The former were manually selected from the distorted image. The latter were calculated based on an initial pixel (left corner of the HD-MEA), the size of the electrodes, and the spacing between them, both in millimeter units. This relationship between pixels and millimeters was established by using known dimensions of the HD-MEA border and electrode pitch in the image.

The organoid segmentation within the rectified image was accomplished using the Segment Anything Model (SAM) [36]. This model combines neural network architectures, allowing for precise and versatile image segmentation without requiring specialized training on new images. The segmented image is analyzed to detect variations in pixel intensity, which signify the presence of organoid contours. Both images with the organoid's contour and electrode grid are overlayed. Each electrode area is checked for the presence of the organoid's border. When a border is detected within an electrode's bounds, that particular electrode is marked prominently on the grid image to signify contact with the organoid (see Figure 5.5B). The step-by-step illustration of the analysis process is shown in Supplemental Figure C.5.

Plotting & alignment to neural activity data

Electrode numbers as (x,y) position were plotted in matplotlib and exported as SVG. The SVG aligns over other plots, such as activity heatmaps, which follow the same x:3580 by y:2100 axis dimensions. Since electrophysiology plots use the electrode coordinate system with the same (x,y) positions, the image segmentation grid and neural activity plots are aligned on the same coordinate system.

Measuring neural activity

Extracellular field potential recordings were performed using CMOS-based high-density microelectrode arrays (HD-MEAs) (MaxOne, Maxwell Biosystems). Each HD-MEA contains 26,400 recording electrodes within a sensing area of 3.85 mm × 2.1 mm (each electrode has a diameter of 7.5 µm, spaced 17.5 µm apart center-to-center). A subset of up to 1020 electrodes (defined spatially by a configuration) can be selected for simultaneous recording [3]. Across one configuration, neuronal activity in microvolts was sampled over time at 20kHz and stored in HDF5 file format.

The experiment involved each chip's daily activity scans and recordings (described below). Each chip underwent an activity scan and subsequent recording every day, consistently conducted within the same one-hour time window. All chips shared the same recording unit and were recorded one at a time. For the AFAR condition, beyond the daily recordings and activity scans, the chip remained on the HD-MEA for automated hourly recordings.

The gain was set to 1024x with a 1 Hz high pass filter for both activity scans and recordings. The recording was set up to save 5 RMS thresholded spike times as well as all raw voltage data for downstream analysis and plotting.

All neural activity measurements were performed inside the incubator at 36.5°C, 5% CO2.

Activity scans

Activity scans were performed daily in the MaxLab Live Scope (Version 22.2.22, MaxWell Biosystems) to identify where the organoid's electrical activity is spatially distributed across the HD-MEA. The activity scan sequentially records from different configurations of up to 1020 electrodes, thereby sampling the microelectrode array for action potentials. We used the checkerboard assay consisting of 14 configurations, with 30 seconds of recording per configuration. The resulting activity heatmap (see Activity heatmaps) for each chip is shown in Figure 5.5B and Supplementary Figure C.6. Based on the assay results, 1020 most active electrodes were selected for simultaneous activity recordings.

Recordings

Each recording lasted 10 minutes. Initial recording configurations were created on the first day, and configurations were updated on the second day to match shifting activity. Afterward, we chose to keep the configurations constant across the final 5 days since the activity did not shift dramatically, and keeping the same configuration allowed for more consistent monitoring of the same region.

Spike sorting and curation

To know how automated culture affects the neuron's electrophysiology, each MaxWell recording is spike sorted into single unit activity using Kilosort2 [56]. By using a template-matching algorithm, Kilosort2 can cluster neurons based on their waveform shape. The settings for spike sorting are a bandpass filter of 300 to 6000 Hz for the raw data and voltage thresholding with 6 RMS above the baseline.

The sorting output is curated by an automatic algorithm that checks the signal-to-noise ratio (SNR), firing rate, interspike interval (ISI) violation, and the spike footprint for each putative neuronal unit. As a result, units that had SNR above 5, firing rate above 0.1 Hz, ISI violation below 0.1 and footprint on more than one channel are kept for analysis. Spike sorting was performed on the National Research Platform (NRP) computing cluster with an NVIDIA GeForce GTX 1080 Ti GPU.

Activity heatmaps

Activity heatmaps in Figure 5.5A depict the spatial distribution of significant voltage events. MaxWell software provides thresholded event identification based on moving root-mean-square (rms) value for each electrode, identifying events exceeding 5 times an electrode's rms value. We created a 2D grid of spike counts per second and applied a 2D Gaussian blur for visual smoothness, normalizing each grid point by dividing it by $2\pi r^2$ to re-scale back to the original Hz values. These values were then plotted as the activity heat maps. The heatmaps use warmer colors for higher firing frequency and darker colors for lower activity.

5.6 Conclusion

The multi-system integration achieved in Aim 3 represents a significant advancement in cerebral organoid research technology. Our integrated platform, combining automated microfluidics, high-density microelectrode arrays, and in-incubator imaging, enables unprecedented long-term monitoring and control of organoid cultures.

Key achievements of this aim include:

- Successful integration of multiple technologies through an IoT architecture, allowing for coordinated, automated experiments
- Development of a computer vision-based feedback system for precise control of media exchange, ensuring stable culture conditions
- Demonstration of the platform's capability to support long-term organoid culture with minimal human intervention
- Acquisition of hourly electrophysiological data, revealing dynamic neural activity patterns not observable with traditional recording methods
- Validation of the system's performance through a 7-day study of mouse cerebral cortex organoids, showing comparable growth and activity to manual culture methods

Importantly, our results indicate that frequent automated feeding and recording do not negatively impact organoid development or neuronal activity. Instead, the high-frequency recordings unveiled temporal dynamics in neural firing patterns that were not apparent in daily recordings.

This integrated platform opens new avenues for studying brain development and function in vitro. The ability to maintain stable, long-term cultures while continuously monitoring multiple parameters will enable more complex experiments, such as extended developmental studies or chronic drug treatments. Furthermore, the high-temporal resolution data acquired through this system may provide new insights into the emergence and maturation of neural networks in cerebral organoids.

Future work will focus on extending the duration of automated experiments, incorporating additional sensing modalities, and applying this technology to human cerebral organoids and disease models. The modular nature of our IoT-based system will facilitate the integration of new technologies as they become available, ensuring that this platform remains at the forefront of organoid research.

In conclusion, the multi-system integration achieved in Aim 3 provides a powerful new tool for neuroscience research, combining the benefits of automation, precise environmental control, and high-resolution data acquisition. This platform has the potential to accelerate our understanding of brain development and function, and may ultimately contribute to the development of new therapies for neurological disorders.

Chapter 6

Conclusion

6.1 Discussion

The increasing demands for long-term experiments, reproducibility, parallelization, and longitudinal analysis drive cell culture toward automation. This study showcases an automated, microfluidic solution for the growth and maintenance of organoids capable of existing in conjunction with other control and sensing devices over the Internet of Things, magnifying the ability to capitalize on precision robotics for automated experimentation. Combining this platform with the imaging platform shown here (Figure 3.7) provides a stationary environment that uniquely enables the live study of individual organoids over time. This platform could easily be used to maintain other organoid models and *ex vivo* tissues. The 24-plex microfluidic chip described here could also be adapted to support the growth of adherent (2D) cultures by including an additional protocol step to treat the microfluidic chip with a cell adherence surface coating prior to loading cells.

The use of orbital shakers for long-term organoid culture has been widely adopted in the field and yields benefits to nutrient diffusion and dissolved gas homogeneity. However, the fluid velocities and shear forces present do not resemble the embryonic environment. Microfluidics such as in the system shown here could be used to tune fluid velocities, shear forces, and pressure gradients while providing the same benefits to nutrient and dissolved gas concentration through rapid feeding regimens. Our system enables an environment of low velocities. The CFD simulation shown here (Figure 3.6) represents the conditions present in the validation experiment which preferentially selected for low velocities; however, greater rates of profusion would yield higher velocity gradients that could be used to study the effects on organoid morphology and differentiation.

Reducing stress levels in cerebral organoid models is crucial to achieving physiological relevance. As measured by reduced glycolytic enzyme expression, the environment of the *Autoculture* platform results in reduced-stress organoids compared to traditional suspension culture conditions. Pathways that respond to environmental conditions such as sugar metabolism, hypoxia monitoring, and protein production are interconnected through the integrated stress response pathway. By reducing concentration fluctuations in the cell culture media through automated feeding, the cultures may experience greater homeostasis. Further investigation is needed to understand the potential long-term effects of reducing gene expression of glycolysis and ER stress genes and the critical environmental conditions that underlie the gene expression signature associated with less cell stress we observed. For example, it is unclear whether depletion of essential nutrients, like glucose, or accumulation of cell metabolites, like lactose, is the critical factor leading to the induction of genes in the glycolysis pathway observed under standard organoid culture conditions. However, the *Autoculture* system we developed here provides a platform in which we can systematically explore this question.

We integrated the custom-built and commercially available instruments using the IoT *device-class* framework. This system ensures faster, consistent, and always available operations, increasing the overall throughput while allowing the researchers to focus on formulating questions and data interpretation. Running on a distributed IoT network offers dual benefits. Using a local MQTT broker ensures reliable performance even during internet outages. Cloud integration enables global collaboration across distant labs for shared or complementary research. This setup enhances both the continuity of individual experiments and the integration of worldwide scientific efforts. The reduction of human intervention enabled by the microfluidic feeding system reduces the risk of contamination and other human-introduced mishaps. This is particularly valuable in months-long organoid experiments, where the accumulation of small variations in sample handling can accumulate to generate large differences between experimental batches.

Our system has the capacity to increase the frequency of media collections, morphology assessments, and electrophysiological measurements beyond what is feasible under standard conditions. Feedback in experimental setups becomes essential for maintaining target operating zones in the absence of direct physical observation. In this paper we demonstrated one method of feedback, which was needed to maintain a consistent volume in the organoid growth chamber. During our 7-day run, the system achieved this feedback autonomously and did not experience break-downs or need to use the messaging alert system to overcome anomalies.

How frequently should data be collected? By providing the ability to record as frequently as desired, our system can uncover the optimal frequency for meaningful data capture for rare but significant events. Neural processes unfold with remarkable complexity and variability, yet for practical reasons, many experimental paradigms are limited to daily recordings at most [21, 19, 82, **?**]. Researchers can thereby miss crucial events that occur between observation points. From our results, the high-frequency recordings presented trends not captured in the once-a-day sampling. Hourly recordings like those conducted here can enable the detection of patterns, oscillations, and interactions that may be overlooked in sporadic recordings [77, 43]. These benefits are particularly relevant to researchers wishing to study phenomena with a more immediate timescale, such as neuroplasticity [100]. Additionally, many neurodevelopmental disorders have been hypothesized to be ‘connectopathies,’ characterized by abnormal connectivity [102]. Frequent recordings can provide a nuanced view of the underlying changes in activity patterns during neurodevelopment, contributing to a better understanding of the etiology of neurodevelopmental disorders.

6.2 Future Work

In the future, devices can use the flexibility of MQTT messaging to allow the creation of additional feedback loops to control the experiment. The computer vision techniques we applied to volume estimation could be extended to further applications such as colorimetric and absorbance sensing using the same setup to interrogate biochemical properties of the media. Such measurements could provide a more detailed and accurate analysis of organoid cultures and can lead to a more nuanced understanding of their behavior and responses to different stimuli.

The more the number and different kinds of measurements taken in an experiment, the more automation becomes essential to coordinate and manage the different modalities. The use of 3D printing technology enhances this flexibility, allowing for the seamless combination of multiple systems, such as the integration of our custom media exchange setup with the commercial HD-MEA and portable microscope. We foresee the integration of various sensory data and feedback mechanisms to analyze cell culture conditions. Our platform's consistency and reliability are ideal for comparative studies involving organoids of different genotypes or subjected to various pharmacological manipulations. This capacity to facilitate direct comparisons between diverse experimental conditions holds promise for advancing our understanding of neurodevelopment and neurodevelopmental disorders.

6.2.1 Conditioned media sensing (collaboration with Dr. Holger Schmidt and lab)

The conditioned media extracted from cell culture contains a collection of data to draw inferences relating to the state of the culture. The initial system binned this conditioned media in collection reservoirs to be analyzed downstream. Here, we will use this for real-time data that the system can interpret as feedback to gain insight on the state of the culture.

The first implementation to sense conditioned media is an in-line pH sensor. Prefacing each feeding cycle, spent media is drawn into the syringe pump and then exported either to a collection reservoir or processing module. On this line, a T-intersection fluid sampler pH monitor will be added to record conditioned media. This is used to approximate culture metabolic rates and readjust the feeding regimen.

The second implementation is the further the insight gathered from conditioned media and prepare aliquots for stained counting. All eukaryotic cells generate extracellular vesicles (EVs) through processes of budding the cell membrane or endosome. EVs contain cargo of DNA, RNA, lipids, and proteins, contained in a lipid envelope that are released into the extracellular space. The stain and counting of these EVs yield insight into the state of the cells. The particular phenotypes and number of EVs represent a body of research that will be conducted in collaboration with Dr. Holger Schmidt and lab members. To integrate real-time EV counting devices, the *Autoculture* platform will prepare staining protocols. This is summarized as:

1. Aliquot a sample of conditioned media in the syringe vial
2. Pass the sample through a 200nm in-line filter and back to the syringe vial
3. Draw EV stain from cold storage and mix in equal proportions
4. Incubate for 1 hour with periodic mixing
5. Send a message over MQTT that a stained sample is ready for measurement
6. Translate the prepared sample to the EV sensing device and slowly push the fluid through
7. Receive measurement results

Appendix A

Cell Culture Protocols

Embryonic stem cell culture

All experiments were performed in the adapted C57/BL6 mouse embryonic stem cell (ESC) line (Millipore Sigma # SF-CMTI-2). This line is derived from a male of the C57/BL6J mouse strain. Mycoplasma testing confirmed lack of contamination.

ESCs were maintained on Recombinant Human Protein Vitronectin (Thermo Fisher Scientific # A14700) coated plates using mESC maintenance media containing Glasgow Minimum Essential Medium (Thermo Fisher Scientific # 11710035), Embryonic Stem Cell-Qualified Fetal Bovine Serum (Thermo Fisher Scientific # 10439001), 0.1 mM MEM Non-Essential Amino Acids (Thermo Fisher Scientific # 11140050), 1 mM Sodium Pyruvate (Millipore Sigma # S8636), 2 mM Glutamax supplement (Thermo Fisher Scientific # 35050061), 0.1 mM 2-Mercaptoethanol (Millipore Sigma # M3148), and 0.05 mg/ml Primocin (Invitrogen # ant-pm-05). mESC maintenance media was supplemented with 1,000 units/mL of Recombinant Mouse Leukemia Inhibitory Factor (Millipore Sigma # ESG1107). Media was changed daily.

Vitronectin coating was incubated for 15 min at a concentration of 0.5 µg/mL dissolved in 1X Phosphate-buffered saline (PBS) pH 7.4 (Thermo Fisher Scientific # 70011044). Dissociation and cell passages were done using ReLeSR passaging reagent (Stem Cell Technologies # 05872) according to the manufacturer's instructions. Cell freezing was done in mFreSR cryopreservation medium (Stem Cell Technologies # 05855) according to the manufacturer's instructions.

Cerebral cortex organoids generation

Mouse cortical organoids were grown as previously described by our group [**?**, 18] with some modifications. To generate cortical organoids we single cell dissociated ESCs using TrypLE Express Enzyme (ThermoFisher Scientific #12604021) for 5 minutes at 37°C and re-aggregated in lipidure-coated 96-well V-bottom plates at a density of 3,000 cells per aggregate, in 150 µL of mESC maintenance media supplemented with Rho Kinase Inhibitor (Y-27632, 10 µM, Tocris # 1254) and 1,000 units/mL of Recombinant Mouse Leukemia Inhibitory Factor (Millipore Sigma # ESG1107) (Day -1).

After one day (Day 0), we replaced the medium with cortical differentiation medium containing Glasgow Minimum Essential Medium (Thermo Fisher Scientific # 11710035), 10% Knockout Serum Replacement (Thermo Fisher Scientific # 10828028), 0.1 mM MEM Non-Essential Amino Acids (Thermo Fisher Scientific # 11140050), 1 mM Sodium Pyruvate (Millipore Sigma # S8636), 2 mM Glutamax supplement (Thermo Fisher Scientific # 35050061) 0.1 mM 2-Mercaptoethanol (Millipore Sigma # M3148) and 0.05 mg/ml Primocin (Invitrogen # ant-pm-05). Cortical differentiation medium was supplemented with Rho Kinase Inhibitor (Y-27632, 20 µM # 1254), WNT inhibitor (IWR1- ε , 3 µM, Cayman Chemical # 13659) and TGF-Beta inhibitor (SB431542, Tocris # 1614, 5 µM, days 0-7). Media was changed daily.

On day 5, organoids were transferred to ultra-low adhesion plates (Millipore Sigma # CLS3471) where media was aspirated and replaced with fresh neuronal differentiation media. The plate with organoids was put on an orbital shaker at 60 revolutions per minute. Neuronal differentiation medium contained Dulbecco's Modified Eagle Medium: Nutrient Mixture F-12 with GlutaMAX supplement (Thermo Fisher Scientific # 10565018), 1X N-2 Supplement (Thermo Fisher Scientific # 17502048), 1X Chemically Defined Lipid Concentrate (Thermo Fisher Scientific # 11905031) and 0.05 mg/ml Primocin (Invitrogen # ant-pm-05). Organoids were grown under 5% CO2 conditions. The medium was changed every 2-3 days.

On day 14 and onward, we transferred the organoids to neuronal maturation media containing BrainPhys Neuronal Medium (Stem Cell Technologies # 05790), 1X N-2 Supplement, 1X Chemically Defined Lipid Concentrate (Thermo Fisher Scientific # 11905031), 1X B-27 Supplement (Thermo Fisher Scientific # 17504044), 0.05 mg/ml Primocin (Invitrogen # ant-pm-05) and 0.5% v/v Matrigel Growth Factor Reduced (GFR) Basement Membrane Matrix, LDEV-free.

Organoid plating on microelectrode array

Mouse cerebral cortex organoids were plated, as previously described by our group [18], with two organoids per well. We plated the organoids at day 32 on MaxOne high-density microelectrode arrays (Maxwell Biosystems # PSM). Prior to organoid plating, the microelectrode arrays were coated in 2 steps: First, they were coated with 0.01% Poly-L-ornithine (Millipore Sigma # P4957) at 36.5°C overnight. Then, the microelectrode arrays were washed 3 times with PBS and coated with a solution of 5 µg/ml mouse Laminin (Fisher Scientific # CB40232) and 5 µg/ml human Fibronectin (Fisher Scientific # CB40008) prepared in PBS, at 36.5°C overnight.

After coating, we placed the organoids on the microelectrode arrays and removed excess media. The organoids were incubated at 36.5°C for 20 minutes to promote attachment. We then added prewarmed neuronal maturation media (described in the section above). We exchanged 1.0 mL of conditioned media for fresh every 2 days.

HD-MEAs containing the organoid cultures are stored in an incubator at 36.5 °C, 5% CO2, covered with membrane lids described in the section below, Assembled devices and custom 3D-printed components.

Comparison to primary fetal brain tissue

The RNA-seq results from Automation versus Suspension cultures were then compared to select genes from primary human fetal tissue, sequenced by Bhaduri, *et al.* [6]. The is a large caveat in this comparison in that the Automation versus Suspension cultures were bulk sequenced whereas the primary human fetal tissue was single cell, therefore all insights here are to suggest results to influence the experimental design of a future study (the Adaptive Glucose study).

In Table A.1-A.3, genes and a breif desciption of their functions are listed in the first two columns. In the final three columns, three comparisons are presented:

- **Automation / Organoid:** This compares fold-changes differences caused by automation (increased feeding rate). A positive value here represents up-regulation compared to conventional cerebral organoid culture.
- **oRG, Primary / Organoid:** This compares the difference between primary outer radial glia (oRG) and organoid outer radial glia (oRG). A positive value here represents primary tissue has up-regulation.
- **layer IV, Primary / Organoid:** This compares the difference between primary layer IV neurons and organoid layer IV neurons. A positive value here represents primary tissue has up-regulation.

Gene	Function	**Auto. / Org.** log2FC (adjpval)	**oRG, Prim. / Org.** log2FC (adjpval)	**lay. IV, Prim. / Org.** log2FC (adjpval)
ENO1: Enolase 1	Breakdown of glucose to pyruvate (Glycolysis)	-3.3826 (6.90E-19) Automation reduced this	-0.6537 (0) Organoid increased this	-0.9175 (0) Organoid increased this
PFKM: Phosphofructo-kinase	Essential regulator for speed of glycolysis (Glycolysis)	-0.5491 (0.0954) Not significant	N/A	N/A
GAPDH: Glyceraldehyde-3-phosphate dehydr.	NAD+ to NADH (Glycolysis)	-2.6092 (5.27E-05) Automation reduced this	N/A	N/A
PDK1: Pyruvate dehydrogenase kinase 1	Inactivates pyruvate dehydrogenase enzyme (Anti-Oxphos)	-2.9278 (1.64E-23) Automation reduced this	N/A	N/A
BNIP3: BCL2/adenovirus E1B 19 kDa PIP3	Mitochondrial autophagy (Anti-Oxphos)	-3.3051 (3.03E-62) Automation reduced this	-0.9834 (0) Organoid increased this	-1.0840 (0) Organoid increased this
JUN (AP-1): Activator protein 1	TF response to ROS (Cell Stress)	-0.4960 (0.2290) Not significant	0.3218 (5.85E-30) Organoid decreased this	-0.3454 (5.15E-122) Organoid increased this

Table A.1: DGE comparison of Primary, Organoid, and Automation, Part 1 of 2.

Gene	Function	**Auto. / Org.** log2FC (adjpval)	**oRG, Prim. / Org.** log2FC (adjpval)	**lay. IV, Prim. / Org.** log2FC (adjpval)
HIF1A: HIF-1 alpha	TF response to Hypoxia	-1.1383 (7.04E-4) Automation reduced this	N/A	N/A
ARNT2: HIF-1 beta paralog 2	TF response to Hypoxia	-1.4045 (3.44E-05) Automation reduced this	N/A	N/A
PDH: Pyruvate dehydrogenase	Converts pyruvate to acetyl-CoA (TCA)	-1.3821 (5.81E-4) Automation reduced this	-0.3841 (5.03E-143) Organoid increased this	-0.3543 (3.10E-96) Organoid increased this
ACLY: ATP citrate lyase	Synthesis of cytosolic acetyl-CoA from citrate (TCA)	-1.9321 (3.26E-06) Automation reduced this	N/A	N/A
SLC25A1: Dicarboxylate antiporter solute carrier	Transport of citrate from mitochondria to cytosol (Cell Stress)	-2.1623 (1.71E-07) Automation reduced this	-0.4372 (1.17E-133) Organoid increased this	-0.4564 (1.33E-250) Organoid increased this
IDH2: Isocitrate dehydrogenase	Oxidative decarboxylation of isocitrate (TCA)	-3.1610 (6.39E-12) Automation reduced this	-0.5478 (9.35E-201) Organoid increased this	-0.3842 (4.17E-96) Organoid increased this

Table A.2: DGE comparison of Primary, Organoid, and Automation, Part 2 of 2.

Table A.3: Table of genes regulating pathways in metabolism, stress, and hypoxia with differential gene expression (DGE) results in three perspectives. The "Automation / Organoid" column is DGE comparing automated cerebral organoids (high) to suspension cerebral organoids (low) from (Seiler, *et al.*, 2022)[84]. The remaining two columns, "oRG, Primary / Organoid" and "Layer IV, Primary / Organoid" are derived from DGE from (Bhaduri, *et al.*, 2020)[6] and contrast cell-specific single-cell RNA-seq, either outer radial glia (oRG) or layer IV neurons (Layer IV), from primary tissue (high) to suspension organoid (low). Notes were added to assist the organization.

The selected genes for this table are key regulators of glycolysis, oxphos, cell stress, and hypoxia (see Section 2.2 "Cellular Metabolism in the Brain"). In congruence with the author's findings [6, 84] the data suggests that conventional cerebral organoids have up-regulated glycolysis compared to primrary tissue and that automated feeding reduces this. In addition, conventional cerebral organoids up-regulate mitochondrial autophogy (BNIP3), a pathway to disallow Oxphos. Automated feeding down-regulates anti-Oxphos pathaways (PDK1 and BNIP3), guiding the cultures into closer fidelity to primary tissue. Cell stress as a response to reactive oxidative species (ROS) appears to have a preferential impact on the layer IV neurons in organoids, however, there were no significant results from automation versus convention. It should be noted that the bulk RNA-seq of the automated organoids occured on Day 18 of differentiation which had many markers of neural progenitors however no terminally differentiated neural cells.

In comparison to Oxphos, the TCA cycle appears to be up-regulated in conventional cerebral organoids compared to primrary. The data from automated feeding suggests this is reduced as well.

Appendix B

Reactions

Anaerobic glycolysis

The reactions of anaerobic glycolysis involve the breakdown of glucose into pyruvate and the subsequent conversion of pyruvate into lactate. The reactions of anaerobic glycolysis can be divided into two main stages: the energy investment phase and the energy payoff phase. The overall reaction can be written as:

$$Glucose + 2\ ADP + 2\ Pi + 2NAD^{+} \rightarrow 2\ Lactate + 2\ ATP + 2\ NADH + 2\ H^{+}$$

Energy investment phase:

1. Glucose phosphorylation: Glucose is phosphorylated by hexokinase to form glucose-6-phosphate (G6P) using one molecule of ATP.

$$Glucose + ATP \rightarrow Glucose\text{-}6\text{-}phosphate + ADP$$

2. Isomerization: G6P is converted into fructose-6-phosphate (F6P) by phosphohexose isomerase.

$$Glucose\text{-}6\text{-}phosphate \leftrightarrow Fructose\text{-}6\text{-}phosphate$$

3. Phosphorylation: F6P is phosphorylated by phosphofructokinase to form fructose-1,6-bisphosphate (FBP) using another molecule of ATP.

$$Fructose\text{-}6\text{-}phosphate + ATP \rightarrow Fructose\text{-}1,6\text{-}bisphosphate + ADP$$

4. Cleavage: FBP is cleaved into two three-carbon molecules of glyceraldehyde-3-phosphate (G3P).

$$Fructose\text{-}1,6\text{-}bisphosphate \rightarrow 2\ Glyceraldehyde\text{-}3\text{-}phosphate$$

Energy payoff phase:

5. Oxidation and phosphorylation: G3P is oxidized by NAD+ to form 1,3-bisphosphoglycerate (1,3-BPG) while reducing NAD+ to NADH. In the process, a phosphate group is added to 1,3-BPG to form ATP through substrate-level phosphorylation.

$$\text{Glyceraldehyde-3-phosphate} + NAD^+ + P_i \rightarrow$$
$$1,3\text{-}Bisphosphoglycerate + NADH + H^+$$

$$ADP + 1,3\text{-}Bisphosphoglycerate \rightarrow ATP + 3\text{-}Phosphoglycerate$$

6. Isomerization: The phosphate group on 3-phosphoglycerate is shifted to form 2-phosphoglycerate.

$$3\text{-}Phosphoglycerate \leftrightarrow 2\text{-}Phosphoglycerate$$

7. Dehydration: Water is removed from 2-phosphoglycerate to form phosphoenolpyruvate (PEP).

$$2\text{-}Phosphoglycerate \rightarrow Phosphoenolpyruvate + H_2O$$

8. Phosphorylation: PEP is phosphorylated by pyruvate kinase to form pyruvate and another molecule of ATP through substrate-level phosphorylation.

$$Phosphoenolpyruvate + ADP \rightarrow Pyruvate + ATP$$

9. Lactate formation: In the absence of oxygen, pyruvate is converted to lactate by lactate dehydrogenase, which regenerates NAD+ for use in the earlier steps of glycolysis.

$$Pyruvate + NADH Lactate + NAD^{+}$$

Aerobic glycolysis

Aerobic glycolysis, also known as aerobic respiration or cellular respiration, is a metabolic process that occurs in the presence of oxygen. It involves the breakdown of glucose into pyruvate and the subsequent oxidation of pyruvate to generate ATP through oxidative phosphorylation. The reactions of aerobic glycolysis can be divided into three main stages: glycolysis, the Krebs cycle (also known as the citric acid cycle or TCA cycle), and oxidative phosphorylation.

Glycolysis:

1. Glucose phosphorylation: Glucose is phosphorylated by hexokinase to form glucose-6-phosphate (G6P) using one molecule of ATP.

$$Glucose + ATP \rightarrow Glucose\text{-}6\text{-}phosphate + ADP$$

2. Isomerization: G6P is converted into fructose-6-phosphate (F6P) by phosphohexose isomerase.

$$Glucose\text{-}6\text{-}phosphate \leftrightarrow Fructose\text{-}6\text{-}phosphate$$

3. Phosphorylation: F6P is phosphorylated by phosphofructokinase to form fructose-1,6-bisphosphate (FBP) using another molecule of ATP.

$$Fructose\text{-}6\text{-}phosphate + ATP \rightarrow Fructose\text{-}1,6\text{-}bisphosphate + ADP$$

4. Cleavage: FBP is cleaved into two three-carbon molecules of glyceraldehyde-3-phosphate (G3P).

$$Fructose\text{-}1,6\text{-}bisphosphate \rightarrow 2\ Glyceraldehyde\text{-}3\text{-}phosphate$$

5. Oxidation and phosphorylation: G3P is oxidized by NAD+ to form 1,3-bisphosphoglycerate (1,3-BPG) while reducing NAD+ to NADH. In the process, a phosphate group is added to 1,3-BPG to form ATP through substrate-level phosphorylation.

$$\text{Glyceraldehyde-3-phosphate} + NAD^+ + P_i \rightarrow$$
$$1,3\text{-}Bisphosphoglycerate + NADH + H^+$$

$$ADP + 1,3\text{-}Bisphosphoglycerate \rightarrow ATP + 3\text{-}Phosphoglycerate$$

6. Isomerization: The phosphate group on 3-phosphoglycerate is shifted to form 2-phosphoglycerate.

$$3\text{-}Phosphoglycerate \leftrightarrow 2\text{-}Phosphoglycerate$$

7. Dehydration: Water is removed from 2-phosphoglycerate to form phosphoenolpyruvate (PEP).

$$2\text{-}Phosphoglycerate \rightarrow Phosphoenolpyruvate + H_2O$$

8. Phosphorylation: PEP is phosphorylated by pyruvate kinase to form pyruvate and another molecule of ATP through substrate-level phosphorylation.

$$Phosphoenolpyruvate + ADP \rightarrow Pyruvate + ATP$$

The Krebs cycle:

9. Pyruvate oxidation: Pyruvate is oxidized by pyruvate dehydrogenase to form acetyl-CoA, which enters the Krebs cycle.

$$Pyruvate + NAD + +CoA \rightarrow Acetyl\text{-}CoA + NADH + H^{+} + CO_{2}$$

10. Citrate formation: Acetyl-CoA combines with oxaloacetate to form citrate.

$$Acetyl\text{-}CoA + Oxaloacetate \rightarrow Citrate + CoA$$

11. Isomerization: Citrate is converted into isocitrate by aconitase.

$$Citrate \leftrightarrow Isocitrate$$

12. Oxidation and decarboxylation: Isocitrate is oxidized by isocitrate dehydrogenase to form alpha-k

Appendix C

Supplemental Material for Integrated System

Fabrication & Protocols

Assembled devices and custom 3D-printed components

All custom accessories were 3D printed (Form 3B+, Formlabs) with Biomed Clear V1 material (RS-F2-BMCL-01, Formlabs), except for the collection tube and camera stand in the refrigerator printed in BioMed Black V1 (RS-F2-BMBL-01, Formlabs). The parts were printed flat on the build plate to reduce support material. Alignment grooves between the insert and lid described in the Microfluidic culture chamber form a hole which also facilitates 3D printing by removing the formation of suction cups to the resin tank.

Microfluidic culture chamber

The microfluidic culture chamber assembly allows media to be exchanged inside the HD-MEA well. The chamber assembly consists of a microfluidic module, glass rod lid, and catch tray (Figure 5.2B, C).

The microfluidic module is placed inside the HD-MEA well, creating a media chamber and fluid path into and out of the chamber. Media from outside the incubator travels to the fluidic insert along 0.030” ID and 0.090” OD Tygon tubing (AAD02119-CP, Cole Parmer); the length of the tubing is approximately 100 cm. The tubing attaches to the fluidic insert using PEEK fittings (EW-02014-97, Cole Parmer) wrapped (counter-clockwise) in PTFE thread seal tape around twice the fitting’s circumference. The inlet and outlet are raised inside the fluidic insert to create a pool following a geometry published in previous work [84].

The fluidic insert, glass rod lid, and catch tray use silicone O-rings (5233T543, 5233T479, 5233T297, and 5233T585, McMaster) to provide seals against contaminations and leakage. O-rings were rubbed with a minimal quantity of canola oil for lubrication to facilitate installation and enhance sealing performance. The canola oil can be autoclave-sterilized, but it is unnecessary if the O-rings are sterilized post-lubrication (see Sterilization and assembly).

Membrane lid

The membrane lid used for experimental control conditions follows established designs [70], with adjusted dimensions to improve grip, matching material to the microfluidic culture chamber, and high-temperature silicone O-rings instead of rubber. The outer O-ring (5233T683, McMaster) holds the breathable FEP film (23-1FEP-2-50, CS Hyde Company) stretched over the top of the lid. The inner O-ring (5233T585, McMaster) seals the lid and well. The inner O-ring is also rubbed with a minimal quantity of canola oil as described in the Microfluidic culture chamber section.

In-incubator imaging alignment holders

The custom alignment holders, designed for two configurations, center a digital microscope over the biological sample on the HD-MEA. Components are screw mounted (91292A134, McMaster) to optical breadboards (SAB10X15-M, SAB15X15-M, Base Lab Tools Inc.) to ensure stability and maintain accurate spacing.

HD-MEA off the headstage

The microscope is held over a single HD-MEA by a post and clamp (MS08B, Dino-Lite) mounted with a setscrew and base (SS6MS10, TH15/M, Thorlabs). The custom HD-MEA holder centers it for imaging. Throughout the experiment, HD-MEAs were left resting on each holder. The holder has cut-outs for handling the chip and also avoids the chip's contact pads to decrease scratching and avoid moist surfaces. The holder also has indicators for the chip's proper rotation with respect to the microscope.

HD-MEA on the recording headstage

The custom holder on a post assembly (SS6MS10, TH15/M, TR250/M-JP, Thorlabs) mounts the microscope over the chip on the recording headstage. The custom headstage holder centers both the recording headstage with its attached chip to the microscope.

Cloud Architecture

IoT infrastructure creates an ecosystem of devices and cloud-based services

We built a cloud-based IoT ecosystem that enables communication between users, devices, and services to implement actions, record data, and streamline upload, storage, and analysis. All devices (here: pumps, microscopes, and microelectrode arrays) run software using the *device-class* Python framework (Figure C.1A and **??**). Devices operate collectively with shared core software and complementary behaviors: they can request jobs from each other, yield during sensitive operations, and ensure collaborative functions and smooth operation (Figure C.1D). Devices update their *shadow* in the database whenever their state information changes (i.e, assigned experiment, schedule, current job and estimated completion time, and other dynamic variables) to eliminate the need for device polling. Messages (i.e., job requests) between devices and services are sent through a centralized MQTT broker via the publish/subscribe protocol. This decoupled architecture allows for independent and extensible deployment of components. Data generated by devices is immediately uploaded to an S3 object storage in a predefined structure using an experiment Universally Unique IDentifier (UUID) as the top-level key. A ‘metadata.json’ file stores experiment details, sample information, notes, and an index of the produced data. Raw data is stored separately from analyzed data under different sub-keys. Cloud jobs, which operate as shared services, process raw data from S3 and write results back to S3, reporting status via MQTT messages. To utilize the IoT ecosystem, users initiate experiments, control devices, and visualize data through a website (see **??**, Website and screenshots in Supplemental Figure C.3), with the typical user workflow in Figure C.1C.

Cloud Infrastructure

The cloud infrastructure, including S3, MQTT messaging, and cloud processing within the IoT system, has been previously described [58]. Additionally, we added a database service and defined a consistent organizational structure for MQTT messages and topics across devices and cloud jobs.

We use a combination of self-hosted services running on a server, and large data storage and analysis are performed on the National Research Platform (NRP) cloud compute cluster [67]. The devices are integrated with these cloud services:

- S3 cloud data storage: file storage using S3 object store, hosted on NRP cloud.
- Database: Strapi database stores device states, is self-hosted on our server, and is backed up to S3.

- MQTT messaging: EMQX MQTT broker, self-hosted on the server, and a Python messaging library (braingeneers.iot.broker) utilized by all software endpoints to send and receive messages from the broker.
- Cloud jobs/processing: utilizes a Kubernetes cluster on NRP and launches jobs. Employs software modularized by Docker containers and orchestrated by Kubernetes.
- User interfaces: features a website and integration with messaging apps (e.g., Slack) for interaction with devices, self-hosted on the server.

All custom software functionalities run in Docker containers and operate in a microservice architecture: specialized to a specific task and interface with minimal dependencies. A reverse proxy shields all web services from direct exposure to the internet. For example, webpages are configured through a reverse NGINX proxy, which not only assigns a specific domain to each service but also handles SSL and authentication services.

Security

Devices initiate communication with the server and can be locked down to incoming traffic. Devices take MQTT commands in a specific format and are limited to the set of their defined commands, making them robust to command injection attacks. Accessing all cloud services requires authentication with user/device credentials. All web, MQTT messages, database, and S3 storage operations are encrypted. Access to the user interface website is restricted through the proxy with a login authentication step. On the server side, all web-based microservices are secured through an NGINX proxy. The proxy allows web-based services to be relatively untrusted by providing security (https, authentication, internet visible network listener) and keeping all other web-based services on an internal docker network inaccessible from the internet. This simplifies security for services that will change often and be written by programmers with minimal security training.

Smartplugs

A smartplug was connected to the recording system to automatically manage the duration of the recording system running. The smartplug (S31, SONOFF) running Tasmota 13.2.0 was connected to the MQTT broker (see MQTT) and received MQTT commands over WiFi to turn on and off.

The smartplug facilitated the automated recordings every hour: on the computer connected to the MEA recording system, a script running in Python (3.10) triggered the smartplug via MQTT to turn on the recording system, performed a recording using MaxLab Python API (MaxWell Biosystems), and afterward triggered the smartplug to turn off the recording system.

MQTT

MQTT messages serve as the standard unit of communication (Figure C.1B, orange). MQTT allows devices and services to communicate without direct dependencies between each other by using a common publish/subscribe medium. MQTT clients are the devices or software entities that connect to the broker to send (publish) or receive (subscribe to) messages. Devices and services send messages on MQTT topics, which are hierarchical strings that allow listeners to capture a wide or narrow scope of information. Messages contain a payload with a list of key-value pairs to structure information. For example, a message requesting a microelectrode array to record has a key for recording duration with a value in minutes. Examples of MQTT topic structure and message JSON payloads are summarized in Supplementary Table **??**; see GitHub for more information[1].

The MQTT broker is the central communication facilitator in the network and coordinates messages between clients. The MQTT broker receives all messages from the clients, filters these messages based on their topics, and then distributes them accordingly to other clients who have subscribed to those specific topics. This setup enables efficient message routing and ensures that messages reach the intended recipients without the senders needing to know the specific details of the recipients.

Clients can be sensors, actuators, applications, and services (like UIs or analysis), or any other devices capable of network communication. The organization is future-proof because MQTT allows the creation of new services and devices and uses information available without changing any services (logging, UI, dashboards, analysis of traffic, etc.). Furthermore, message bridges can be employed to convert MQTT messages to other messaging APIs such as text messaging, email, or work chat applications

---

[1] `https://github.com/braingeneers/integrated-system-v1-paper`

like Slack (see Messaging bridge).

IoT device-class

The primary function of a *device-class* involves listening for job requests, executing them, and saving the resulting data to the cloud. This data includes measurements (e.g., images, voltage recordings) and log entries detailing device actions (e.g., cell culture feeding events). By consolidating features, the *device-class* framework simplifies the creation of new devices and enables easy control, updating, and interoperability. The Python *device-class* provides standard features across all IoT devices:

- a state machine defining standard behavior (i.e., experiment workflow)
- structured framework for processing incoming request messages
- autonomous task scheduling, timing, and execution; the internal scheduler manages time
- conflicts of tasks or autonomously recurring jobs
- multi-tasking and responsiveness to user requests via threading
- built-in database operations (i.e., updating device state (shadow))
- communication via MQTT messaging (including alerts via Slack bridge)
- background data upload/download mechanisms, managing queueing and retry
- error handling mechanisms

- communicate and work with other devices in a fleet

A child of the parent *device-class* will inherit all basic functionality, and may add additional features. For instance, a camera *device-class* child performs all actions that a *device-class* can, plus it knows how to handle a request to take a picture.

Having a common parent class consolidates similar features for different devices and allows for easier updates because all devices use the same core code library. The *device-class* code is available within the Braingeneerspy Python package on GitHub [**?**]. For state machine states and request commands see Supplementary Tables C.2 and **??**.

Devices can work in a fleet. As each device has the same core software with complementary behaviors, they integrate seamlessly, similar to how uniform building blocks can easily snap together. Devices can ask each other to yield while they perform sensitive actions (Figure C.1D). Similarly, devices can perform services for each other in a coordinated manner. For example, midway through a recording, a microelectrode array device could ask the pump to deliver a drug. Devices can perform rudimentary decision-making to simplify overarching management. Devices post status and information to an open MQTT topic, allowing services and devices to build on and interface with those devices without altering existing devices and services. Devices can use each other to make sure the experiment is on track across multiple modes of sensing, for example the pump using the eyes of the camera to ensure pumping succeeded.

Pre-experiment workflow

Figure C.1A illustrates the state transitions of a generic device during operation. It begins in the SHUTDOWN state, moving to IDLE, where it waits for user setup verification. Post-setup, it transitions to PRIMED, ready for experimental involvement. In the READY state, the device listens for experiment-specific MQTT messages, ignoring external recruitment until released with an END message. Devices can communicate collectively via MQTT topics for coordinated actions. Transitioning to WAITING occurs upon receiving a pause command, halting job execution. The device moves to EXEC when starting a job, returning to READY upon completion. Data uploads are managed independently of state changes, ensuring continuity even during outages. Devices can exit an experiment at any stage, reverting to IDLE or SHUTDOWN, with data upload tasks resuming upon restart. Figure C.1A describes a generic device (e.g. a scientific instrument) and how it transitions between states during operation. On device start, the device transitions from SHUTDOWN state to IDLE. In the IDLE state, the device is waiting for a user to verify or install physical prerequisites. The IDLE state ensures the user performs the necessary setup of their device to maintain safety and usability. For example, a pump may wait in IDLE state until a user checks and confirms that the pump is clean and proper reagent bottles are connected. On the other hand, a camera may not have any prerequisites and would immediately transition to the next state, PRIMED. In the PRIMED state, the device has all the prerequisites to perform its job and waits to be called into an experiment. Devices listen on their default device MQTT topic. Once it receives a correctly formatted ‘start’ MQTT message (see ‘START’ message in Supplementary Table **??**), it can transition to READY.

Experimental workflow

When the device transitions to READY state, when it listens to an MQTT topic for the experiment. It will refuse requests to be recruited to other experiments until it is released from the current experiment by an END message (see END message in Table **??**). This ensures other users don’t accidentally disturb or recruit an occupied device into a parallel experiment. Switching MQTT topics also ensures exclusivity in incoming messages. The experiment topic structure (see MQTT) allows devices to send a group message addressing all devices. For example, a device or user could send a message to roll-call all devices on the topic (see PING message in Table **??**) or pause all devices while it performs a sensitive action (see PAUSE message in Table **??**). Upon receiving a message to pause, the device transitions to WAITING state, where it does not perform any jobs.

Once a device returns to READY state, it can transition into EXEC state if it receives a job request or has a job request from its schedule. If the device is in WAITING or EXEC while receiving a job request, it will put the request on the schedule to be executed as soon as possible. During EXEC state, the device is actively executing a job request. Once the job finishes or is stopped (see STOP message in Table **??**), the device transitions back to READY state. Any data produced is queued for upload, protected from internet outages by upload retries with exponential backoff. Uploads occur in the background, independent of device state. A device can begin EXEC on a new job immediately after queueing the previous data for upload. From any state, a device can be terminated from an experiment and return to the IDLE state. At any point in the experiment, if a device is gracefully requested to turn off, it performs a final transition to SHUTDOWN state before halting the program. The device keeps the upload queue saved on disk and will continue unfinished uploads upon restart.

Data uploading

Data is saved to a ‘diskcache’ in memory. Once a file is produced, it is put on the upload queue. The upload queue contains references to files within diskcahe. Typical devices have at least 32 GB of disk memory, far larger than a single file. The queue is restricted to grow up to 80% of the device’s memory. Once the memory of the device fills up, older files that were uploaded can become overwritten.

Messaging bridge

The messaging bridge serves as an intermediary for communication between different platforms. It is a service that listens to MQTT messages in the IoT environment and translates them into other APIs like Slack.

The Slack bridge allows IoT devices to send notifications to individuals in designated Slack channels. The messaging bridge uses the message broker API and Slack API [88]. The Slack API requires an API key to be registered with Slack and an API bot to be added to the Slack channels of interest. The message bridge listens to an MQTT channel dedicated to Slack messages. When devices want to post a message to Slack, they publish a message on the dedicated Slack MQTT topic with a JSON payload containing the message. The payload can include text and image data. To support images, a link to an S3 object can be passed in the message, and the messaging bridge will then download and attach it to the Slack message. An image can also be sent directly inside the MQTT message, this requires modifying the message broker service's configuration to increase the MQTT message buffer size to accommodate larger KB-sized files. The Slack bridge is a relatively simple service that decouples devices from dependencies on a specific API by communicating using the common message format MQTT.

Website

The website's front end is developed using React, a JavaScript library for building dynamic and responsive user interfaces. For the backend, Flask, a lightweight Python web framework, is employed. Flask's simplicity and flexibility make it ideal for our web services. It handles server-side operations, data processing, and interaction with databases.

The system's structure incorporates a message broker API, which is established on the backend side of the architecture. This message broker is responsible for the asynchronous communication and management of all IoT devices connected to the cloud. Additionally, Flask's compatibility with Python enables seamless integration with Python APIs, including the braingeneerspy MQTT message broker.

Through the front end, users can issue commands to the devices, and the message broker API in the backend efficiently manages these requests. The user interface encompasses three main components: the initialization page for entering initial experiment data, the control page for managing devices and monitoring their status, and the visualization page for analyzing experimental data through various graphs. All three pages require a specified experiment UUID (see Figure C.1).

Both frontend and backend components are containerized using Docker, ensuring consistency and isolation in different environments. Integration of Cross-Origin Resource Sharing (CORS) is crucial for allowing the React frontend to securely interact with the Flask backend hosted on a different domain.

Initialization page: On the initialization page, users can enter metadata containing experiment and biological sample details, which are compiled into a JSON file and uploaded to cloud storage, serving as a centralized repository for all experimental data.

Control page: On the control page, users can access all the devices involved in the experiment associated with a specific UUID. For each device, users can request the execution of all the commands listed in Table **??**, such as starting, stopping, and pausing the device, as well as scheduling tasks. Additionally, on the control page, users can monitor the real-time status of the device, as outlined in Table C.2.

Visualization page: On the visualization page, users can load data related to the volume estimator from current or previous experiments of a specific UUID. It is also possible to download images on a specific timestamp, allowing for manual monitoring of reservoir tubes.

Feature	**Delta (µL)**	**Running Total (µL)**
Min operating	172.2	172.2
Min to wet glass	94.0	266.2
Target lower operating	88.1	354.3
Target higher operating	204.9	559.2
Max operating	204.9	764.1
Total operating capacity:		**764.1**
Inner lid overflow	345.1	1109.2
Outer lid overflow	464.1	1573.3
Total chip capacity:		**1573.3**
Catch tray	1539.5	3112.8
Total overflowed capacity:		**3112.8**

Table C.1: Numerical operating volume ranges based on the microfluidic culture chamber's 3D model (CAD) measurements. Illustrations of operating ranges are shown in Supplementary Figure C.2. The Feature column lists critical points in the microfluidic culture chamber. The Delta column is the volume space between each feature, and the Running Total column is the volume from the floor to the feature.

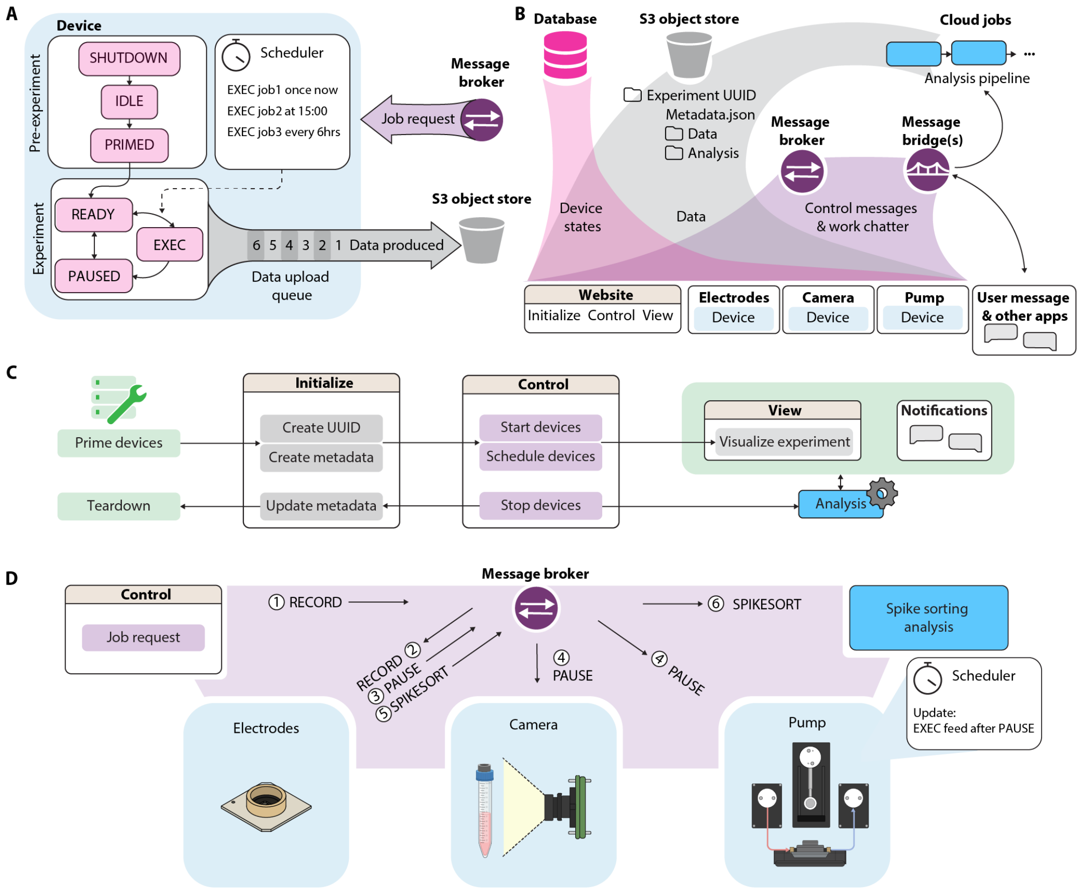

Figure C.1: Cloud-based device interactions. (A) The *device-class* is a generalized state machine framework of all IoT devices. The *device* participates in experiments by taking in job requests (from experimenters or other devices), scheduling and executing the jobs, and producing data files that are queued and uploaded to cloud storage. **(B)** IoT infrastructure. Device states (pink) are saved in a database and displayed on the website user interface. Device-generated data (gray) is saved and organized in cloud storage, where it can be accessed by user interface or analysis cloud jobs. Devices send communications (purple) through a message broker and use message bridges to translate messages to analysis pipelines or text messaging applications. **(C)** User workflow. Devices are physically primed in accordance with experimental procedures such as sterilization. On the 'Initialize' webpage, an experiment is created with a unique ID (UUID) and descriptive notes (metadata). On the 'Control' webpage, devices are called to start working on the experiment and are given a job schedule. The 'View' webpage and notifications allow the user to monitor the ongoing experiment. **(D)** Example of inter-device communication: (1) A RECORD job request is made from the 'Control' panel. (2) The message broker delivers the record request to the electrophysiology recording unit. (3) The electrophysiology unit pauses all other devices to ensure a quality recording. (4) All devices receive a pause request. The pump reschedules a feed until after the pause. (5) Upon finishing the recording, the electrophysiology unit delivers a spike sorting request to commence data analysis.

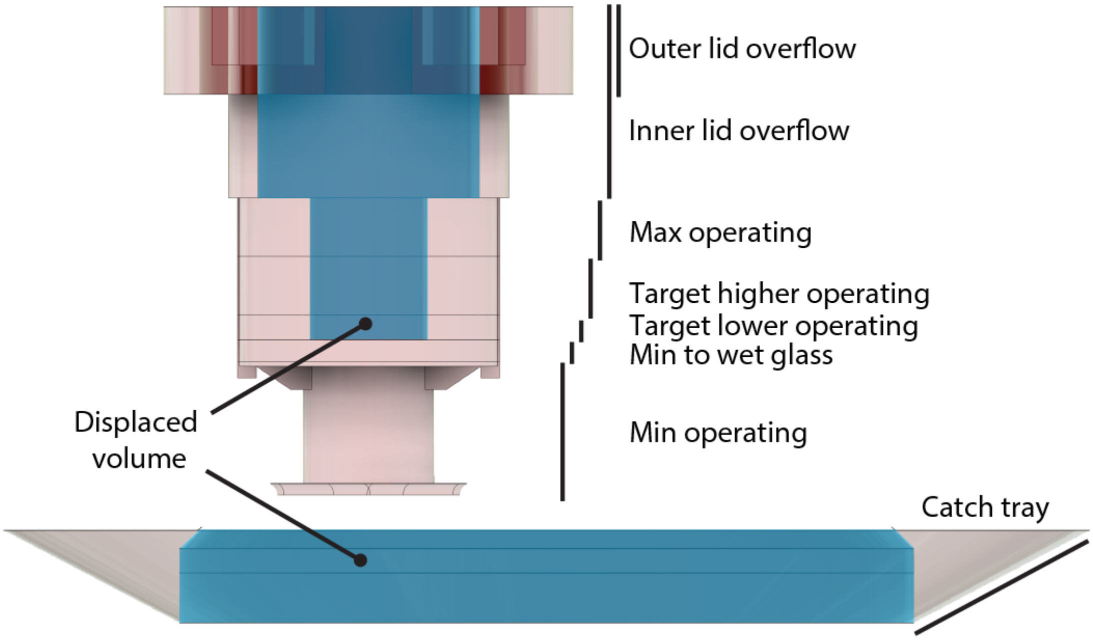

Figure C.2: Diagram of operating ranges of the microfluidic culture chamber. Shaded pink areas represent volumes where media is collected. Shaded blue areas mark displaced volumes (where there is no media stored). The numerical volumes for each operating range are listed in Supplementary Table C.1.

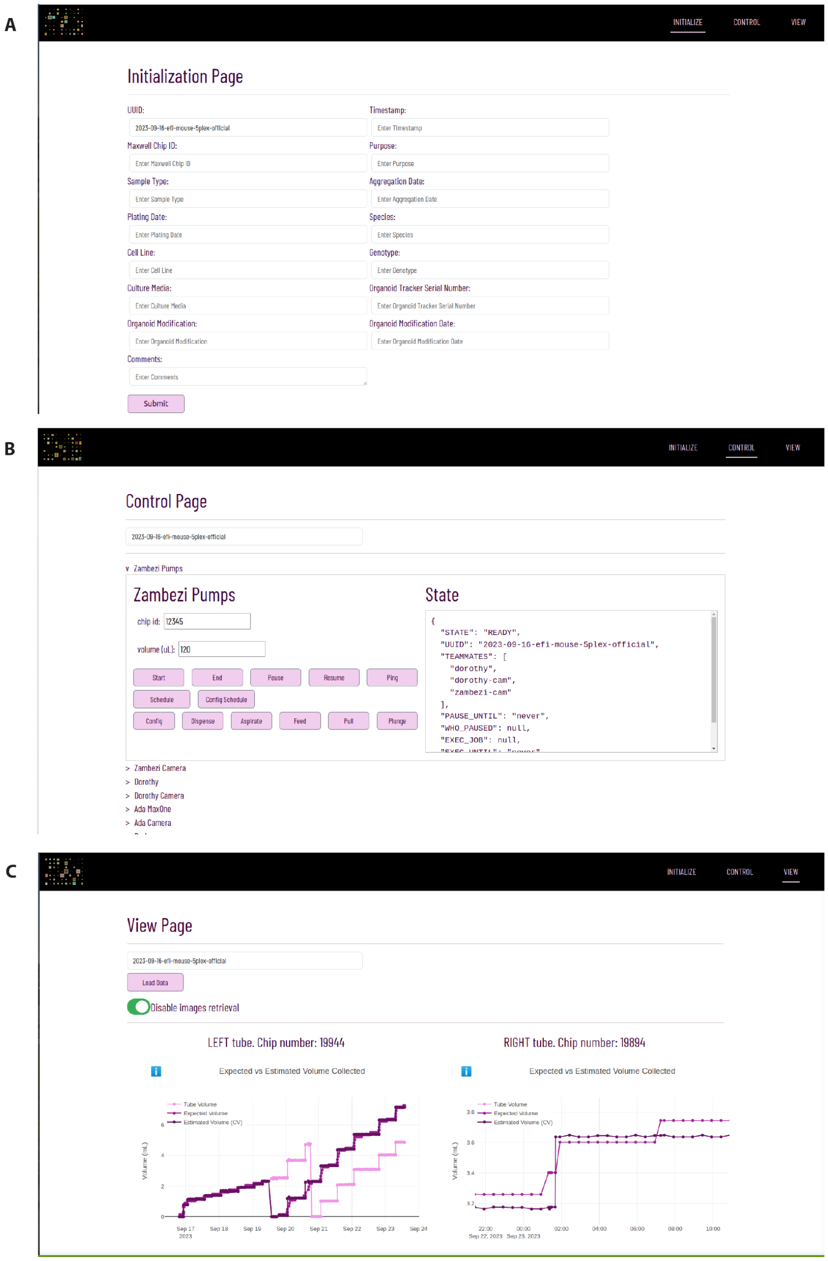

Initialization Page

UUID: 2023-09-16-efi-mouse-5plex-official

Timestamp: Enter Timestamp

Maxwell Chip ID: Enter Maxwell Chip ID

Purpose: Enter Purpose

Sample Type: Enter Sample Type

Aggregation Date: Enter Aggregation Date

Plating Date: Enter Plating Date

Species: Enter Species

Cell Line: Enter Cell Line

Genotype: Enter Genotype

Culture Media: Enter Culture Media

Organoid Tracker Serial Number: Enter Organoid Tracker Serial Number

Organoid Modification: Enter Organoid Modification

Organoid Modification Date: Enter Organoid Modification Date

Comments: Enter Comments

Control Page

2023-09-16-efi-mouse-5plex-official

v Zambezi Pumps

Zambezi Pumps

chip id: 12345

volume (uL): 120

State

```
{
  "STATE": "READY",
  "UUID": "2023-09-16-efi-mouse-5plex-official",
  "TEAMMATES": [
    "dorothy",
    "dorothy-cam",
    "zambezi-cam"
  ],
  "PAUSE_UNTIL": "never",
  "WHO_PAUSED": null,
  "EXEC_JOB": null,
```

- \> Zambezi Camera
- \> Dorothy
- \> Dorothy Camera
- \> Ada MaxOne
- \> Ada Camera

View Page

2023-09-16-efi-mouse-5plex-official

● Disable images retrieval

LEFT tube. Chip number: 19944

Expected vs Estimated Volume Collected

RIGHT tube. Chip number: 19894

Expected vs Estimated Volume Collected

Figure C.3: Webpage user interface screenshots. (A) Initialization page. **(B)** Control page. **(C)** Visualization page: It includes three graph types. (1) Expected versus Estimated Volume Graph. (2) Expected minus Estimated Graph. (3) Collected Volume According to Computer Vision and Pump Graph.

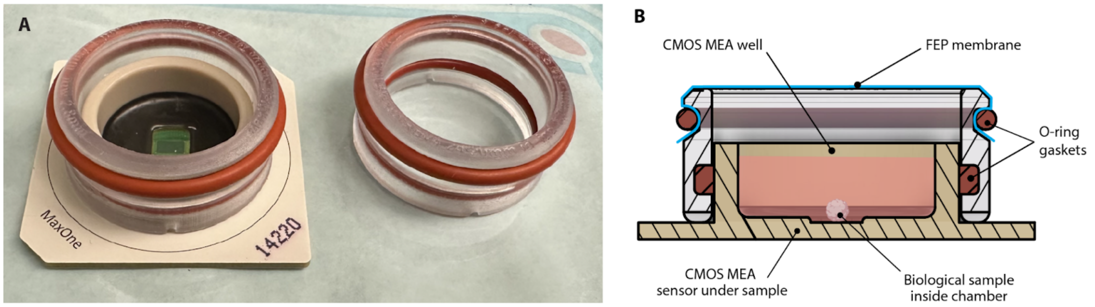

Figure C.4: 3D printed breathable membrane lid used for Controls modeled after designs by Potter (49). **(A)** Picture of the membrane lid and HD-MEA. The chamber is comprised of biocompatible 3D-printed parts, sealed by O-rings to the HD-MEA, and imaged through the FEP membrane stretched over the top with an O-ring. **(B)** Cross-sectional rendering depicting the fluid path and position of the sample.

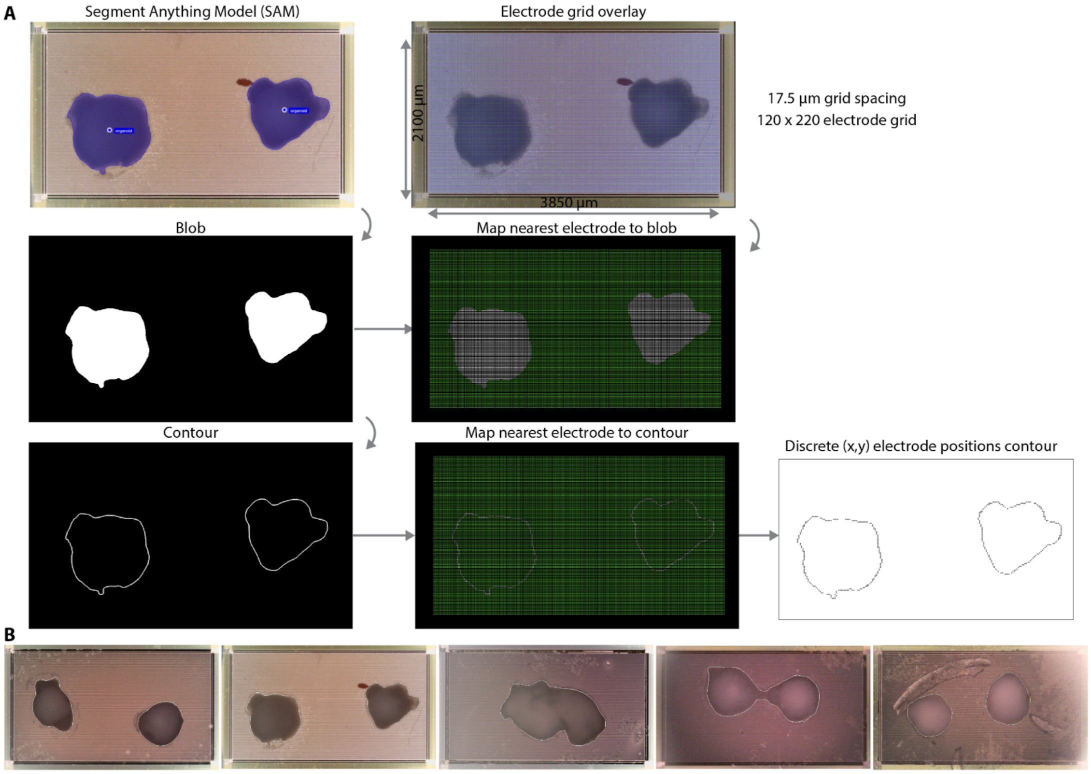

Figure C.5: **(A)** Organoid boundary segmentation process. **(B)** Detected organoid boundaries for all chips.

.

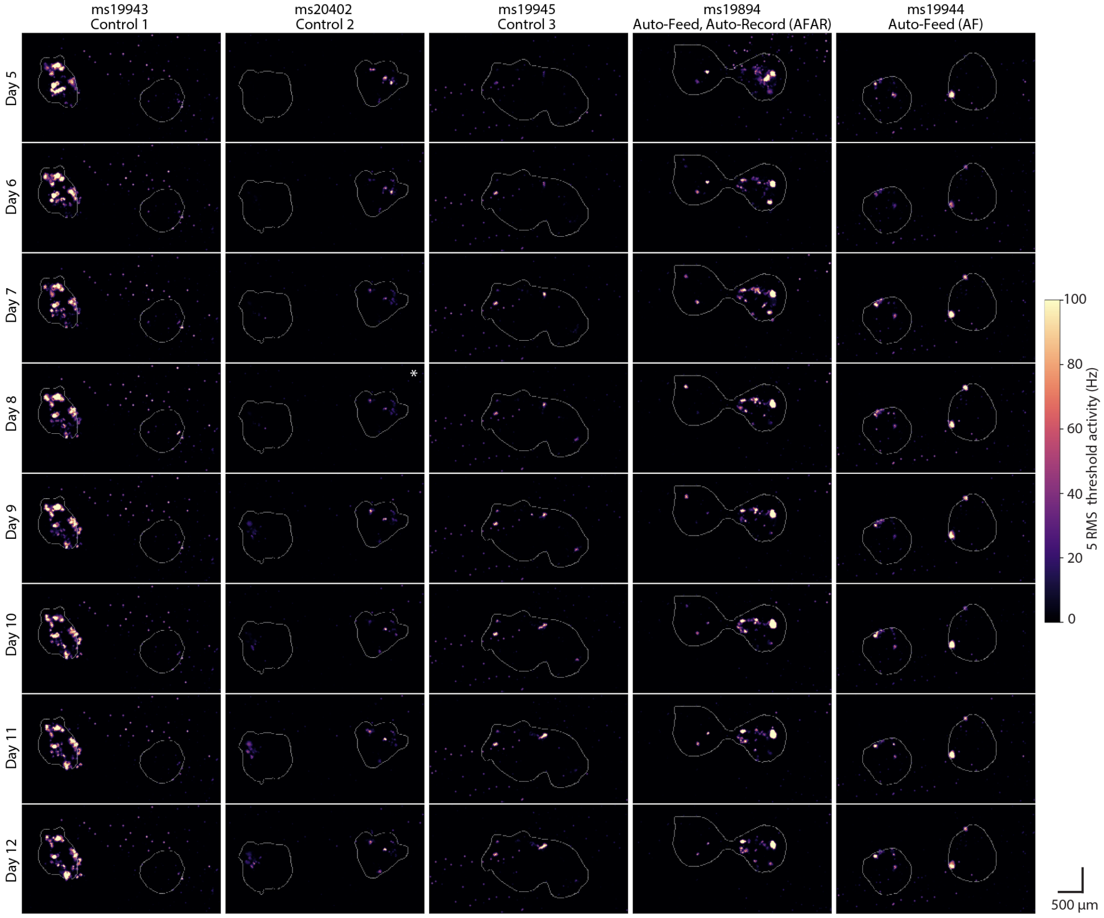

Figure C.6: Daily activity scans of all chips over all days. Boundaries of each organoid were outlined and overlaid for orientation.

State	**Description**
SHUTDOWN	The device has been turned off gracefully and won't respond until it's turned back on.
IDLE	The device is not assigned to any experiments and not doing anything at the moment, and is missing physical prerequisites (i.e., a reagent or piece of hardware) to be able to perform its job.
PRIMED	The device is not assigned to any experiments and not doing anything at the moment, but it has all the physical prerequisites to perform its job.
READY	The device is assigned to an experiment and is ready to execute a command.
WAITING	The device has received a command to PAUSE and is waiting until a given time to resume performing jobs.
EXEC	The device is actively executing a job command.

Table C.2: Device States. The *device-class* is structured as a finite-state machine, with a defined set of states (SHUTDOWN, IDLE, PRIMED, READY, PAUSED, EXEC) that describe its status. The finite-state machine reads a set of inputs and changes to a different state based on those inputs. The inputs can be user physical interactions (i.e., button press, linkage of consumables, etc.), MQTT messages containing job requests, or scheduled events.

Bibliography

[1] M. Akram. Mini-review on glycolysis and cancer. *Journal of Cancer Education: The Official Journal of the American Association for Cancer Education*, 28(3):454–457, September 2013.

[2] Muhammad Akram. Citric acid cycle and role of its intermediates in metabolism. *Cell Biochemistry and Biophysics*, 68(3):475–478, April 2014.

[3] Marco Ballini, Jan Müller, Paolo Livi, Yihui Chen, Urs Frey, Alexander Stettler, Amir Shadmani, Vijay Viswam, Ian Lloyd Jones, David Jäckel, Milos Radivojevic, Marta K. Lewandowska, Wei Gong, Michele Fiscella, Douglas J. Bakkum, Flavio Heer, and Andreas Hierlemann. A 1024-Channel CMOS Microelectrode Array With 26,400 Electrodes for Recording and Stimulation of Electrogenic Cells In Vitro. *IEEE Journal of Solid-State Circuits*, 49(11):2705–2719, November 2014. Conference Name: IEEE Journal of Solid-State Circuits.

[4] Pierre V. Baudin, Victoria T. Ly, Pattawong Pansodtee, Erik A. Jung, Robert Currie, Ryan Hoffman, Helen Rankin Willsey, Alex A. Pollen, Tomasz J. Nowakowski, David Haussler, Mohammed A. Mostajo-Radji, Sofie R. Salama, and Mircea Teodorescu. Low cost cloud based remote microscopy for biological sciences. *Internet of Things*, 18:100454, May 2022.

[5] Grégory Bellot, Raquel Garcia-Medina, Pierre Gounon, Johanna Chiche, Danièle Roux, Jacques Pouysségur, and Nathalie M. Mazure. Hypoxia-induced autophagy is mediated through hypoxia-inducible factor induction of BNIP3 and BNIP3L via their BH3 domains. *Molecular and Cellular Biology*, 29(10):2570–2581, May 2009.

[6] Aparna Bhaduri, Madeline G. Andrews, Walter Mancia Leon, Diane Jung, David Shin, Denise Allen, Dana Jung, Galina Schmunk, Maximilian Haeussler, Jahan Salma, Alex A. Pollen, Tomasz J. Nowakowski, and Arnold R. Kriegstein. Cell stress in cortical organoids impairs molecular subtype specification. *Nature*, 578(7793):142–148, February 2020.

[7] J. Bylund, N. Finnström, and E. H. Oliw. Gene expression of a novel cytochrome P450 of the CYP4F subfamily in human seminal vesicles. *Biochemical and Biophysical Research Communications*, 261(1):169–174, July 1999.

[8] Christophe Cariou, Laure Moiroux-Arvis, François Pinet, and Jean-Pierre Chanet. Internet of Underground Things in Agriculture 4.0: Challenges, Applications and Perspectives. *Sensors*, 23(8):4058, January 2023. Number: 8 Publisher: Multidisciplinary Digital Publishing Institute.

[9] Yu Chen, Robert H. Austin, and James C. Sturm. On-chip cell labelling and washing by capture and release using microfluidic trap arrays. *Biomicrofluidics*, 11(5):054107, September 2017.

[10] Zhe Chen, Garrett J. Blair, Chengdi Cao, Jim Zhou, Daniel Aharoni, Peyman Golshani, Hugh T. Blair, and Jason Cong. FPGA-Based In-Vivo Calcium Image Decoding for Closed-Loop Feedback Applications. *IEEE Transactions on Biomedical Circuits and Systems*, 17(2):169–179, April 2023. Conference Name: IEEE Transactions on Biomedical Circuits and Systems.

[11] Carl F. Cori and Gerty T. Cori. THE CARBOHYDRATE METABOLISM OF TUMORS: II. CHANGES IN THE SUGAR, LACTIC ACID, AND CO2-COMBINING POWER OF BLOOD PASSING THROUGH A TUMOR. *Journal of Biological Chemistry*, 65(2):397–405, September 1925.

[12] Jiyeon K. Denninger, Xi Chen, Altan M. Turkoglu, Patricia Sarchet, Abby R. Volk, Joshua D. Rieskamp, Pearlly Yan, and Elizabeth D. Kirby. Defining the adult hippocampal neural stem cell secretome: In vivo versus in vitro transcriptomic differences and their correlation to secreted protein levels. *Brain Research*, 1735:146717, May 2020.

[13] Alexander Dobin. STAR 2.7.11b, 2017.

[14] Alexander Dobin, Carrie A. Davis, Felix Schlesinger, Jorg Drenkow, Chris Zaleski, Sonali Jha, Philippe Batut, Mark Chaisson, and Thomas R. Gingeras. STAR: ultrafast universal RNA-seq aligner. *Bioinformatics (Oxford, England)*, 29(1):15–21, January 2013.

[15] H. Eagle. Amino acid metabolism in mammalian cell cultures. *Science (New York, N.Y.)*, 130(3373):432–437, August 1959.

[16] Rasheena Edmondson, Jessica Jenkins Broglie, Audrey F. Adcock, and Liju Yang. Three-Dimensional Cell Culture Systems and Their Applications in Drug Discovery and Cell-Based Biosensors. *Assay and Drug Development Technologies*, 12(4):207–218, May 2014.

[17] Mototsugu Eiraku, Kiichi Watanabe, Mami Matsuo-Takasaki, Masako Kawada, Shigenobu Yonemura, Michiru Matsumura, Takafumi Wataya, Ayaka Nishiyama, Keiko Muguruma, and Yoshiki Sasai. Self-Organized Formation of Polarized Cortical Tissues from ESCs and Its Active Manipulation by Extrinsic Signals. *Cell Stem Cell*, 3(5):519–532, November 2008.

[18] Matthew A. T. Elliott, Hunter E. Schweiger, Ash Robbins, Samira Vera-Choqqueccota, Drew Ehrlich, Sebastian Hernandez, Kateryna Voitiuk, Jinghui Geng, Jess L. Sevetson, Cordero Core, Yohei M. Rosen, Mircea Teodorescu, Nico O. Wagner, David Haussler, and Mohammed A. Mostajo-Radji. Internet-Connected Cortical Organoids for Project-Based Stem Cell and Neuroscience Education. *eNeuro*, 10(12), December 2023. Publisher: Society for Neuroscience Section: Research Article: New Research.

[19] Summer R. Fair, Dominic Julian, Annalisa M. Hartlaub, Sai Teja Pusuluri, Girik Malik, Taryn L. Summerfied, Guomao Zhao, Arelis B. Hester, William E. Ackerman, Ethan W. Hollingsworth, Mehboob Ali, Craig A. McElroy, Irina A. Buhimschi, Jaime Imitola, Nathalie L. Maitre, Tracy A. Bedrosian, and Mark E. Hester. Electrophysiological Maturation of Cerebral Organoids Correlates with Dynamic Morphological and Cellular Development. *Stem Cell Reports*, 15(4):855–868, October 2020.

[20] Aisha Farhana and Sarah L. Lappin. Biochemistry, Lactate Dehydrogenase. In *StatPearls*. StatPearls Publishing, Treasure Island (FL), 2024.

[21] Stefano L. Giandomenico, Susanna B. Mierau, George M. Gibbons, Lea M. D. Wenger, Laura Masullo, Timothy Sit, Magdalena Sutcliffe, Jerome Boulanger, Marco Tripodi, Emmanuel Derivery, Ole Paulsen, András Lakatos, and Madeline A. Lancaster. Cerebral organoids at the air–liquid interface generate diverse nerve tracts with functional output. *Nature Neuroscience*, 22(4):669–679, April 2019. Publisher: Nature Publishing Group.

[22] L. B. Gladden. Lactate metabolism: a new paradigm for the third millennium. *The Journal of Physiology*, 558(Pt 1):5–30, July 2004.

[23] Cesar Gonzalez, Enrique Armijo, Javiera Bravo-Alegria, Andrea Becerra-Calixto, Charles E. Mays, and Claudio Soto. Modeling amyloid beta and tau pathology in human cerebral organoids. *Molecular Psychiatry*, 23(12):2363–2374, December 2018. Publisher: Nature Publishing Group.

[24] Livia Goto-Silva, Nadia M. E. Ayad, Iasmin L. Herzog, Nilton P. Silva, Bernard Lamien, Helcio R. B. Orlande, Annie da Costa Souza, Sidarta Ribeiro, Michele Martins, Gilberto B. Domont, Magno Junqueira, Fernanda Tovar-Moll, and Stevens K. Rehen. Computational fluid dynamic analysis of physical forces playing a role in brain organoid cultures in two different multiplex platforms. *BMC developmental biology*, 19(1):3, March 2019.

[25] C. Granchi, S. Bertini, M. Macchia, and F. Minutolo. Inhibitors of lactate dehydrogenase isoforms and their therapeutic potentials. *Current Medicinal Chemistry*, 17(7):672–697, 2010.

[26] Robert D. Guzy and Paul T. Schumacker. Oxygen sensing by mitochondria at complex III: the paradox of increased reactive oxygen species during hypoxia. *Experimental Physiology*, 91(5):807–819, September 2006.

[27] Julia J. Harris, Renaud Jolivet, and David Attwell. Synaptic energy use and supply. *Neuron*, 75(5):762–777, September 2012.

[28] Carl D. Holmgren, Marat Mukhtarov, Anton E. Malkov, Irina Y. Popova, Piotr Bregestovski, and Yuri Zilberter. Energy substrate availability as a determinant of neuronal resting potential, GABA signaling and spontaneous network activity in the neonatal cortex in vitro. *Journal of Neurochemistry*, 112(4):900–912, February 2010.

[29] Danying Hu, Yuanzheng Gong, Eric J. Seibel, Laligam N. Sekhar, and Blake Hannaford. Semi-autonomous image-guided brain tumour resection using an integrated robotic system: A bench-top study. *The International Journal of Medical Robotics and Computer Assisted Surgery*, 14(1):e1872, 2018. _eprint: https://onlinelibrary.wiley.com/doi/pdf/10.1002/rcs.1872.

[30] Dongeun Huh, Benjamin D. Matthews, Akiko Mammoto, Martín Montoya-Zavala, Hong Yuan Hsin, and Donald E. Ingber. Reconstituting organ-level lung functions on a chip. *Science (New York, N.Y.)*, 328(5986):1662–1668, June 2010.

[31] Anton Ivanov, Marat Mukhtarov, Piotr Bregestovski, and Yuri Zilberter. Lactate Effectively Covers Energy Demands during Neuronal Network Activity in Neonatal Hippocampal Slices. *Frontiers in Neuroenergetics*, 3:2, 2011.

[32] Farzaneh Jafary, Mohamad Reza Ganjalikhany, Ali Moradi, Mahdie Hemati, and Sepideh Jafari. Novel Peptide Inhibitors for Lactate Dehydrogenase A (LDHA): A Survey to Inhibit LDHA Activity via Disruption of Protein-Protein Interaction. *Scientific Reports*, 9:4686, March 2019.

[33] Sabina Kanton, Michael James Boyle, Zhisong He, Malgorzata Santel, Anne Weigert, Fátima Sanchís-Calleja, Patricia Guijarro, Leila Sidow, Jonas Simon Fleck, Dingding Han, Zhengzong Qian, Michael Heide, Wieland B. Huttner, Philipp Khaitovich, Svante Pääbo, Barbara Treutlein, and J. Gray Camp. Organoid single-cell genomic atlas uncovers human-specific features of brain development. *Nature*, 574(7778):418–422, October 2019.

[34] Jaimon T. Kelly, Katrina L. Campbell, Enying Gong, and Paul Scuffham. The Internet of Things: Impact and Implications for Health Care Delivery. *Journal of Medical Internet Research*, 22(11):e20135, November 2020. Company: Journal of Medical Internet Research Distributor: Journal of Medical Internet Research Institution: Journal of Medical Internet Research Label: Journal of Medical Internet Research Publisher: JMIR Publications Inc., Toronto, Canada.

[35] Arseny S. Khakhalin. Questioning the depolarizing effects of GABA during early brain development. *Journal of Neurophysiology*, 106(3):1065–1067, September 2011.

[36] Alexander Kirillov, Eric Mintun, Nikhila Ravi, Hanzi Mao, Chloe Rolland, Laura Gustafson, Tete Xiao, Spencer Whitehead, Alexander C. Berg, Wan-Yen Lo, Piotr Dollár, and Ross Girshick. Segment Anything, April 2023. arXiv:2304.02643 [cs].

[37] Fanwei Kong, Liang Yuan, Yuan F. Zheng, and Weidong Chen. Automatic liquid handling for life science: a critical review of the current state of the art. *Journal of Laboratory Automation*, 17(3):169–185, June 2012.

[38] Satoshi Konishi, Takeshi Hashimoto, Tsubasa Nakabuchi, Takatoshi Ozeki, and Hiroki Kajita. Cell and tissue system capable of automated culture, stimulation, and monitor with the aim of feedback control of organs-on-a-chip. *Scientific Reports*, 11(1):2999, February 2021. Publisher: Nature Publishing Group.

[39] Dieter A. Kubli, Melissa N. Quinsay, Chengqun Huang, Youngil Lee, and Asa B. Gustafsson. Bnip3 functions as a mitochondrial sensor of oxidative stress during myocardial ischemia and reperfusion. *American Journal of Physiology. Heart and Circulatory Physiology*, 295(5):H2025–2031, November 2008.

[40] Madeline A. Lancaster and Juergen A. Knoblich. Organogenesis in a dish: modeling development and disease using organoid technologies. *Science (New York, N.Y.)*, 345(6194):1247125, July 2014.

[41] Madeline A. Lancaster, Magdalena Renner, Carol-Anne Martin, Daniel Wenzel, Louise S. Bicknell, Matthew E. Hurles, Tessa Homfray, Josef M. Penninger, Andrew P. Jackson, and Juergen A. Knoblich. Cerebral organoids model human brain development and microcephaly. *Nature*, 501(7467):373–379, September 2013. Number: 7467 Publisher: Nature Publishing Group.

[42] Chang-Soo Lee. Grand Challenges in Microfluidics: A Call for Biological and Engineering Action. *Frontiers in Sensors*, 1, 2020.

[43] Suengwon Lee and Christian I. Hong. Organoids as Model Systems to Investigate Circadian Clock-Related Diseases and Treatments. *Frontiers in Genetics*, 13:874288, April 2022.

[44] Heng Li, Bob Handsaker, Alec Wysoker, Tim Fennell, Jue Ruan, Nils Homer, Gabor Marth, Goncalo Abecasis, and Richard Durbin. The Sequence Alignment/Map format and SAMtools. *Bioinformatics*, 25(16):2078–2079, August 2009.

[45] Chun Liu, Angelos Oikonomopoulos, Nazish Sayed, and Joseph C. Wu. Modeling human diseases with induced pluripotent stem cells: from 2D to 3D and beyond. *Development (Cambridge, England)*, 145(5):dev156166, March 2018.

[46] Katherine E. Liu and William A. Frazier. Phosphorylation of the BNIP3 C-Terminus Inhibits Mitochondrial Damage and Cell Death without Blocking Autophagy. *PloS One*, 10(6):e0129667, 2015.

[47] Xiaoguang Lu and Ye Ai. Automatic Microfluidic Cell Wash Platform for Purifying Cells in Suspension: Puriogen. *Analytical Chemistry*, 94(26):9424–9433, July 2022. Publisher: American Chemical Society.

[48] Victoria T. Ly, Pierre V. Baudin, Pattawong Pansodtee, Erik A. Jung, Kateryna Voitiuk, Yohei M. Rosen, Helen Rankin Willsey, Gary L. Mantalas, Spencer T. Seiler, John A. Selberg, Sergio A. Cordero, Jayden M. Ross, Marco Rolandi, Alex A. Pollen, Tomasz J. Nowakowski, David Haussler, Mohammed A. Mostajo-Radji, Sofie R. Salama, and Mircea Teodorescu. Picroscope: low-cost system for simultaneous longitudinal biological imaging. *Communications Biology*, 4(1):1261, November 2021.

[49] Adam MacDonald, Brianna Lu, Maxime Caron, Nina Caporicci-Dinucci, Dale Hatrock, Kevin Petrecca, Guillaume Bourque, and Jo Anne Stratton. Single Cell Transcriptomics of Ependymal Cells Across Age, Region and Species Reveals Cilia-Related and Metal Ion Regulatory Roles as Major Conserved Ependymal Cell Functions. *Frontiers in Cellular Neuroscience*, 15:703951, 2021.

[50] Niall P. Macdonald, Joan M. Cabot, Petr Smejkal, Rosanne M. Guijt, Brett Paull, and Michael C. Breadmore. Comparing Microfluidic Performance of Three-Dimensional (3D) Printing Platforms. *Analytical Chemistry*, 89(7):3858–3866, April 2017. Publisher: American Chemical Society.

[51] Richard J. McMurtrey. Analytic Models of Oxygen and Nutrient Diffusion, Metabolism Dynamics, and Architecture Optimization in Three-Dimensional Tissue Constructs with Applications and Insights in Cerebral Organoids. *Tissue Engineering. Part C, Methods*, 22(3):221–249, March 2016.

[52] Jan Müller, Marco Ballini, Paolo Livi, Yihui Chen, Milos Radivojevic, Amir Shadmani, Vijay Viswam, Ian L. Jones, Michele Fiscella, Roland Diggelmann, Alexander Stettler, Urs Frey, Douglas J. Bakkum, and Andreas Hierlemann. High-resolution CMOS MEA platform to study neurons at subcellular, cellular, and network levels. *Lab on a chip*, 15(13):2767–2780, July 2015.

[53] Juliana Minardi Nascimento, Verônica M. Saia-Cereda, Rafaela C. Sartore, Rodrigo Madeiro da Costa, Clarissa S. Schitine, Hercules Rezende Freitas, Michael Murgu, Ricardo A. de Melo Reis, Stevens K. Rehen, and Daniel Martins-de Souza. Human Cerebral Organoids and Fetal Brain Tissue Share Proteomic Similarities. *Frontiers in Cell and Developmental Biology*, 7:303, 2019.

[54] Nam-Trung Nguyen, Majid Hejazian, Chin Hong Ooi, and Navid Kashaninejad. Recent Advances and Future Perspectives on Microfluidic Liquid Handling. *Mi-*

cromachines, 8(6):186, June 2017. Number: 6 Publisher: Multidisciplinary Digital Publishing Institute.

[55] Markus Ojala and Gemma C. Garriga. Permutation Tests for Studying Classifier Performance. *The Journal of Machine Learning Research*, 11:1833–1863, August 2010.

[56] Marius Pachitariu, Nicholas Steinmetz, Shabnam Kadir, Matteo Carandini, and Harris Kenneth D. Kilosort: realtime spike-sorting for extracellular electrophysiology with hundreds of channels, June 2016. Pages: 061481 Section: New Results.

[57] Yunjeong Park, Sebastian Hernandez, Cristian O. Hernandez, Hunter E. Schweiger, Houpu Li, Kateryna Voitiuk, Harika Dechiraju, Nico Hawthorne, Elana M. Muzzy, John A. Selberg, Frederika N. Sullivan, Roberto Urcuyo, Sofie R. Salama, Elham Aslankoohi, Heather J. Knight, Mircea Teodorescu, Mohammed A. Mostajo-Radji, and Marco Rolandi. Modulation of neuronal activity in cortical organoids with bioelectronic delivery of ions and neurotransmitters. *Cell Reports Methods*, 4(1):100686, January 2024.

[58] David F. Parks, Kateryna Voitiuk, Jinghui Geng, Matthew A. T. Elliott, Matthew G. Keefe, Erik A. Jung, Ash Robbins, Pierre V. Baudin, Victoria T. Ly, Nico Hawthorne, Dylan Yong, Sebastian E. Sanso, Nick Rezaee, Jess Sevetson, Spencer T. Seiler, Rob Currie, Alex A. Pollen, Keith B. Hengen, Tomasz J. Nowakowski, Mohammed A. Mostajo-Radji, Sofie R. Salama, Mircea Teodorescu, and David Haussler. Internet of Things Architecture for Cellular Biology, February 2022. Pages: 2021.07.29.453595 Section: New Results.

[59] David F. Parks, Kateryna Voitiuk, Jinghui Geng, Matthew A. T. Elliott, Matthew G. Keefe, Erik A. Jung, Ash Robbins, Pierre V. Baudin, Victoria T. Ly, Nico Hawthorne, Dylan Yong, Sebastian E. Sanso, Nick Rezaee, Jess L. Sevetson, Spencer T. Seiler, Rob Currie, Alex A. Pollen, Keith B. Hengen, Tomasz J. Nowakowski, Mohammed A. Mostajo-Radji, Sofie R. Salama, Mircea Teodorescu, and David Haussler. IoT cloud laboratory: Internet of Things architecture for cellular biology. *Internet of Things*, 20:100618, November 2022.

[60] Austin P. Passaro and Steven L. Stice. Electrophysiological Analysis of Brain Organoids: Current Approaches and Advancements. *Frontiers in Neuroscience*, 14, 2021.

[61] João Passos, Sérgio Ivan Lopes, Filipe Manuel Clemente, Pedro Miguel Moreira, Markel Rico-González, Pedro Bezerra, and Luís Paulo Rodrigues. Wearables and Internet of Things (IoT) Technologies for Fitness Assessment: A Systematic Review. *Sensors*, 21(16):5418, January 2021. Number: 16 Publisher: Multidisciplinary Digital Publishing Institute.

[62] Minal Patel and Shuying Yang. Advances in reprogramming somatic cells to induced pluripotent stem cells. *Stem Cell Reviews and Reports*, 6(3):367–380, September 2010.

[63] Anca M. Pașca, Jin-Young Park, Hyun-Woo Shin, Qihao Qi, Omer Revah, Rebecca Krasnoff, Ruth O'Hara, A. Jeremy Willsey, Theo D. Palmer, and Sergiu P. Pașca. Human 3D cellular model of hypoxic brain injury of prematurity. *Nature Medicine*, 25(5):784–791, May 2019.

[64] Luc Pellerin, Anne-Karine Bouzier-Sore, Agnès Aubert, Sébastien Serres, Michel Merle, Robert Costalat, and Pierre J. Magistretti. Activity-dependent regulation of energy metabolism by astrocytes: an update. *Glia*, 55(12):1251–1262, September 2007.

[65] Simone Picelli, Omid R. Faridani, Åsa K. Björklund, Gösta Winberg, Sven Sagasser, and Rickard Sandberg. Full-length RNA-seq from single cells using Smart-seq2. *Nature Protocols*, 9(1):171–181, January 2014. Publisher: Nature Publishing Group.

[66] Trenton L. Place, Frederick E. Domann, and Adam J. Case. Limitations of oxygen delivery to cells in culture: An underappreciated problem in basic and translational research. *Free Radical Biology & Medicine*, 113:311–322, December 2017.

[67] National Research Platform. National Research Platform: Accelerating Research Through Advanced Networks, 2024.

[68] Alex A. Pollen, Aparna Bhaduri, Madeline G. Andrews, Tomasz J. Nowakowski, Olivia S. Meyerson, Mohammed A. Mostajo-Radji, Elizabeth Di Lullo, Beatriz Alvarado, Melanie Bedolli, Max L. Dougherty, Ian T. Fiddes, Zev N. Kronenberg, Joe Shuga, Anne A. Leyrat, Jay A. West, Marina Bershteyn, Craig B. Lowe, Bryan J. Pavlovic, Sofie R. Salama, David Haussler, Evan E. Eichler, and Arnold R. Kriegstein. Establishing Cerebral Organoids as Models of Human-Specific Brain Evolution. *Cell*, 176(4):743–756.e17, February 2019.

[69] Michelle Potter, Emma Newport, and Karl J. Morten. The Warburg effect: 80 years on. *Biochemical Society Transactions*, 44(5):1499–1505, October 2016.

[70] Steve M Potter and Thomas B DeMarse. A new approach to neural cell culture for long-term studies. *Journal of Neuroscience Methods*, 110(1):17–24, September 2001.

[71] Jüri Reimand, Meelis Kull, Hedi Peterson, Jaanus Hansen, and Jaak Vilo. g:Profiler–a web-based toolset for functional profiling of gene lists from large-scale experiments. *Nucleic Acids Research*, 35(Web Server issue):W193–200, July 2007.

[72] Magdalena Renner, Madeline A. Lancaster, Shan Bian, Heejin Choi, Taeyun Ku, Angela Peer, Kwanghun Chung, and Juergen A. Knoblich. Self-organized developmental patterning and differentiation in cerebral organoids. *The EMBO journal*, 36(10):1316–1329, May 2017.

[73] P. R. Rich. The molecular machinery of Keilin's respiratory chain. *Biochemical Society Transactions*, 31(Pt 6):1095–1105, December 2003.

[74] Jochen Ringe, Christian Kaps, Gerd-Rüdiger Burmester, and Michael Sittinger. Stem cells for regenerative medicine: advances in the engineering of tissues and organs. *Die Naturwissenschaften*, 89(8):338–351, August 2002.

[75] Anna Ronowska, Andrzej Szutowicz, Hanna Bielarczyk, Sylwia Gul-Hinc, Joanna Klimaszewska-Łata, Aleksandra Dyś, Marlena Zyśk, and Agnieszka Jankowska-Kulawy. The Regulatory Effects of Acetyl-CoA Distribution in the Healthy and Diseased Brain. *Frontiers in Cellular Neuroscience*, 12:169, 2018.

[76] Eva Ruusuvuori, Ilya Kirilkin, Nikhil Pandya, and Kai Kaila. Spontaneous network events driven by depolarizing GABA action in neonatal hippocampal slices are not attributable to deficient mitochondrial energy metabolism. *The Journal of Neuroscience: The Official Journal of the Society for Neuroscience*, 30(46):15638–15642, November 2010.

[77] Nina M. Rzechorzek, Magdalena A. Sutcliffe, Andrei Mihut, Koby Baranes, Nuzli Karam, Daniel Lloyd-Davies Sánchez, Sew Y. Peak-Chew, Aiwei Zeng, Noah Poulin, Estere Seinkmane, Kaiser Karim, Christopher M. Proctor, Mark Kotter, Madeline A. Lancaster, and Andrew D. Beale. Circadian clocks in human cerebral organoids, February 2024. Pages: 2024.02.20.580978 Section: New Results.

[78] Pintu Kumar Sadhu, Venkata P. Yanambaka, and Ahmed Abdelgawad. Internet of Things: Security and Solutions Survey. *Sensors*, 22(19):7433, January 2022. Number: 19 Publisher: Multidisciplinary Digital Publishing Institute.

[79] M. Mehdi Salek, Pooria Sattari, and Robert J. Martinuzzi. Analysis of fluid flow and wall shear stress patterns inside partially filled agitated culture well plates. *Annals of Biomedical Engineering*, 40(3):707–728, March 2012.

[80] J. Sassone, C. Colciago, M. Figini, P. Marchi, F. Colleoni, A. Di Pardo, R. Zippel, Y. Torrente, S. Sipione, V. Silani, and A. Ciammola. A13 Mutant huntingtin induces activation of Bcl-2/adenovirus E1B 19-kDa interacting protein (BNIP3). *Journal of Neurology, Neurosurgery & Psychiatry*, 81(Suppl 1):A4–A4, September 2010. Publisher: BMJ Publishing Group Ltd Section: EHDN Plenary Meeting: abstracts.

[81] W. F. Scherer, J. T. Syverton, and G. O. Gey. Studies on the propagation in vitro of poliomyelitis viruses. IV. Viral multiplication in a stable strain of human

malignant epithelial cells (strain HeLa) derived from an epidermoid carcinoma of the cervix. *The Journal of Experimental Medicine*, 97(5):695–710, May 1953.

[82] Manuel Schröter, Congwei Wang, Marco Terrigno, Philipp Hornauer, Ziqiang Huang, Ravi Jagasia, and Andreas Hierlemann. Functional imaging of brain organoids using high-density microelectrode arrays. *Mrs Bulletin*, 47(6):530–544, 2022.

[83] J. Schuberth and D. J. Jenden. Transport of choline from plasma to cerebrospinal fluid in the rabbit with reference to the origin of choline and to acetylcholine metabolism in brain. *Brain Research*, 84(2):245–256, February 1975.

[84] Spencer T. Seiler, Gary L. Mantalas, John Selberg, Sergio Cordero, Sebastian Torres-Montoya, Pierre V. Baudin, Victoria T. Ly, Finn Amend, Liam Tran, Ryan N. Hoffman, Marco Rolandi, Richard E. Green, David Haussler, Sofie R. Salama, and Mircea Teodorescu. Modular automated microfluidic cell culture platform reduces glycolytic stress in cerebral cortex organoids. *Scientific Reports*, 12(1):20173, November 2022. Number: 1 Publisher: Nature Publishing Group.

[85] Gregg L. Semenza. Hypoxia-inducible factors in physiology and medicine. *Cell*, 148(3):399–408, February 2012.

[86] Venktesh S. Shirure, Ye Bi, Matthew B. Curtis, Andrew Lezia, Madeleine M. Goedegebuure, S. Peter Goedegebuure, Rebecca Aft, Ryan C. Fields, and Steven C. George. Tumor-on-a-chip platform to investigate progression and drug sensitivity in cell lines and patient-derived organoids. *Lab on a Chip*, 18(23):3687–3702, December 2018.

[87] R. A. Shooter and G. O. Gey. Studies of the mineral requirements of mammalian cells. *British Journal of Experimental Pathology*, 33(1):98–103, February 1952.

[88] Slack. Unlock your productivity potential with Slack Platform.

[89] Aidan Slattery, Zhenghui Wen, Pauline Tenblad, Jesús Sanjosé-Orduna, Diego Pintossi, Tim den Hartog, and Timothy Noël. Automated self-optimization, intensification, and scale-up of photocatalysis in flow. *Science*, 383(6681):eadj1817, January 2024. Publisher: American Association for the Advancement of Science.

[90] Scott M. Smith and Sara R. Zwart. Nutritional biochemistry of spaceflight. *Advances in Clinical Chemistry*, 46:87–130, 2008.

[91] Adéle Stewart-Lord, Clare Beanlands, Ricardo Khine, Shani Shamah, Noreen Sinclair, Sandie Woods, Nick Woznitza, and Lesley Baillie. The Role and Development of Advanced Clinical Practice Within Allied Health Professions: A Mixed Method Study. *Journal of Multidisciplinary Healthcare*, 13:1705–1715, 2020.

[92] Peng Su, Yuanyuan Chen, and Mengmeng Lu. Smart city information processing under internet of things and cloud computing. *The Journal of Supercomputing*, 78(3):3676–3695, February 2022.

[93] Dang Ngoc Anh Suong, Keiko Imamura, Ikuyo Inoue, Ryotaro Kabai, Satoko Sakamoto, Tatsuya Okumura, Yoshikazu Kato, Takayuki Kondo, Yuichiro Yada, William L. Klein, Akira Watanabe, and Haruhisa Inoue. Induction of inverted morphology in brain organoids by vertical-mixing bioreactors. *Communications Biology*, 4(1):1213, October 2021.

[94] Andrzej Szutowicz, Hanna Bielarczyk, Agnieszka Jankowska-Kulawy, Tadeusz Pawełczyk, and Anna Ronowska. Acetyl-CoA the key factor for survival or death of cholinergic neurons in course of neurodegenerative diseases. *Neurochemical Research*, 38(8):1523–1542, August 2013.

[95] Kazutoshi Takahashi and Shinya Yamanaka. Induction of Pluripotent Stem Cells from Mouse Embryonic and Adult Fibroblast Cultures by Defined Factors. *Cell*, 126(4):663–676, August 2006.

[96] Maria Tenje, Anna Fornell, Mathias Ohlin, and Johan Nilsson. Particle Manipulation Methods in Droplet Microfluidics. *Analytical Chemistry*, 90(3):1434–1443, February 2018.

[97] Miguel F. Tenreiro, Ana F. Louro, Paula M. Alves, and Margarida Serra. Next generation of heart regenerative therapies: progress and promise of cardiac tissue engineering. *npj Regenerative Medicine*, 6(1):1–17, June 2021. Publisher: Nature Publishing Group.

[98] J. A. Thomson, J. Itskovitz-Eldor, S. S. Shapiro, M. A. Waknitz, J. J. Swiergiel, V. S. Marshall, and J. M. Jones. Embryonic stem cell lines derived from human blastocysts. *Science (New York, N.Y.)*, 282(5391):1145–1147, November 1998.

[99] Mario A. Torres-Acosta, Gary J. Lye, and Duygu Dikicioglu. Automated liquid-handling operations for robust, resilient, and efficient bio-based laboratory practices. *Biochemical Engineering Journal*, 188:108713, December 2022.

[100] Gina G. Turrigiano and Sacha B. Nelson. Homeostatic plasticity in the developing nervous system. *Nature Reviews Neuroscience*, 5(2):97–107, February 2004. Number: 2 Publisher: Nature Publishing Group.

[101] Roman Tyzio, Camille Allene, Romain Nardou, Michel A. Picardo, Sumii Yamamoto, Sudhir Sivakumaran, Maddalena D. Caiati, Sylvain Rheims, Marat Minlebaev, Mathieu Milh, Pascal Ferré, Rustem Khazipov, Jean-Louis Romette, Jean Lorquin, Rosa Cossart, Ilgam Khalilov, Astrid Nehlig, Enrico Cherubini, and Yehezkel Ben-Ari. Depolarizing actions of GABA in immature neurons depend neither on ketone bodies nor on pyruvate. *The Journal of Neuroscience: The Official Journal of the Society for Neuroscience*, 31(1):34–45, January 2011.

[102] Jean-Paul Urenda, Ashley Del Dosso, Marcella Birtele, and Giorgia Quadrato. Present and Future Modeling of Human Psychiatric Connectopathies With Brain Organoids. *Biological Psychiatry*, 93(7):606–615, April 2023.

[103] Ana Uzquiano, Amanda J. Kedaigle, Martina Pigoni, Bruna Paulsen, Xian Adiconis, Kwanho Kim, Tyler Faits, Surya Nagaraja, Noelia Antón-Bolaños, Chiara Gerhardinger, Ashley Tucewicz, Evan Murray, Xin Jin, Jason Buenrostro, Fei Chen, Silvia Velasco, Aviv Regev, Joshua Z. Levin, and Paola Arlotta. Single-cell multiomics atlas of organoid development uncovers longitudinal molecular programs of cellular diversification of the human cerebral cortex, March 2022. Pages: 2022.03.17.484798 Section: New Results.

[104] John Vivian, Arjun Arkal Rao, Frank Austin Nothaft, Christopher Ketchum, Joel Armstrong, Adam Novak, Jacob Pfeil, Jake Narkizian, Alden D. Deran, Audrey Musselman-Brown, Hannes Schmidt, Peter Amstutz, Brian Craft, Mary Goldman, Kate Rosenbloom, Melissa Cline, Brian O'Connor, Megan Hanna, Chet Birger, W. James Kent, David A. Patterson, Anthony D. Joseph, Jingchun Zhu, Sasha Zaranek, Gad Getz, David Haussler, and Benedict Paten. Toil enables reproducible, open source, big biomedical data analyses. *Nature Biotechnology*, 35(4):314–316, April 2017. Publisher: Nature Publishing Group.

[105] Kateryna Voitiuk, Spencer T. Seiler, Mirella Pessoa de Melo, Jinghui Geng, Sebastian Hernandez, Hunter E. Schweiger, Jess L. Sevetson, David F. Parks, Ash Robbins, Sebastian Torres-Montoya, Drew Ehrlich, Matthew A. T. Elliott, Tal Sharf, David Haussler, Mohammed A. Mostajo-Radji, Sofie R. Salama, and Mircea Teodorescu. A feedback-driven IoT microfluidic, electrophysiology, and imaging platform for brain organoid studies, May 2024. Pages: 2024.03.15.585237 Section: Confirmatory Results.

[106] Sidra Waheed, Joan M. Cabot, Niall P. Macdonald, Trevor Lewis, Rosanne M. Guijt, Brett Paull, and Michael C. Breadmore. 3D printed microfluidic devices: enablers and barriers. *Lab on a Chip*, 16(11):1993–2013, May 2016. Publisher: The Royal Society of Chemistry.

[107] O. Warburg, F. Wind, and E. Negelein. THE METABOLISM OF TUMORS IN THE BODY. *The Journal of General Physiology*, 8(6):519–530, March 1927.

[108] Aryeh Warmflash, Benoit Sorre, Fred Etoc, Eric D. Siggia, and Ali H. Brivanlou. A method to recapitulate early embryonic spatial patterning in human embryonic stem cells. *Nature Methods*, 11(8):847–854, August 2014. Publisher: Nature Publishing Group.

[109] Momoko Watanabe, Jessie E. Buth, Neda Vishlaghi, Luis de la Torre-Ubieta, Jiannis Taxidis, Baljit S. Khakh, Giovanni Coppola, Caroline A. Pearson, Ken Yamauchi, Danyang Gong, Xinghong Dai, Robert Damoiseaux, Roghiyh Aliyari, Simone Liebscher, Katja Schenke-Layland, Christine Caneda, Eric J. Huang,

Ye Zhang, Genhong Cheng, Daniel H. Geschwind, Peyman Golshani, Ren Sun, and Bennett G. Novitch. Self-Organized Cerebral Organoids with Human-Specific Features Predict Effective Drugs to Combat Zika Virus Infection. *Cell Reports*, 21(2):517–532, October 2017.

[110] Matthias T. Wyss, Pierre J. Magistretti, Alfred Buck, and Bruno Weber. Labeled acetate as a marker of astrocytic metabolism. *Journal of Cerebral Blood Flow and Metabolism: Official Journal of the International Society of Cerebral Blood Flow and Metabolism*, 31(8):1668–1674, August 2011.

[111] Gary Yellen. Fueling thought: Management of glycolysis and oxidative phosphorylation in neuronal metabolism. *The Journal of Cell Biology*, 217(7):2235–2246, July 2018.

[112] Maksim Zakhartsev, Xuelian Yang, Matthias Reuss, and Hans Otto Pörtner. Metabolic efficiency in yeast Saccharomyces cerevisiae in relation to temperature dependent growth and biomass yield. *Journal of Thermal Biology*, 52:117–129, August 2015.

[113] Yu Shrike Zhang, Julio Aleman, Su Ryon Shin, Tugba Kilic, Duckjin Kim, Seyed Ali Mousavi Shaegh, Solange Massa, Reza Riahi, Sukyoung Chae, Ning Hu, Huseyin Avci, Weijia Zhang, Antonia Silvestri, Amir Sanati Nezhad, Ahmad Manbohi, Fabio De Ferrari, Alessandro Polini, Giovanni Calzone, Noor Shaikh, Parissa Alerasool, Erica Budina, Jian Kang, Nupura Bhise, João Ribas, Adel Pourmand, Aleksander Skardal, Thomas Shupe, Colin E. Bishop, Mehmet Remzi Dokmeci, Anthony Atala, and Ali Khademhosseini. Multisensor-integrated organs-on-chips platform for automated and continual in situ monitoring of organoid behaviors. *Proceedings of the National Academy of Sciences of the United States of America*, 114(12):E2293–E2302, March 2017.

[114] Yuri Zilberter, Tanya Zilberter, and Piotr Bregestovski. Neuronal activity in vitro and the in vivo reality: the role of energy homeostasis. *Trends in Pharmacological Sciences*, 31(9):394–401, September 2010.